The Dissertation Committee for Parvathy Prem certifies that this is the approved version of the following dissertation:

DSMC Simulations of Volatile Transport in a Transient Lunar Atmosphere and Ice Deposition in Cold Traps after a Comet Impact

Committee:

David B. Goldstein, Supervisor

Philip L. Varghese, Co-Supervisor

Laurence M. Trafton, Co-Supervisor

Laxminarayan L. Raja

Richard C. Elphic

DSMC Simulations of Volatile Transport in a Transient Lunar Atmosphere and Ice Deposition in Cold Traps after a Comet Impact

by

Parvathy Prem, BE; MSE

Dissertation

Presented to the Faculty of the Graduate School of
The University of Texas at Austin
in Partial Fulfillment
of the Requirements
for the Degree of

Doctor of Philosophy

The University of Texas at Austin
May 2017

Epigraph

"All that survives after our death are publications and people. So look carefully after the words you write, the thoughts and publications you create, and how you love others. For these are the only things that will remain."

– Susan Niebur (1973-2012)

Acknowledgements

First and foremost, I would like to thank my advisors – Prof. David Goldstein, Prof. Philip Varghese and Dr. Laurence Trafton – for their guidance, encouragement and support over almost seven years of graduate study. They have my gratitude and respect not only for their (willingly shared) scientific expertise, but also for the high standards to which they hold their work (and that of their students), for the balance of guidance and independence that they provide as advisors, and for the consideration with which they treat others. One of the main reasons I wished to complete this PhD was to be able to pay forward what I've gained from their training; I would be more than satisfied if I could ever advise a student even half as well as they have.

I would also like to thank the other two members of my Dissertation Committee – Prof. Laxminarayan Raja for his interest in my progress and professional advice over the years, and Dr. Richard (Rick) Elphic for his enthusiasm and support. The encouragement that I've received from Rick and several other members of the planetary science community has made a world of difference to me, and I am deeply appreciative of all that they do to make this a welcoming and inclusive field.

The work described in this dissertation would not have been possible without Dr. Bénédicte Stewart's previous work. I cannot thank Bénédicte enough for all her help in getting started with the DSMC code. I would also like to thank the late Dr. Elisabetta Pierazzo and Dr. Natalia Artemieva for their collaboration, which has been instrumental to this work. Many thanks are also due to several current and former members of the Computational Fluid Physics Lab at UT Austin – Dr. William (Billy) McDoniel, Dr. Seng Yeoh, Dr. Chris Moore, Dr. Andrew Walker, Dr. Aaron Morris, Jeff Chu and Will Hoey. Billy's improvements to code performance helped my work greatly; Chris, Andrew and

Aaron were always ready to help when I was getting started; Yeoh and Jeff were great office mates, and all of them have been great company to work with.

I was fortunate to have several excellent professors during the course of my graduate studies, but special thanks go to Prof. John Lassiter and Prof. John (Jack) Holt. John's class on Meteoritics and Early Solar System Processes not only provided a broad overview of the field that was as interesting as it has been useful, but also taught me how to read scientific literature critically. As for Jack's Planetary Geology & Geophysics class – I don't think I've ever enjoyed a course more; for that, and for all his support in the years since, Jack has my lasting gratitude.

Despite the fascinating science and the wonderful people I've had the privilege to work with, the last seven years have also been the hardest of my life. I don't think I could have pulled through without the support of several old friends, who deserve much more thanks than I can give in a few lines. The same goes for my parents and my little brother, who have always had more faith in me than I think is rational, and for my husband, Anindya, who has been my best friend for eleven years. I would also like to thank Dr. Margarita Leonor Diaz for her invaluable professional help over the last year and a half – I don't think I could have written this dissertation without it.

Last, but by no means least, I would like to acknowledge Tina Woods, Geetha Rajagopal and Scott Messec for their help with all things administrative and electronic. The simulations presented here would not have been possible without the generous computational resources provided by the Texas Advanced Computing Center, and the assistance of the technical support teams at TACC and ICES. This work was also supported in part by the NASA LASER program under Grant NNX09AM60G.

DSMC Simulations of Volatile Transport in a Transient Lunar Atmosphere and Ice Deposition in Cold Traps after a Comet Impact

Parvathy Prem, Ph.D.
The University of Texas at Austin, 2017

Supervisor: David B. Goldstein
Co-Supervisors: Philip L. Varghese and Laurence M. Trafton

Over the years, a number of missions have detected signs of water and other volatiles in cold, permanently shadowed regions near the lunar poles, where temperatures are sufficiently low that volatile ices can remain stable over geological timescales. Several observations suggest that comet impacts may have played a role in delivering these cold-trapped volatiles. In this work, I use Direct Simulation Monte Carlo (DSMC) simulations to investigate the transport and sequestration of water in the aftermath of a lunar comet impact, focusing on developing a broad understanding of the physical processes that govern the fate of impact-delivered volatiles (particularly water), in order to better interpret remote sensing data.

The sheer amount of vapor generated by a volatile-rich impact can transform the Moon's tenuous, surface-bound exosphere into a collisional, transient atmosphere with characteristic gas dynamic features that influence the redistribution of impact-delivered volatiles. Notably, the simulations indicate that reconvergence of vapor antipodal to the point of impact may result in preferential redistribution of water in the vicinity of the antipode; in some circumstances, water may be distributed non-uniformly between different cold traps. It is also found that atmospheric self-shielding from photodestruction significantly increases the amount of water that reaches the shelter of cold traps.

Volatile transport in an impact-generated atmosphere is also influenced by gas phase interactions with solar radiation and the lunar surface. The Moon has a distinctive surface thermal environment, characterized by large gradients in temperature over very small scales. In this work, I develop a stochastic rough surface temperature model that is then coupled to volatile transport simulations. It is found that surface roughness reduces the mobility of water at high latitudes, while also increasing the concentration of atmospheric/exospheric water molecules around the poles. I also implement a coupled DSMC-photon Monte Carlo method to model radiative heat transfer in the evolving, three-dimensional, rarefied atmosphere. The trapping of radiation within the optically thick gas slows the rate of cooling of the expanding vapor cloud, and also affects near-field atmospheric structure and winds. Ultimately, the fate of impact-delivered water is determined by the interplay between these factors.

Table of Contents

List of Tables

List of Figures

Chapter 1: Introduction

1.1. MOTIVATION

Over the years, a number of missions have observed signs of water and other volatiles in permanently shadowed craters ('cold traps') near the lunar poles. Due to the almost perpendicular orientation of the Moon's spin axis relative to the ecliptic plane, parts of the interiors of these craters have not seen sunlight for over two billion years (Arnold, 1979) and have temperatures so low that a variety of volatile compounds, notably water, can remain stable at the surface and shallow sub-surface over geological time scales (Watson et al., 1961; Paige et al., 2010). Understanding the origin, abundance and distribution of lunar water and other volatiles is integral to understanding the history of the inner solar system and the in situ resources available for planetary exploration.

The ongoing search for cold-trapped water on the Moon has yielded mixed results (discussed in Chapter 2 and references therein). Several groups have used remote sensing data to derive constraints on the abundance and distribution of cold-trapped volatiles, but significant uncertainties remain regarding the nature and amount of water present. In this context, a better understanding of source and delivery mechanisms is key to interpreting observations and to understanding the lunar volatile inventory.

Water can reach the lunar surface in several ways; it can be degassed from the lunar interior, generated by solar wind bombardment of the regolith or delivered by impacts of volatile-bearing bodies ranging in size from micrometeoroids to comets (Arnold, 1979; Morgan and Shemansky, 1991). Comet impacts are a delivery mechanism of particular interest for a number of reasons. In 2009, the LCROSS mission led to the detection not only of H_2O, but also CH_4, NH_3 and other compounds commonly found in comets, at the Cabeus cold trap (Colaprete et al., 2010). More recently, Miller et al. (2014) revisited neutron spectroscopy data from the Lunar Prospector mission and identified isolated sub-surface hydrogen signatures at some cold traps – the absence of a corresponding surficial signature suggesting delivery of the detected hydrogen (possibly water) by some ancient, episodic source. It has also been observed that water ice, if present, appears to be heterogeneously distributed between cold traps, with some regions of permanent shadow lacking signs of water (Mitrofanov et al., 2010; Gladstone et al., 2012). These differences could be due to local variations in thermal properties and history (Siegler et al., 2014; Siegler et al., 2016; Schorghofer and Taylor, 2007), but it could also be the case that certain delivery mechanisms, such as comet impacts, distribute volatiles non-uniformly between cold traps, further contributing to the heterogeneity of the signatures observed. (Other delivery mechanisms, such as the cold-trapping of solar wind-generated volatiles, rely on collisionless migration of molecules to the poles, which should lead to uniform filling of cold traps, since the average ballistic hop distance is larger than typical cold trap dimensions). Lastly, recent evidence from the MESSENGER mission for water ice and organic material at Mercury (Chabot et al., 2014) has renewed interest in impact-delivery of inner solar system volatiles, with the Hokusai impact suggested as a potential source of present-day ice deposits (Ernst et al., 2016).

Modeling comets as a source of lunar water is a complex problem. During impact, a cometary nucleus is subject to extreme pressures and temperatures, more than sufficient to completely vaporize constituent ices (Pierazzo and Melosh, 2000). Much of this vapor escapes lunar gravity within minutes, but a significant part remains gravitationally bound and can linger for many lunar days (Stewart et al., 2011) in the form of a transient atmosphere. The primary challenge in modeling this atmosphere lies in the fact that the sheer quantity of volatiles delivered by a comet impact significantly changes the way in which volatile transport takes place. Usually, the Moon's surface-bound exosphere is so tenuous, with surface densities O(10^{10}) molecules/m^3, that molecules rarely encounter each other, and can be assumed to migrate across the lunar surface through collisionless, ballistic hops (Stern, 1999; Cook et al., 2013). However, after a volatile-rich impact, the atmosphere can become sufficiently dense that gas dynamic processes are governed by collisions between molecules – these interactions are then no longer negligible. Moreover, in a sufficiently dense atmosphere, water vapor may be partially shielded from photodestruction (Arnold, 1979), the primary loss process. Shielding and other processes that become important in an impact-generated atmosphere – such as photochemical reactions (Berezhnoi and Klumov, 2000) and radiative transfer – could play a significant role in determining the abundance and distribution of cold-trapped species.

Several prior investigations (Butler, 1997; Crider and Vondrak, 2000 & 2002; Schorghofer, 2014; Moores, 2016) have modeled the transport of volatiles in the collisionless limit – a valid approximation when the source of volatiles does not alter the tenuous nature of the lunar exosphere. However, relatively few studies have addressed the qualitatively different nature of volatile transport in an impact-generated atmosphere. Stewart et al. (2011) developed a hybrid approach to the problem, using the SOVA hydrocode and the Direct Simulation Monte Carlo (DSMC) method to simulate an oblique comet impact and to track the deposition of impact-generated water vapor in cold traps over the course of several lunar days, with the primary objective of determining how much water from the simulated comet impact was transported to polar cold traps. Despite several simplifications introduced in the modeling, Stewart et al.'s work represents the most detailed treatment of post-impact gas dynamics to date.

This work is motivated by the need to understand post-impact volatile transport processes in more depth – to characterize the structure of a transient atmosphere generated by a volatile-rich impact on an otherwise virtually airless body, to re-examine the significance of physical processes neglected in prior work, and to analyze the implications of the structure and gas dynamics of an impact-generated atmosphere for the transport and deposition of water at lunar cold traps.

1.2. OBJECTIVES

The overarching objective of this work is to understand the behavior of impact-generated atmospheres in more depth, by advancing the numerical approach developed by Stewart (2010) through the identification of characteristic features that govern volatile transport and sequestration in the aftermath of an impact, and the re-examination of two major simplifying assumptions made in the previous model.

By identifying characteristic features of an impact-generated atmosphere, I aim to address the following questions: Given a site indicative of a comet impact, what can we say about the associated volatile fallout? Qualitatively, how is this affected by varying impact parameters? The focus here is on developing a broad understanding of the physical processes that govern the fate of impact-delivered volatiles, rather than on quantifying the contribution of comets to the lunar volatile inventory, as in Stewart (2010) and Stewart et al. (2011).

The two major simplifying assumptions in the model of Stewart (2010) that are re-examined in detail (as mentioned above) concern the treatment of lunar surface temperature and the interaction between water vapor and radiation in the impact-generated atmosphere. Surface temperature is a critical parameter in determining the residence time of migrating water molecules on the lunar surface, which in turn may affect the rate and magnitude of volatile transport to Permanently Shadowed Regions (PSR's), as well as the susceptibility of migrating molecules to photodestruction. In order to develop a more realistic representation of the lunar surface thermal environment, I develop a method for modeling temperature variations due to small-scale surface roughness, and couple this model to simulations of water vapor migration. The specific objective here is to address how the presence of shadows and small-scale cold traps affects the transport, loss and sequestration of lunar water.

Interest in radiative transfer within an impact-generated atmosphere stems from the fact that such an atmosphere may not be transparent to several types of radiation (as was previously assumed). Ultraviolet solar radiation is responsible for photolysis, the primary loss process for water molecules; attenuation of this radiation by an absorbing atmosphere may reduce the atmospheric loss rate. Meanwhile, radiative heat transfer – due to the attenuation and absorption of infrared/microwave radiation from the Sun and the lunar surface, and the re-absorption of spontaneously emitted molecular radiation – affects the temperature of the transient atmosphere, and thereby its gas dynamic behavior. In this work, I develop a shielding algorithm to account for the attenuation of solar ultraviolet radiation, and implement a Monte Carlo method to address the radiative heat transfer problem. By coupling these methods to the DSMC simulation, I aim to investigate the extent to which shielding and radiative transfer affect the structure of the transient atmosphere, and analyze the implications for the redistribution of water delivered by a comet impact.

1.3. DISSERTATION OVERVIEW

The structure of this dissertation is as follows. Chapter 2 reviews relevant literature pertaining to lunar volatiles, thermal modeling of planetary surfaces, and computational methods and models for radiative heat transfer. Chapter 3 describes the methods and models used in this work. Chapter 4 discusses results concerning the structure of an impact-generated atmosphere and cold trap deposition patterns, and briefly explores the influence of impact parameters and multi-species interactions. Chapter 5 deals with the influence of lunar surface roughness on volatile transport, including after a comet impact. Chapter 6 validates the method developed for radiative heat transfer in an unsteady, non-equilibrium atmosphere, and discusses the consequences for an impact-generated atmosphere. Lastly, Chapter 7 synthesizes and summarizes results from previous chapters, before outlining questions for further investigation.

Chapter 2: Literature Review

2.1. CHAPTER OVERVIEW

This chapter begins by reviewing current knowledge of the distribution, abundance and origin of lunar water, focusing on observations of (potential) water ice at the lunar poles, specific observations that suggest a cometary source for this water, and modeling work undertaken to investigate source and delivery mechanisms. In order to provide additional context for Chapters 5 and 6, the subsequent sections discuss previous work related to thermal modeling of rough planetary surfaces, and to modeling radiative transfer in planetary atmospheres.

2.2. DISTRIBUTION, ABUNDANCE AND ORIGIN OF LUNAR WATER

2.2.1. The Search for Cold-Trapped Water

The idea that the coldest parts of the lunar surface may be conducive to the stability of water ice over geological time-scales was first put forth by Watson et al. (1961), and revisited by Arnold (1979). Later observations have verified and mapped the presence of regions with temperatures sufficiently low to cold trap water and other volatiles over geological time scales (Paige et al., 2010); however, the abundance, distribution, composition and origin of polar volatiles remain to be comprehensively understood – the search for cold-trapped water continues.

Several spacecraft and ground-based observation campaigns have sought signs of water ice at the lunar poles. In 1994, the Clementine spacecraft coordinated with the

Deep Space Network to conduct a bistatic radar experiment that suggested the presence of patchy ice deposits in Permanently Shadowed Regions (PSR's) at the South Pole (Nozette et al., 1996). However, reanalysis of the data set by Simpson and Tyler (1999) found the observed signatures to be more consistent with high surface roughness, as also inferred by Stacy et al. (1997) from Earth-based observations using the Arecibo radar. Shortly after Clementine, the neutron spectrometer on board Lunar Prospector acquired data that indicated enhanced levels of hydrogen at both poles, consistent with 1.5 ± 0.8% (by mass) water at the South Pole, if all the detected hydrogen were in the form of water (Feldman et al., 2000). Subsequently, Haruyama et al. (2008) used SELENE (Kaguya) images to derive an albedo for the permanently shadowed floor of Shackleton crater (illuminated by scattered light), thus ruling out the presence of extensive surface ice cover. Radar imaging of the lunar poles continued with the Mini-SAR instrument onboard Chandrayaan-1, leading to the identification by Spudis et al. (2010) of several 'anomalous' North Polar craters with distinctive radar returns that could be attributed to water ice rather than surface roughness. Soon afterwards came key confirmation of the presence of water ice in at least one cold trap, when the LCROSS mission impacted a PSR in Cabeus crater, near the South Pole of the Moon, excavating material buried several meters below the surface. Analyzing the composition of this debris, Colaprete et al. (2010) estimated a local water concentration of 5.6 ± 2.9% by mass.

Results from Lunar Reconnaissance Orbiter (LRO) continue to provide fresh perspectives on lunar volatiles. LRO Mini-RF radar observations of the LCROSS impact site in Cabeus crater indicate the absence of a thick layer of ice within the depth (< 2.5 m) sampled by LCROSS (Neish et al*.,* 2011), suggesting that the water detected was present in a more distributed form, consistent with the lower mass fraction inferred by Feldman et al. (2000). Spudis et al. (2013) used Mini-RF data to extend their survey of anomalous polar craters likely to harbor water ice by virtue of their distinctive radar returns and location in regions of permanent shadow showing neutron suppression (indicating the presence of hydrogen). Laser altimetry and reflectance measurements from LOLA, another LRO instrument, have found the floor of Shackleton crater to be brighter than surrounding terrain (Zuber et al., 2012). While this could be accounted for by the presence of surface ice, considering the measurements in conjunction with Mini-RF data, Zuber et al. infer that reduced space weathering of the shadowed crater floor seems a more likely explanation for the enhanced brightness. Meanwhile, far-ultraviolet images acquired by the LAMP instrument (Gladstone et al*.,* 2012) show variations in albedo within PSR's, consistent with the presence of 1-2% (by area) water frost. Keller et al. (2016) recently reviewed these (and other) contributions of the LRO mission towards understanding the distribution and transport of volatiles on the Moon.

Signs of water have also been observed at lower latitudes. In 2009, instruments on three spacecraft – Chandrayaan-1 (Pieters et al*.,* 2009), Deep Impact (Sunshine et al., 2009) and Cassini (Clark, 2009) – independently detected diurnally varying 3 μm and 2.8 μm absorption features across the lunar surface, which are attributable to water and hydroxyl, respectively. These observations suggest the presence of a globally distributed, mobile population of hydrogenated volatiles, likely to be hydroxyl radicals implanted by solar wind bombardment of the lunar regolith (McCord et al., 2011), and perhaps also water. Recently, the LRO LEND instrument (a neutron spectrometer) has also detected signs of diurnally varying hydration (Livengood et al., 2015).

2.2.2. Comets as a Source of Lunar Water

Determining the source(s) of lunar polar volatiles is a question of major interest (National Research Council, 2007), with implications for both science and exploration. Water in particular could have reached the lunar surface in a number of different ways: through outgassing from the lunar interior, through solar wind bombardment of the regolith, or through impacts of volatile-bearing bodies – from micrometeoroids to comets. More detailed reviews of various source mechanisms may be found in work by Arnold (1979), Morgan and Shemansky (1991) and Basilevsky et al. (2012).

Several observations support the hypothesis that comet impacts may have contributed to the present-day lunar volatile inventory. Notably, species detected after the LCROSS impact at the Cabeus cold trap included not only H_2O, but also CH_4, NH_3 and other compounds commonly found in comets (Colaprete et al., 2010). More recently, Miller et al. (2014) revisited neutron spectroscopy data from the Lunar Prospector mission and identified some cold traps with a sub-surface hydrogen signature, but no corresponding surficial signature. This may imply delivery of the detected hydrogen (possibly water) by some ancient, episodic source – such as an impact. Surficial deposits laid down by such a source could be buried by subsequent impact gardening (Crider and Vondrak, 2003; Hurley et al., 2012) or migrate to the subsurface under favorable thermal conditions (Schorghofer and Taylor, 2007).

Observations also indicate that water ice, if present, appears to be heterogeneously distributed between cold traps, with some regions of permanent shadow lacking signs of water (Mitrofanov et al., 2010 & 2012; Gladstone et al., 2012). This is somewhat puzzling because source mechanisms that rely on collisionless migration of molecules to the poles (for instance, solar wind generated volatiles may reach cold traps in this manner) should lead to uniform filling of cold traps, since the average ballistic hop distance is greater than typical cold trap dimensions. Several theories as to why cold traps may be non-uniformly filled have been developed. Siegler et al. (2014) model the evolution of the temperature of the lunar poles over the past 2-3 Ga and find that past thermal conditions may have favored the accumulation of ice in different regions than those favored under present thermal conditions. Siegler et al. (2016) extend this analysis by combining thermal modeling with Lunar Prospector Neutron Spectrometer data to make a compelling case that the antipodal, polarly offset nature of hydrogen deposits at the North and South Poles is consistent with a change in the orientation of the Moon's spin axis (true polar wander), suggesting that hydrogen-bearing volatiles may have been deposited and sequestered in a different, past polar thermal environment.

Others have explored the idea that the apparent variation in hydrogen (perhaps water) content could be due to the nature of the source. Schorghofer (2014) uses a Monte Carlo model for the collisionless transport of water molecules after a nominal impact (modeled as a point source) and finds that the latitude, though not the longitude, of the impact influences cold trap deposition patterns; viz., cold traps at each pole are uniformly filled, but the pole closer to the location of impact accumulates thicker deposits. Using a similar model, Moores (2016) found that for equatorial impacts, cold traps at lower latitudes tend to accumulate more water, as migrating molecules become progressively less mobile with decreasing surface temperature at higher latitudes. These results suggest that the observed heterogeneities in volatile abundance between different cold traps may be partly due to the nature of volatile transport and deposition after an impact, as well as differences in subsequent thermal evolution.

2.2.3. Modeling

Analyses of remote sensing data have been complemented by the development of numerical models that seek to understand and constrain the nature of cold-trapped water (and other volatiles) by modeling various source, transport and loss mechanisms. Most investigations have focused on the collisionless migration of exospheric molecules of varying origin, well-represented by the work of Butler (1997) and Crider and Vondrak (2000 & 2002), who have used Monte Carlo methods to model the transport of solar wind-generated hydrogen and water to polar cold traps, tracking the migration of molecules from a globally distributed surficial source, through collisionless hops, until capture or photodestruction. Butler estimated that ~20-50% of globally distributed water molecules could migrate to regions of stability near the lunar poles. Crider and Vondrak (2000) used a different source function, temperature map and more recent estimates for cold trap surface area, and found the fraction of cold-trapped water molecules generated by solar wind bombardment to be ~4.2%. Some subsequent works (e.g. Ong et al., 2010) have applied these estimates to sources other than those modeled by the original authors.

Monte Carlo simulations have also been performed by Schorghofer (2014) and Moores (2016), using a point source of molecules to approximate the release of volatiles by an impact. As discussed in Section 2.2.2, these simulations indicate that the location of the impact and the nature of the migration process could lead to non-uniform cold trap capture in the collisionless limit.

Others have focused on quantifying the amount of impact-generated vapor that remains gravitationally bound to the Moon for various impact parameters – these results may be combined with knowledge of the historical impact flux to estimate a cometary (or asteroidal) contribution to the lunar volatile inventory. For instance, Berezhnoi and Klumov (1998) sought to estimate the amount of water that could be delivered by comets to lunar polar cold traps, based on analytical approximations of how much impact-generated vapor would remain gravitationally bound given comet size, density and impact velocity. Assuming that all gravitationally bound water would eventually be cold-trapped, they concluded that the impact of a single comet ~2 km in diameter would be sufficient to account for the amount of water-equivalent hydrogen inferred from Lunar Prospector data. More recently, Ong et al. (2010) addressed this question in greater detail, using hydrocode simulations to study the dependence of volatile retention on impact velocity by tracking the fraction of non-escaping projectile material for a series of vertical impacts at different velocities. Integrating over an estimated velocity distribution, they find that ~6.5% of the total lunar impact mass flux is retained.

In addition to the work discussed above, numerous more general modeling studies of impact processes (i.e. not explicitly concerning lunar volatiles) have also been conducted. For instance, Pierazzo and Melosh (2000) carried out a set of hydrocode simulations of oblique impacts at varying angles, focusing on the fate of the projectile. They find that at most impact angles, a cometary nucleus would be subject to pressures and temperatures more than sufficient to completely vaporize constituent ices. This finding was reaffirmed by Svetsov and Shuvalov (2015) in their later hydrocode modeling of a range of asteroid and comet impacts. (In an interesting contrast, Svetsov and Shuvalov find that at low impact velocities, hydrated material from asteroids tends to remain in the vicinity of the resultant impact crater, while cometary material vaporizes and is globally dispersed.) Pierazzo and Melosh's simulations also show increased kinetic energy partitioning into projectile material at low (i.e. more grazing) angles of impact, and preferential motion of projectile material in the downrange direction, post-impact. Similar energy partitioning as a function of impact angle is also found in simulations by Artemieva and Shuvalov (2008) and Gisler et al. (2006). These studies are of particular interest here for their focus on the fate of the projectile; many of the other existing studies – experimental (e.g. Schultz, 1996), numerical (e.g. Elbeshausen et al., 2009) and empirical (e.g. Housen and Holsapple, 2011) – are different in scope in that they focus on the crater formation process or characterize impact ejecta more generally, without drawing a distinction between target and projectile material.

The fraction of gravitationally bound impact-generated vapor that ultimately reaches a cold trap in the aftermath of an impact is determined by the loss rate and the gas dynamics of volatile transport in the collisional, transient, impact-generated atmosphere. This problem was first modeled by Stewart et al. (2011) who combined the SOVA hydrocode with the DSMC method to model a single impact in detail. The modeling extended from the instant of impact out to several days afterwards, by which time volatile transport returns to the collisionless limit. The primary objective of Stewart et al. was to determine how much water from the simulated comet impact was transported to polar cold traps. Considering a comet composed of solely water ice, 2 km in diameter, impacting the Moon with a velocity of 30 km/s at a 45° angle (relative to the tangent plane), they found that ~3% of the comet's mass remained gravitationally bound, and ~0.1% was ultimately captured by polar cold traps. This result was found to be largely insensitive to impact location. Although Stewart et al.'s work represents the most detailed treatment of post-impact gas dynamics to date, it should be noted that the SOVA-DSMC simulations involved several simplifications.

One major simplification was the pristine composition of the comet, and the modeling of only a single species; i.e., H_2O. In reality, comets are composed of a variety of species; additionally, photochemistry and other reactions among impact-delivered species and dissociation products may give rise to a still more complex mixture of compounds. Other authors have modeled this chemistry in detail, without focusing on gas dynamics; e.g. Berezhnoi and Klumov (2000) model several reactions that may occur in an impact-generated atmosphere, assuming a constant temperature and a specified initial atmospheric composition, until an equilibrium composition is reached. They infer that the composition of cold trap deposits should be equivalent to this equilibrium atmospheric composition, which is different from the assumed composition of the impactor. It should be noted that Berezhnoi and Klumov's model is "zero-dimensional" in that it does not account for spatial variations in the properties of the transient atmosphere. Another factor that may influence the rates of photochemical reactions was noted by Arnold (1979), viz., when the impact-generated atmosphere is sufficiently dense, a substantial amount of material may be shielded from photolysis – this has not been modeled in any of the work discussed in this section. Stewart et al. (2011) also assume that no condensation or radiative heat transfer occurs in the vapor cloud. Some of the simplifications discussed above are revisited in this work.

2.3. THERMAL MODELING OF ROUGH PLANETARY SURFACES

The transport and sequestration of volatiles on nominally airless solar system bodies, such as the Moon, is intimately linked to the distinctive surface thermal environments that these bodies host. Low gravity and a relative dearth of weathering processes can preserve extremely rough surfaces over which illumination conditions vary dramatically. Thermal conductivity is often low and, in the absence of significant atmospheric heat flow, illumination conditions can create and maintain strong temperature gradients at a range of scales. Large-scale temperature gradients are observable from orbit (e.g. Paige et al., 2010), but sharp gradients may also exist at much smaller scales, below the spatial resolution of orbital instruments.

Detailed thermal modeling of a rough lunar surface appears to have first been conducted by Buhl et al. (1968a, 1968b), who calculate temperature distributions within spherical (bowl-shaped) craters of specified depth-to-diameter ratios. In the first paper (Buhl et al., 1968a), surface elements of the crater wall are modeled to be in radiative equilibrium with incident fluxes from the Sun and from other surface elements in view. Treating the surface of the Moon as densely covered by millimeter to centimeter-scale craters, and using the computed temperature distributions, they demonstrate that variations in the observed infrared flux with viewing angle in such a model could explain certain radiometric observations. Based on approximate values for the conductivity of the lunar regolith, Buhl et al. (1968a) estimated that temperature differences of 100 K could exist across craters as small as 1 mm in diameter. They raise the very pertinent point that, due to these small-scale variations, *"one should be very careful about what is meant by temperature with respect to infrared observations of the [Moon]"*, since the brightness temperature inferred from infrared observations is an average over a distribution of surface temperatures. In the second paper (Buhl et al., 1968b), shadowing effects and conduction of heat into the sub-surface are incorporated into the model in order to investigate the cooling of cratered surfaces during the lunar night or eclipse. Recently, Keihm et al. (2015) applied a similar "micro-crater" model of surface roughness to Vesta, in order to deduce the asteroid's thermal inertia.

Of particular relevance among recent works investigating how small-scale surface roughness affects the thermal environment on airless bodies, Bandfield et al. (2015) use brightness temperature measurements from the Diviner radiometer (onboard LRO) to study the small-scale roughness of the lunar surface. They find that the degree of anisothermality (i.e. small-scale temperature variations) over most of the lunar day side corresponds to a distribution of slopes that can be characterized by an RMS slope angle of 20°, whereas the night side shows little anisothermality. This result is based on a comparison of the Diviner measurements to a thermal model that considers the lunar surface as composed of a Rayleigh distribution of adirectional slopes (i.e. slopes relative to the surface normal) and models surfaces to be at radiative equilibrium with respect to radiation from the Sun and from surrounding surfaces (modeled as flat, and also at radiative equilibrium). Bandfield et al. also use a probability function derived by Smith (1967) to account for the fractional surface area in shadow. Since their final results are relatively insensitive to the precise temperature of colder surfaces, shadowed surfaces are simply specified to be at 100 K. In the same work, Bandfield et al. also use a more detailed, two-dimensional thermal model including sub-surface conduction (similar to Williams et al., 2013) to constrain the length scales associated with Diviner-measured anisothermality. They find that surfaces separated by as little as 0.5 cm may differ in temperature by as much as 145 K. Comparing temperatures obtained using the radiative equilibrium and diffusion models, the assumption of radiative equilibrium is found to be reasonably accurate for calculating the temperatures of illuminated surfaces.

Using similar techniques, Hayne et al. (2013) have investigated the consequences of lunar surface roughness for volatile stability, and find that small-scale cold traps, O(10 cm) in size, may constitute a reservoir for water ice comparable in extent to the larger polar cold traps. Hayne and Aharonson (2015) extend this analysis to Ceres by studying the influence of roughness (at a range of scales) on ice stability using a one-dimensional heat diffusion model, which accounts for sub-surface conduction as well as surface radiative fluxes. They combine this model with a stochastic treatment of surface roughness – similar to that of Bandfield et al. (2015), but at meter to kilometer length scales. The radiative flux calculation accounts for orbital variations in insolation, and the flux from surrounding surfaces is computed using an expression derived by Aharonson and Schorghofer (2006). As in Bandfield et al., this approach involves approximating the surroundings as flat. Hayne and Aharonson also model the temperatures of permanently shadowed crater interiors on Ceres. They estimate the fractional area covered by permanent shadows through an approach developed by Bussey et al. (2003) for the Moon, and then calculate the temperature of these shadowed regions using their heat diffusion model. The surface boundary condition in this case is an expression derived by Ingersoll et al. (1992) for the radiative flux received by shadowed surfaces within spherical craters. Rubanenko et al. (2016) build on this work by undertaking more detailed thermophysical modeling of PSR's in rough/cratered terrain – again motivated by the consequences of surface roughness for volatile stability.

Davidsson et al. (2015) provide a good overview of various methods of modeling rough surfaces (and associated temperature distributions), including the concave spherical segment ("micro-crater") model and the random Gaussian surface roughness model, characterized by a Gaussian distribution of unidirectional (two-dimensional) slopes or equivalently, a Rayleigh distribution of adirectional (three-dimensional) slopes (Shepard et al., 1995). Davidsson et al. evaluate these models from the perspective of interpreting planetary surface thermal emission measurements, and find that the statistical models compare favorably to more realistic (and computationally expensive) thermophysical models. They also show that a random Gaussian surface roughness model provides the best match to measurements of lunar radiance as a function of solar incidence angle.

Besides affecting the *stability* of volatile ices, small-scale temperature variations due to surface roughness may also influence volatile *transport* on airless bodies with collisionless exospheres or collisional but rarefied atmospheres, permanent or temporary (such as a transient atmosphere generated by a comet impact). Surface temperature has been recognized to be an important parameter in volatile transport calculations, due to its influence on the residence time of molecules on the surface, and the distribution of velocities with which molecules leave the surface. The surface temperature of the Moon in particular has been modeled with increasing levels of detail as computing power and knowledge of lunar thermophysical properties have grown.

The initial work of Butler (1997) included a longitudinally averaged model for surface temperature, which allowed for variation of the day-side temperature with latitude (only); the night-side was modeled to be arbitrarily cold, i.e. molecules landing on the night-side were assumed to remain immobile until sunrise. Subsequently, Crider and Vondrak (2000) modeled surface temperature, T, as a function of solar incidence angle, μ; viz., $T(\mu) = 280\cos^{1/4}\mu + 100$ [K], where the $(\frac{1}{4})^{\text{th}}$ power dependence is associated with radiative equilibrium. Stewart et al. (2011) use a similar form of this expression, with the constant term set to 120 K instead of 100 K. Observations and detailed thermal modeling of diurnal variations in lunar surface temperature, with depth- and temperature-dependent density and conductivity (Vasavada et al., 2012), show that day-side temperatures are indeed very close to radiative equilibrium. However, the expressions discussed above do not capture the gradual cooling of the surface during the lunar night, which requires accounting for the regolith’s finite thermal inertia. In Schorghofer’s (2014) simulations of exospheric water, surface temperature is calculated using a one-dimensional thermal model (assuming a smooth surface), which provides accurate results when appropriate thermophysical properties are specified, but is also computationally intensive – more so if small- or large-scale topography is taken into account. Hurley et al. (2015) develop a more computationally tractable model by finding an analytical expression for lunar surface temperature (as a function of latitude and time of day), best-fit to averaged temperature measurements from the Diviner instrument. They then apply a Gaussian distribution of longitudinal offsets to this expression in order to simulate the effects of large-scale topography. Using this "roughened" surface temperature map, Hurley et al. show that the inclusion of roughness results in significant changes in exospheric structure at the dawn terminator. This surface boundary condition has been used to model the lunar helium and argon exospheres (Hurley et al., 2016 and Grava et al., 2015, respectively).

It should be noted that none of the volatile transport simulations discussed above have considered the influence of realistic small-scale roughness on surface temperature (e.g. the intent of Hurley et al., 2015 is to find a best-fit approximation for the effect of large-scale topography). Meanwhile, the more physically realistic (albeit statistical) rough surface temperature models of Bandfield et al. (2015), Hayne and Aharonson (2015) and others have not previously been coupled to simulations of volatile transport.

2.4. COMPUTATIONAL METHODS AND MODELS FOR RADIATIVE TRANSFER

As discussed in Chapter 1, the interaction of radiation with an impact-generated atmosphere (particularly radiative heat transfer) is a topic of interest for several reasons.

Later in this work, I develop a shielding algorithm to account for the attenuation of solar energy, and implement a Monte Carlo method to address the radiative heat transfer problem. This section provides a brief overview of previous work related to this task, focusing on the modeling of radiative transfer in planetary science and engineering contexts (from cometary atmospheres to atmospheric re-entry), on Monte Carlo methods for radiative transfer, and the coupling of radiative transfer to DSMC simulations.

The modeling of radiative transfer in cometary atmospheres (comae) is particularly relevant to the present work due to the rarefied nature of these atmospheres and the prominent role of the water molecule. Gombosi et al. (1986) provide an excellent review of contemporary work on modeling dust and gas in comae, including a section on radiative transfer. Some of the earliest such work focuses on the excitation and emission characteristics of water molecules, due to the importance of these processes in controlling the temperature of the coma – particularly the inner coma, where collisions are more frequent and thus, rotational/vibrational energy is readily converted to translational energy. Shimizu (1976) computed a temperature-dependent rotational (far infrared) cooling rate for water molecules, later updated by Crovisier (1984). In order to approximate radiative trapping in the dense inner coma, these expressions may be scaled by a factor of $e^{-\tau}$, where τ is a local optical depth (Gombosi et al., 1986; Huebner, 1985). Other factors contributing to the thermodynamics of the inner coma include radiative heating of the gas by dust grains and photolytic heating due to energetic species (charged and neutral) produced by photodissociation. Marconi and Mendis (1986) include both of these aspects in their model, which is notable for the range of physics considered.

Most of the models discussed by Gombosi et al. involve the solution of systems of differential equations, with appropriate source terms for radiative heating/cooling. More recently, the DSMC method has emerged as an effective means to model steady and unsteady gas and dust dynamics in comae. The DSMC-based model of Combi (1996) is representative of much of the work done in the years since, and is particularly relevant for its inclusion of radiative cooling, coupled to gas dynamics. In Combi's approach, the rotational excitation state of each simulated molecule is represented by a rotational energy, equivalent to some rotational temperature; each molecule loses rotational energy at a rate determined by its rotational temperature. Although the cooling rate used (Crovisier, 1984) assumes thermal equilibrium, non-equilibrium effects are approximated by the non-thermal distribution of rotational energies. During collisions, molecules exchange rotational and translational energy, and radiative cooling is thus coupled to gas dynamics. Optical depth effects are modeled through an "escape probability" formulation (Huebner and Keady, 1984), in which the radiative cooling rate is scaled by the likelihood that emitted radiation escapes to space. Combi also notes that for temperatures below ~1000 K, the vibrational excitation/de-excitation rate of water molecules is sufficiently low as to be negligible.

The approach to coupling radiative cooling and gas dynamics described above has also been adopted in subsequent DSMC simulations of comae (e.g. Tenishev, 2008). Additionally, Zhang et al. (2003) modified the DSMC code used for this work to handle the rotational cooling of SO_2 in volcanic plumes on Io in a similar manner, although the simulated plumes were assumed to be optically thin at the wavelengths associated with rotational emission. Zhang also modeled vibrational cooling, by tracking molecular excitation levels for the three vibrational modes of SO_2 and computing the probability of spontaneous emission during each computational time step based on the Einstein coefficients for various transitions. Absorption was estimated to be more significant at the wavelengths associated with vibrational emission, and the trapping of vibrational radiation was approximated by implementing an “opacity switch”, i.e., specifying a threshold density below which all radiation was assumed to escape to space, and above which all radiation was assumed to be locally reabsorbed (Zhang, 2004).

A major challenge in modeling radiative transfer is the development of methods that can both address optical depth effects (i.e. the attenuation and trapping of radiation) and be applied to unsteady, asymmetric, non-equilibrium problems. The “escape probability” formulation mentioned above is one way to account for optical depth effects; an extended “coupled escape probability” formulation allows a similar approach to be applied to more complex problems. For example, Gersch and A’Hearn (2014) use such a method to model radiative transfer (accounting for both solar radiation and gas-gas transfer) in a coma with non-uniform properties and jet-like morphologies. Since the main objective of Gersch and A’Hearn is to compute observable spectra, their radiative transfer calculation is a steady-state one, uncoupled to gas dynamics.

An alternative to analytical formulations such as the above is to adopt Monte Carlo methods. The great advantage of using Monte Carlo methods for radiative transfer is the versatility with which they can be adapted to suit a variety of problems in a broad range of fields. What follows is a representative, but by no means exhaustive, compilation of previous work implementing such methods to address problems similar in scope to this work.

Modest (2003) describes in detail the implementation of Monte Carlo methods to solve radiative transfer problems. Broadly, these methods involve the initialization of statistically representative “energy bundles” at appropriate locations (within a bulk volume or at bounding surfaces) and their propagation through an absorbing and/or scattering medium; absorption, scattering or reflection from surfaces may also be included. The tracking of a sufficiently large number of “bundles” allows the radiative flux throughout the medium or at surfaces to be computed. The medium of propagation is typically treated as continuous and divided into computational cells, although an alternative (discussed in detail by Wang and Modest, 2006) is to treat the medium as particulate and model the interaction of rays of radiated energy with these particles. The accuracy of solutions obtained through Monte Carlo methods is determined primarily by the number of energy bundles that are traced.

In some situations, it may be more computationally efficient to use a “backward Monte Carlo method” such as that of Gratiy et al. (2010) in which the flux intensity at some point of interest is obtained by tracing energy bundles *from*, rather than *to*, the point. Gratiy et al. adopt this technique to generate simulated spectra for comparison to observations of Io’s atmosphere, by tracing representative photons “backwards” from the detection instrument. Computational efficiency may also be improved by treating certain model elements deterministically rather than probabilistically; e.g. Debout et al. (2016) trace rays of radiant energy along pre-defined, rather than randomly drawn, directions in their model for radiative transfer in comae, obtaining results that compare favorably with the analytical results of Gersch and A'Hearn (2014) for a similar problem.

Bernes (1979) was one of the earliest to demonstrate the usefulness of Monte Carlo methods for radiative transfer problems, in the context of optically thick interstellar clouds. Salo (1988) explored a problem more closely related to this work, modeling heat transfer to a cometary nucleus from the surrounding dust coma, including incoming solar radiation, thermal re-radiation and scattering within the coma, and reflection of energy from the surface of the nucleus. Hogerheijde and Van der Tak (2000) extended the technique implemented by Bernes (1979) to two dimensions, and introduced several innovative means to accelerate convergence of the (steady-state) solution. They consider multiple gaseous species with energy levels affected by both the radiation field and collisions (represented by collision rate coefficients), and also include radiation from dust in the cloud. Hogerheijde and Van der Tak's Monte Carlo formulation has since been adopted by numerous others; e.g. Lee et al. (2011) use this method to investigate the excitation of water in the coma of Comet 67P/Churyumov-Gerasimenko. Recent work by Roth and Kasen (2015) is representative of further advances in the use of Monte Carlo methods for radiative transfer in which the computed radiation field is coupled to a hydrodynamic model; this work also treats the gas as a continuum, and radiation is coupled to gas dynamics using an implicit finite-differencing scheme.

Monte Carlo methods for radiative transfer have also been coupled to the DSMC method, notably in recent work by Ozawa et al. (2010) and Sohn et al. (2012). These authors carried out coupled DSMC-PMC (Photon Monte Carlo) simulations of the flow field around the Stardust capsule during atmospheric re-entry. These simulations are steady and two-dimensional (axisymmetric). Notable features include a detailed treatment of the spectral distribution of energy, the inclusion of multiple species (charged and neutral) and chemical reactions. Although DSMC is a particle based technique, the PMC calculation is performed using a finite volume approach; i.e. absorption and emission are initially computed on a per cell, rather than a per particle basis. The radiation field is coupled to gas dynamics by dividing the net change in energy per cell between all particles in that cell, assuming equipartition between different modes. Since the calculation is a steady-state one, separate simulations are run to solve for the flow field around the re-entry vehicle at various altitudes. At each altitude, the coupled DSMC-PMC calculation is run until convergence of the solution is achieved.

In summary, radiative transfer in planetary atmospheres has previously been addressed through both analytical and statistical (i.e. Monte Carlo) methods. Complex physical and chemical interactions between multiple species and phases have been modeled, but unsteady and coupled radiation-flow field solutions are rare – more so in situations where the gas dynamic regime is rarefied and particle-based techniques such as DSMC are preferred over analytical or finite element methods.

Chapter 3: Computational Methods and Models[1]

3.1. CHAPTER OVERVIEW

The simulations described in this work were performed by adapting the hybrid SOVA-DSMC method developed by Stewart (2010). I begin this chapter by briefly reviewing this method, and then describe modifications made to the DSMC code in order to model atmospheric self-shielding from photodestruction, surface temperature variations due to small-scale surface roughness, and radiative heat transfer.

3.2. REVIEW OF THE HYBRID SOVA-DSMC METHOD

This section provides a brief overview of the hybrid SOVA-DSMC method developed by Stewart et al. (2009 & 2011) to follow cometary water from impact to permanent shadows – more details may be found in the referenced works. The necessity for a hybrid approach stems from the fact that during the evolution of an impact-generated atmosphere, the flow regime transitions rapidly from continuum to rarefied (and ultimately, to free molecular); the former is best modeled using a hydrodynamic code, while a particle-based technique such as DSMC is more suitable for the latter. The simulations are initiated by using the SOVA hydrocode (Shuvalov, 1999) to model the

---

[1] Parts of Sections 3.2 and 3.3 have previously been published as part of Prem, P., Artemieva, N. A., Goldstein, D. B., Varghese, P. L. & Trafton, L. M., 'Transport of water in a transient impact-generated lunar atmosphere', *Icarus* (2015) and parts of Section 3.4 have been submitted for publication as part of Prem, P., Goldstein, D. B., Varghese, P. L. & Trafton, L. M., 'The influence of surface roughness on volatile transport on the Moon', *Icarus* (2017). P.P. (the author of this dissertation) performed the DSMC simulations in Prem et al. (2015) and the Monte Carlo simulations in Prem et al. (2017), and drafted both manuscripts. N.A.A. was responsible for the SOVA simulations in Prem et al. (2015). D.B.G., P.L.V. and L.M.T. provided useful ideas, suggestions and feedback, and proofread the manuscripts.

phase changes that occur due to the passage of successive compression and rarefaction waves through the target and projectile, and the resultant hydrodynamic flow of molten and vaporized target and projectile material. Most of the results presented in subsequent chapters consider an oblique impact, at an angle of 60° (measured from the horizontal), with an impact velocity of 30 km/s. The lunar surface is assigned the material properties of dunite, and the comet is modeled as a sphere of pure water ice, 2 km in diameter. The only impact parameter varied relative to the simulation of Stewart et al. (2011) is the impact angle – 60° here vs. 45° in the previous work.

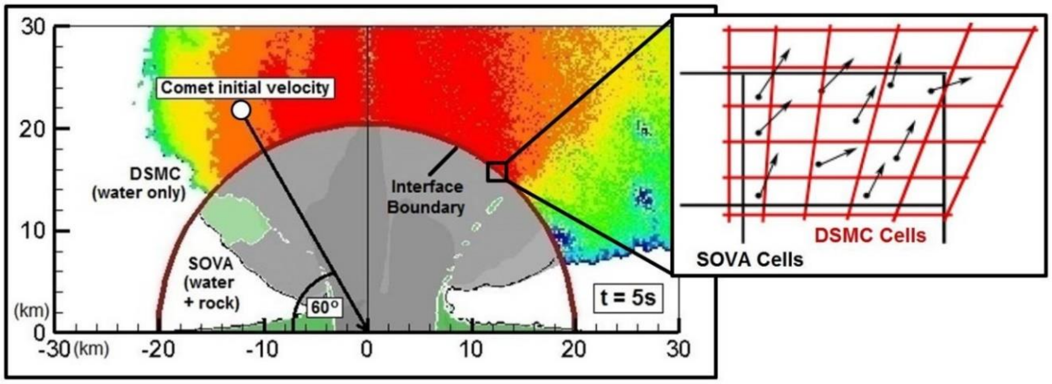

Figure 3.1: Schematic depiction of the hybrid SOVA-DSMC approach, showing a two-dimensional cross-section (in the plane of impact) of SOVA and DSMC density contours, 5 s after a 60°, 30 km/s impact. The initial velocity vector is marked, and the comet is drawn approximately to scale. Also indicated is the boundary of the hemispherical interface separating the SOVA and DSMC computational domains. The inset diagram depicts the overlap between the Cartesian SOVA cells and the spherical DSMC cells at the interface, where DSMC molecules are initialized using continuum SOVA data for water vapor (gray). See Stewart et al. (2009 & 2011) for details.

Hydrocodes use a continuum description of material behavior, which is accurate for the initially dense plume of impact-generated vapor. However, as the plume expands into a near-vacuum background, it undergoes rapid rarefaction and a transition occurs from dense, continuum flow near the point of impact to collisionless flow at the outer fringes of the expanding cloud. Due to the transitional, non-continuum behavior of the impact-generated vapor, the SOVA simulations are limited to a hemispherical domain extending out to 20 km from the point of impact. Beyond this boundary, modeling of impact-generated water vapor is carried out using the DSMC method (Bird, 1994). Representative molecules for the DSMC computation are generated on the basis of continuum properties (density, temperature and velocity) at the SOVA-DSMC interface. Since flow at the interface is predominantly supersonic, there is no reverse coupling of the two codes; i.e. the SOVA domain is unaffected by the DSMC domain. Both SOVA and DSMC simulations are unsteady and three-dimensional, and the DSMC code is parallelized for computational speed (Stewart, 2010; McDoniel, 2015). Figure 3.1 depicts the interfacing between the two codes (Stewart et al., 2009) and the problem set-up.

It should be noted that although the impact-generated plume consists of both water vapor and vaporized or molten rock, for the purposes of this study, I focus on the water vapor component and neglect any water-rock interactions outside the SOVA domain. Given the impact velocity and comet composition specified, virtually all of the projectile is vaporized. The impact-generated vapor is initially heated to temperatures sufficiently high that some dissociation may occur; however, it is probable that dissociation products recombine as the (still dense) vapor cools rapidly during expansion into vacuum. By the time water vapor reaches the interface between the SOVA and DSMC codes, the temperature is well below 1000 K and the pressure is O(1 atm); under such conditions, water molecules should largely be undissociated. Since atmospheric condensation into droplets or ice crystals is not currently modeled, molecules remain in the vapor phase until escape, photodestruction or cold-trap capture.

DSMC is a statistical method that models gas behavior by moving and colliding a large number of representative molecules within a gridded domain. This approach is particularly useful for regimes in which flow is still collisional, but the continuum description breaks down – such as during vapor expansion into vacuum, when a gas may become so rarefied that the mean distance between molecular collisions is larger than characteristic length scales. In these circumstances, gas behavior must be described using the Boltzmann equation, for which no general analytical solutions are available. However, numerical methods such as DSMC have been used for similar problems in planetary science with considerable success. For instance, the DSMC code used in this work has recently been used to model the rarefied atmosphere and volcanic plumes of Io (Walker et al., 2010; McDoniel et al., 2015), as well as water vapor plumes on Enceladus (Yeoh et al., 2015) and Europa (Berg et al., 2016). The accuracy of the DSMC method increases with the number of representative molecules simulated – in the limit of a large number of representative molecules, DSMC collision models have been shown to satisfy the Boltzmann equation collision integral (Nanbu, 1986) and Bird's algorithm has been shown to converge to a solution of the Boltzmann equation (Wagner, 1992).

In the DSMC code, molecules generated at the SOVA-DSMC interface are affected by gravity and Coriolis forces (McDoniel, 2015), and interact with each other through collisions. The DSMC simulations presented here were carried out using $O(10^8)$ particles and $O(10^7)$ cells. As described by Stewart et al. (2011), the simulations are performed in a series of staged computational domains of increasing size to account for the rapid expansion of impact-generated vapor. In the quasi-cylindrical innermost domain (32 km × 32 km × 360°), cells are 100 m × 100 m × 1° in size and the time-step is 0.5×10^{-3} s. Later-stage global simulations of volatile transport are carried out in a domain bounded by two spherical surfaces: the lower boundary represents the lunar surface, and the upper boundary is at an altitude of 40,000 km. Cells are 1° × 2° in size in the azimuthal and polar dimensions respectively, while cell size in the radial dimension increases exponentially from 1 km at the lunar surface to 100 km above an altitude of ~60 km, with a collisionless "buffer" cell ~10,000 km in size to track molecules moving beyond ~40,000 km from the surface. In this domain, the time-step is varied from 1 s to 10 s as the atmosphere becomes more rarefied with time.

Due to the wide range of spatial and temporal scales in the problem, the DSMC simulations are under-resolved (i.e. cell size is larger than the mean free path and time-step is larger than the mean collision time) for much of the atmosphere – in the densest regions, the mean free path is O(0.1 m) even hours after impact. Large cells introduce an unphysical numerical viscosity, which tends to smear gradients in macroscopic properties due to collisions between molecules that are separated by distances considerably larger than the mean free path. In order to reduce this inaccuracy, I use a "free cell" routine (Roveda et al., 2000; Stewart et al., 2011) that preferentially collides nearby molecules in each cell. Although the simulations still remain under-resolved in some regions, we appear to be able to capture gradients in macroscopic properties, such as density and temperature, with reasonable accuracy (Stewart et al., 2009).

At each time-step, the No Time Counter (NTC) scheme developed by Bird (1994) is used to determine the number of pairs of molecules to be selected within each computational cell. Collisions between molecules are then computed using the Variable Hard Sphere (VHS) model, according to which the molecules in each selected pair may or may not collide, depending on their relative velocity. Translational-rotational energy exchange between molecules during collisions is modeled using the standard Larsen-Borgnakke model, while translational-vibrational energy exchange is modeled using the discrete Larsen-Borgnakke model. I also use the collision limiting scheme developed by Stewart et al. (2009), which reduces the computational cost of simulations by accounting for the fact that in regions at local thermal equilibrium, only a limited number of collisions is required to bring the gas to equilibrium; subsequent collisions simply redistribute energy between molecules without affecting macroscopic properties.

Besides gas-gas interactions through collisions, gas-surface interactions are also important. Simulated molecules that come into contact with the lunar surface reside temporarily on the surface and, upon desorption, leave the surface with velocities drawn from a Maxwellian distribution at the local surface temperature. The mean surface residence time, t_{res}, is given by Langmuir (1916) and Frenkel (1924) as:

$$t_{res} = \frac{1}{\nu_0} \exp\left(\frac{E_a}{k_B T_{surf}}\right) \tag{3.1}$$

where $\nu_0 = 2.0 \times 10^{12}$ s^{-1} and $E_a = 6.65 \times 10^{-20}$ J are the lattice vibrational frequency and binding energy, respectively, for a H_2O molecule within a H_2O matrix (Sandford and

Allamandola, 1993); k_B is the Boltzmann constant, and T_{surf} is the local, diurnally varying surface temperature. The main reason for considering a H_2O molecule in a H_2O matrix in this calculation is that the lunar surface should saturate rapidly with several monolayers of water after a comet impact. Furthermore, based on data from the M^3 instrument on Chandrayaan-1, Li and Milliken (2013) estimate surface hydration levels of ~100-500 ppm (thought to be partly indigenous, and partly due to solar wind implantation) even at mid- to low-latitudes, suggesting that parts of the lunar surface may be coated by an adsorbed monolayer of water even prior to a comet impact.

Besides gravitational escape, the primary atmospheric loss processes are photodestruction and cold-trap capture. Cold trap capture is modeled as in Stewart et al. (2011) by tracking and removing from the simulation any molecules that land within seven nominal craters – one at the North Pole, six at the South Pole – with locations and sizes representative of actual cold traps. The treatment of photodestruction in this work differs from that of Stewart et al. (2011) and is described in the following section.

3.3. PHOTODESTRUCTION AND ATMOSPHERIC SELF-SHIELDING

One important change made to the DSMC code for the purposes of this work is the inclusion of atmospheric self-shielding from photodestruction. Stewart et al. (2011) treated the transient atmosphere as optically thin in the ultraviolet i.e. all molecules other than those in the Moon's shadow were assumed to be exposed to unattenuated sunlight. In reality, the atmosphere may be sufficiently dense (and hence, optically thick) that upper, sunward layers absorb a significant part of the solar ultraviolet, reducing the intensity of dissociating radiation that penetrates through to lower layers. More strongly illuminated parts of the vapor cloud are thus preferentially depleted, and the overall rate of photodestruction is reduced. Since the primary loss process for gravitationally bound water is photodestruction, reduced loss rates may significantly increase the probability that water molecules migrate to cold traps during their lifetime.

Atmospheric self-shielding from photodestruction is implemented as follows. The photodestruction rate coefficient, r_{photo} (s^{-1}) in a given computational cell is given by:

$$r_{photo} = (1.2 \times 10^{-5})[0.4 \exp(-nL\sigma_{121.6nm}) + 0.6 \exp(-nL\sigma_{145-186nm})] \qquad (3.2)$$

Here, nL is the density (molecules/m^2) of the atmospheric column that sunlight passes through before it reaches the cell. Dissociation by the 121.6 nm Lyman-α line and by continuum absorption in the 145-186 nm range are considered separately. Based on the work of Crovisier (1989), Eq. (3.2) approximates 40% of photodestruction of H_2O in unattenuated sunlight to be due to Lyman-α and 60% to be due to ultraviolet radiation in the 145-186 nm range. For the quiet Sun, the total unattenuated photodestruction rate of H_2O at 1 AU is 1.2×10^{-5} s^{-1} (Huebner et al., 1992). The term $\sigma_{121.6nm}$ is the Lyman-α absorption cross-section of a H_2O molecule and $\sigma_{145\text{-}186nm}$ is a band-averaged absorption cross-section over the 145-186 nm range, such that:

$$\sigma_{145-186nm} \int B_\lambda(\lambda, T) d\lambda = \int \sigma(\lambda) B_\lambda(\lambda, T) d\lambda \qquad (3.3)$$

where $\sigma(\lambda)$ denotes the absorption cross-section at some wavelength λ and the Sun is approximated as a black body at $T = 5780$ K, such that the solar spectral radiance is given by $B_\lambda(\lambda,T) = (2hc^2/\lambda^5)[1/(\exp(hc/\lambda k_B T) - 1)]$. Based on H_2O absorption coefficients acquired by Watanabe and Zelikoff (1953), $\sigma_{121.6nm}$ is found to be 1.571×10^{-21} m^2 and $\sigma_{145\text{-}186nm}$ is found to be 2.384×10^{-22} m^2. Calculations of column density, nL, are performed periodically to account for changes in atmospheric structure and the position of the Sun. Since the computational domain is divided between processors, the DSMC grid sections contained in each processor are mapped to a single Cartesian grid for the column density calculation. In order to strike an acceptable balance between accuracy and computational speed, the Cartesian grid is non-uniform, but still relatively coarse.

Photodestruction is implemented in DSMC based on the probability (p_{photo}) that a molecule dissociates during a time-step of size Δt, given by:

$$p_{photo} = 1 - \exp(-r_{photo}\Delta t) \tag{3.4}$$

where r_{photo} is the photodissociation rate constant of the cell in which the molecule is located. Molecules are destroyed when a randomly drawn number is less than this probability. Currently, product species are neglected – when a water molecule dissociates, it is simply removed from the simulation. However, it should be noted that reactions involving multiple species could play a significant role in determining the composition and fate of the transient atmosphere, an issue briefly explored in Chapter 4.

3.4. ROUGH SURFACE TEMPERATURE MODEL

This section focuses on the question of how to model "sub-pixel" (i.e. below the resolution of orbital measurements or modeled surface cells) roughness in a physically realistic way for volatile transport simulations. This is an important question because thermal models primarily intended for other purposes (such as matching brightness temperature measurements) may be less suited to modeling gas-surface interactions. Section 3.4.1 discusses the development of an appropriate rough surface temperature model for this work. Section 3.4.2 presents a brief comparison of the model to other approaches to modeling rough surface temperatures, and Section 3.4.3 discusses non-equilibrium effects and small-scale permanent shadow – two factors that are not explicitly included in the present model. Lastly, Section 3.4.4 describes the coupling of the rough surface temperature model to simulations of volatile transport.

3.4.1. Development of a Rough Surface Temperature Model

In order to develop a thermal model for a rough surface, it is first necessary to specify the magnitude and scale of the roughness of interest. Although large-scale temperature gradients may be larger in magnitude, migrating molecules sample the lunar surface down to the smallest scales, as a result of which even small-scale temperature gradients may play an outsize role – influencing volatile transport and exospheric structure on a global scale. Thus, the most fundamental scale of roughness important for simulations of volatile transport is the smallest scale over which significant temperature gradients can be maintained. (Molecules may also interact with a rough surface at even smaller scales, on the order of the interstitial spaces between unconsolidated regolith grains, leading to residence times and molecular velocities that are not determined by temperature alone, but in this work, I consider only the thermal effects of roughness.)

Based on the findings of Bandfield et al. (2015), small-scale temperature variations over the lunar night side are neglected, and the lunar day side is modeled as having a Rayleigh distribution of adirectional slopes (Shepard et al., 1995) characterized by a RMS slope angle of 20°. As inferred by Bandfield et al., the degree of small-scale roughness is modeled to be uniform over the lunar maria and highlands. This is also consistent with trends observed by others (e.g. Rosenburg et al., 2011) who find that differences in roughness between geologic units diminish with decreasing length scale, suggesting that small-scale roughness is generated by a global, ongoing mechanism such as micrometeoroid impacts or other processes.

The orientation of each sub-pixel surface within every rough day-side pixel is determined by sampling an adirectional slope from the specified Rayleigh distribution, and an azimuthal orientation about the mean (pixel) surface normal. Together, these angles define the local (sub-pixel) surface normal vector, as illustrated by Figure 3.2. Once the orientation of a sub-pixel surface has been determined, its temperature can be computed. Since the Moon is a slow rotator, surfaces may be assumed to be in equilibrium with radiation from the Sun and surrounding surfaces. The solar contribution depends on the local solar incidence angle (determined by latitude, time of day and the local surface orientation) while the contribution from surrounding surfaces depends on the temperature of those surfaces and their view factors with respect to the location of interest. Since detailed modeling of the latter is computationally intractable given the scope of the global simulations of volatile transport, I adopt an approximate approach by modeling the incident flux from the surroundings as dependent only on mean solar incidence angle (a measure of the mean temperature of surrounding surfaces), and independent of local surface slope. This assumption is not strictly valid for any specific location, but should hold true on average for a random distribution of slopes and elevations – for instance, a flat (zero slope) surface may be situated at a relative topographic low or high, receiving more radiated and scattered energy from surrounding surfaces in the former case.

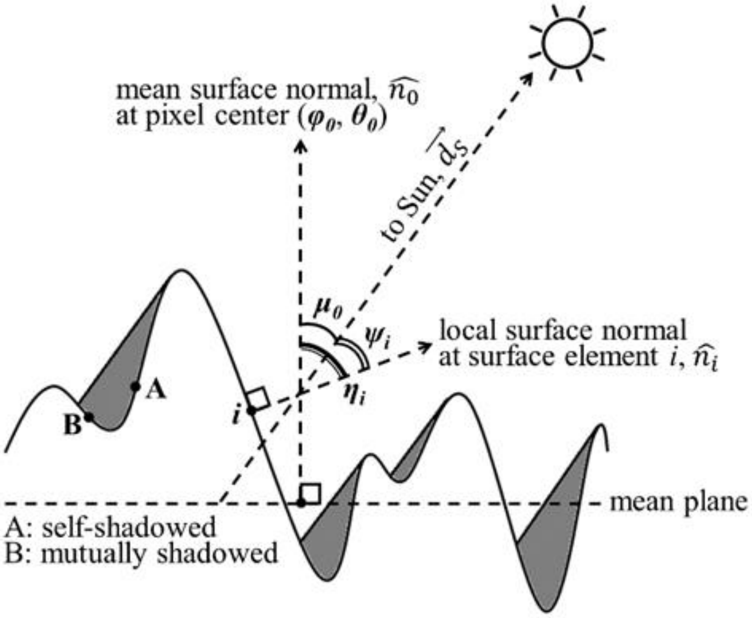

Note: $\hat{n}$, $\widehat{n_i}$ and $\overrightarrow{d_S}$ may not lie in the same plane ∴ in general, the slope angle $\eta_i \neq \mu_0 + \psi_i$; $\mu_0 \equiv$ mean solar incidence angle; $\psi_i \equiv$ local solar incidence angle.

Figure 3.2: Schematic of a stochastically rough surface, illustrating various important angles and terms. Shading indicates regions of shadow. Note that this is a two-dimensional representation of a three-dimensional surface.

Sub-pixel surfaces may also be shadowed, in two ways – when the Sun dips below the local horizon (self-shadowing) or when other surfaces obstruct sunlight (mutual shadowing). Self-shadowing can be determined, again, by the mean solar incidence angle and local surface orientation, while the probability of mutual shadowing depends only on the mean solar incidence angle for a specified degree of roughness, as derived by Smith (1967). Taking all of the above into account, the temperature T_i of a (day-side) sub-pixel surface i can be approximated by:

$$\varepsilon\sigma T_i^4 = (1-\alpha)F_S\cos\psi_i + F_{surr}\cos\mu_0 \tag{3.5}$$
$$T_i \geq T_{i,min}$$

where ε = 0.95 and α = 0.11 are the emissivity and albedo of the lunar surface, respectively; the solar constant F_S = 1366 W/m^2 (for illuminated surfaces) or zero (for shadowed surfaces); ψ_i denotes the local solar incidence angle at sub-pixel surface i and μ_0 denotes the mean solar incidence angle at the center of the pixel. The term $(1-\alpha)F_S\cos\psi_i$ represents the direct solar flux incident at sub-pixel surface i, while $F_{surr}\cos\mu_0$ represents the incident scattered/radiated flux from surrounding surfaces. T_i is constrained to be greater than or equal to a specified threshold temperature, $T_{i,min}$ to avoid the temperature of shadows approaching 0 K at low mean solar incidence angles.

This approach differs from others primarily in that the quantity F_{surr} is assumed to be a constant, independent of local surface slope (as discussed above) such that incident flux from surrounding surfaces depends only on the mean solar flux (for scattered solar energy) and the mean surface temperature to the fourth power (for re-radiated solar energy), both of which are proportional to $\cos\mu_0$. Having assumed this form for the flux from surroundings, the value of F_{surr} is constrained (for the specified degree of roughness) by the consideration that the bolometric brightness temperature of any pixel, integrated over all constituent sub-pixel surfaces, should match the observed bolometric brightness temperature at that latitude and time of day, T_{obs}; i.e. it is required that:

$$T_{obs} \approx [\varepsilon(\Sigma_i T_i^4 \cos\eta_i)/(\Sigma_i \cos\eta_i)]^{1/4} \tag{3.6}$$

where η_i is the slope of sub-pixel surface i, such that the $\cos\eta_i$ terms account for the tilt of sub-pixel surfaces with respect to the mean surface normal. The bolometric brightness temperature, T_{obs}, is defined by Paige et al. (2010) as the wavelength-integrated radiance expressed as the temperature of an equivalent blackbody.

It should be noted that the approach described above considers only small-scale stochastic roughness superimposed on a spherical lunar surface, and does not account for temperature variations caused by large-scale topography. Large-scale thermal gradients could be incorporated by making use of the excellent altimetry data and illumination models that are available, but I did not do so in this work – partly to control computational cost, but also to isolate the influence on volatile transport of roughness at the smallest scales. Given this simplification, Hurley et al.'s (2015) analytical expression for lunar surface temperature is used to check the physical consistency of the model. Hurley et al.'s expression is a fit to Diviner radiometer observations that averages out the influence of large-scale topography such that the observed bolometric brightness temperature T_{obs} is well-approximated by:

$$T_{obs} = 392\cos^{1/4}\mu_0 \geq 130\text{ K} \qquad \text{for } \mu_0 < 90° \text{ (day-side)} \tag{3.7a}$$

$$T_{obs} = \Sigma_{j=0,..,5}\left(a_j \varphi_0^j\right) + 35(\sin\theta_0 - 1) \qquad \text{for } \mu_0 > 90° \text{ (night-side)} \tag{3.7b}$$

where φ_0 is longitude ($\varphi_0 = \pi$ at midnight) and θ_0 is co-latitude (from 0 to π) at the pixel center, and $a = [444.738, –448.937, 239.668, –63.8844, 8.34064, –0.423502]$.

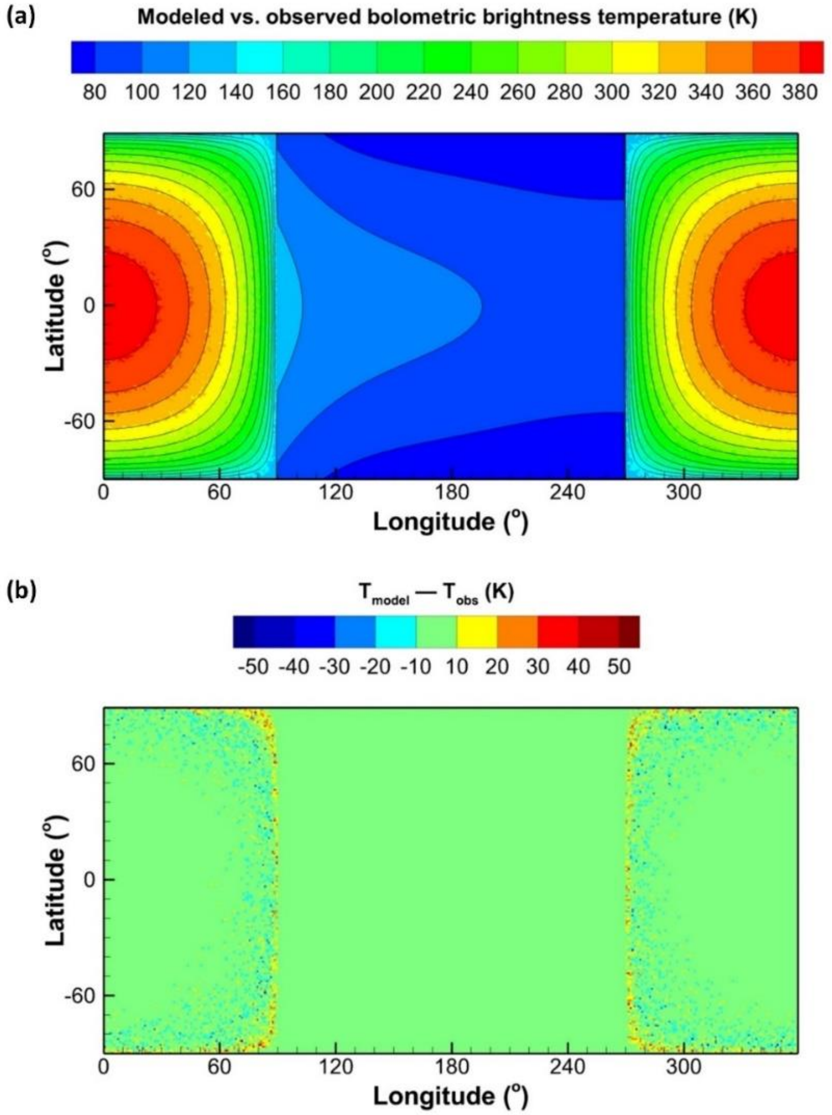

Figure 3.3: (a) Bolometric brightness temperature (indicated by color contours) map composed of 1° by 1° pixels with sub-pixel temperature distributions modeled according to Eq. (3.5), compared to the analytical fit to observations derived by Hurley et al., 2015 (indicated by line contours). (b) Difference between modeled and observed bolometric brightness temperatures, T_{model} and T_{obs}, corresponding to the right-hand side and left-hand side of Eq. (3.6), respectively.

Since the lunar night side shows little anisothermality, night-side temperatures are modeled directly using Eq. (3.7b), which accounts for the gradual cooling of the surface during the night due to the thermal inertia of the regolith. Analytic day-side temperatures computed using Eq. (3.7a) are compared against modeled pixel brightness temperatures. By varying the values of the constants F_{surr} and $T_{i,min}$ in Eq. (3.5) when computing day-side, sub-pixel surface temperatures, it is possible to find best-fit values of these constants, which minimize bolometric brightness temperature differences between our model and Hurley et al.'s fit to observations and satisfy the constraint specified in Eq. (3.6). For the specified degree of roughness (RMS slope angle = 20°), the best-fit values are found to be F_{surr} = 250 W/m^2 and $T_{i,min}$ = 130 K – the latter a direct consequence of the 130 K day-side temperature minimum imposed by Eq. (3.7a) at the terminator.

As shown in Figure 3.3, bolometric brightness temperatures mapped using the rough surface temperature model described above (with best-fit values of F_{surr} and $T_{i,min}$) are largely within ± 10 K of Hurley et al.'s fit to observations, with deviations most pronounced near the terminators, but generally less than the 10-50 K magnitude of error inherent in neglecting the influence of large-scale topography (also most pronounced near the terminators). The small-scale temperature variations in the model are thus largely consistent with larger scale brightness temperature measurements from orbit.

3.4.2. Comparison to Other Rough Surface Temperature Models

In this section, I briefly compare the model developed in the preceding section to other rough surface temperature models, developed for other purposes. In general, all models include the term $(1 - \alpha)F_S\cos\psi_i$ in Eq. (3.5) to account for the solar flux incident on a sloping surface i, and some models also account for orbital variations of the solar constant F_S. The main difference between other models and ours lies in how we model the radiative flux from surrounding surfaces, specifically the term F_{surr} in Eq. (3.5).

Based on previous work by Aharonson and Schorghofer (2006), Hayne and Aharonson (2015) develop an expression for the flux incident on a sloping surface due to thermal emission from flat surroundings, in which the term equivalent to F_{surr} is given by:

$$F_{surr} = (1 - \alpha)F_s\sin^2(\eta_i/2) \tag{3.8}$$

where the factor $\sin^2(\eta_i/2)$ accounts for the increase in view factor between a sloping surface and flat surroundings as the slope (η_i) increases. Although Eq. (3.8) works well when surrounding surfaces can be reasonably represented as flat, when dealing with a random distribution of slopes and elevations, the view factor between any given surface and its surroundings is, on average, independent of slope (as discussed in Section 3.4.1). Moreover, the approximation of surroundings as flat is questionable in such a situation, particularly at the small scales that are of interest here.

It is found that computing F_{surr} using Eq. (3.8) instead of using the best-fit value of F_{surr} = 250 W/m^2 in Eq. (3.5) results in a poorer match to the observed bolometric brightness temperature, as shown in Figure 3.4(a), suggesting that the approach developed here may be a more physically accurate way to model small-scale temperature variations due to surface roughness, particularly when independently obtained slope distribution data and brightness temperature measurements are available to constrain the value of F_{surr}. From Figures 3.4(b) and 3.4(c), it can be seen that Eq. (3.8) provides sub-pixel temperature distributions broadly similar to ours at higher temperatures and low solar incidence angles, but with significant differences at lower temperatures and high solar incidence angles.

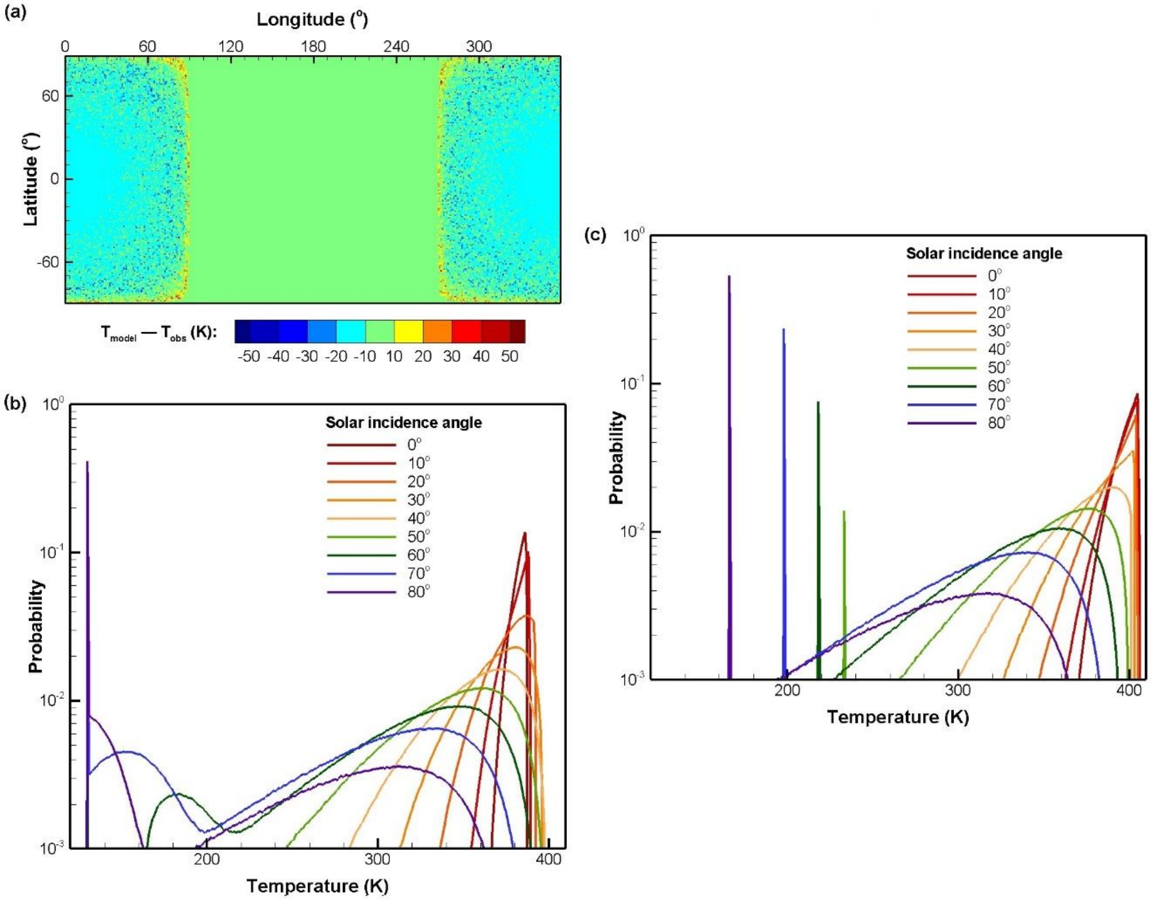

Figure 3.4: (a) Difference between modeled and observed bolometric brightness temperatures when Eq. (3.8) is used to compute radiative flux reaching a sub-pixel surface from its surroundings; (b) Sub-pixel temperature distributions for various mean solar incidence angles from Eq. (3.8) and (c) from Eq. (3.5), using $F_{surr} = 250$ W/m^2.

Ultimately, the importance of model accuracy depends on the purpose of the modeling. As a case in point, Bandfield et al. (2015) used Eq. (3.8) with a fixed shadow temperature of 100 K to infer the magnitude of the small-scale lunar roughness modeled here. However, in that work, the purpose of modeling sub-pixel temperature distributions was to compute the total emitted flux, a quantity that is largely determined by higher sub-pixel temperatures (since flux ∝ T_i^4). Furthermore, Bandfield et al. found that their model best matched measurements of surface anisothermality at relatively low solar incidence angles (< 45°), with significant deviations at higher incidence angles. Since sub-pixel temperatures at high temperatures and low solar incidence angles have a similar frequency distribution in both our model and that of Hayne and Aharonson (2015), similar results would likely have been obtained with either model. However, in simulations of volatile transport, the residence time of molecules on the planetary surface increases exponentially with decreasing surface temperature ($t_{res} \propto \exp(1/T_i)$) and is disproportionately influenced by lower sub-pixel temperatures, particularly shadow temperatures – which have significantly different frequencies and values in our model compared to that of Hayne and Aharonson.

Eq. (3.5) more closely resembles an expression derived by Ingersoll et al. (1992) for the surface temperature inside spherical craters, in which the term equivalent to F_{surr} is given by:

$$F_{surr} = (1 - \alpha)F_s f[\varepsilon + \alpha(1 - f)]/(1 - \alpha f) \tag{3.9}$$

where $f = 1/(1 + 1/4b^2)$

Here, the term b is the ratio of crater depth to diameter; unlike Eq. (3.8), this expression has no dependence on local slope. Comparing Eq. (3.9) to Eq. (3.5), it can be found that the best-fit value of $F_{surr} = 250$ W/m^2 yields shadow temperatures corresponding to the temperatures of shadowed regions within spherical craters having $b = 0.245$. It is interesting to note that this value falls within the range of measured depth-to-diameter ratios (Brownlee et al., 1973) for craters generated by micrometeoroid impacts – thought to be a candidate mechanism for generating globally distributed small-scale roughness. However, it should also be noted that the temperature distributions obtained using Eq. (3.5) are different from those that would be obtained by assuming a surface saturated with spherical micro-craters as in Buhl et al. (1968a).

3.4.3. Non-Equilibrium Effects and Permanent Shadows

In modeling sub-pixel temperatures as described in Section 3.4.2, two major assumptions are made regarding shadowed surfaces. Namely, (i) shadowed surfaces are assumed to be in instantaneous radiative equilibrium with their surroundings i.e. surfaces that enter shadow cool instantaneously to the shadow temperature (determined by latitude and time of day), while surfaces that come out of shadow warm instantaneously to the illuminated temperature (determined by latitude, time of day and local slope); and (ii) all shadows are assumed to be temporary, i.e. any small-scale permanent shadows are not explicitly modeled. This section discusses these simplifications in more depth.

Due to the slow rate of rotation of the Moon, the assumption of radiative equilibrium is acceptable for illuminated and self-shadowed regions, where surface temperature increases or decreases slowly with solar incidence angle. However, mutually shadowed regions behave somewhat differently. The assumption of radiative equilibrium remains valid between dawn and mid-day, during which time shadows warm gradually as their surroundings also become warmer – again, at a rate sufficiently slow that radiative equilibrium can be maintained throughout the warming process.

The main deviations from radiative equilibrium occur between mid-day and dusk, as illuminated sub-pixel surfaces become mutually shadowed. In our model, these surfaces cool instantaneously to the radiative equilibrium shadow temperature, whereas in reality, the cooling process takes a finite length of time, determined by radiation and sub-surface heat conduction. To constrain the time-scales involved, I constructed a simple, one-dimensional thermal model to solve the differential equations governing surface temperature evolution, using Vasavada et al.'s (1999) 'two-layer' model for the thermophysical properties of lunar regolith. This solver was used to model cooling rates of a representative range of illuminated surfaces that suddenly enter shadow, warmed only by flux from surrounding surfaces, of the form $F_{surr}\cos\mu_0$. The cooling time-scale was found to be ~2 hours, only weakly dependent on the initial surface temperature. This implies that each modeled pixel contains a mixture of 'old shadows' (surfaces that entered shadow more than 2 hours ago) at radiative equilibrium, and 'new shadows' (surfaces that entered shadow less than 2 hours ago) spanning a range of temperatures between the peak illuminated surface temperature and the radiative equilibrium shadow temperature. The relative proportion of 'old' and 'new' shadows can be computed from Smith's (1967) probability of mutual shadowing, denoted hereafter by $p(t)$ at a time t. The probability that a mutually shadowed region is 'new' (i.e. has been shadowed for less than 2 hours) at time t is given by:

$$p_{new}(t) = [p(t) - p(t - \Delta t_{cool})]/p(t) \tag{3.10}$$

where $p(t) = 1 - \frac{1}{\Lambda(\mu(t))+1}$ from Smith (1967),

with $2\Lambda(\mu(t)) = \sqrt{\frac{2}{\pi}} \cdot \frac{w}{\mu(t)} e^{-\frac{[\mu(t)]^2}{2w^2}} - \mathrm{erfc}\left(\frac{\mu(t)}{\sqrt{2}w}\right)$ and $\mu(t) = \cot\mu_0(t)$

Here, Δt_{cool} is the cooling time-scale, which is taken to be 2 hours; w is the RMS slope = tan(20°) and $\mu_0(t)$ is the mean solar incidence angle at time t.

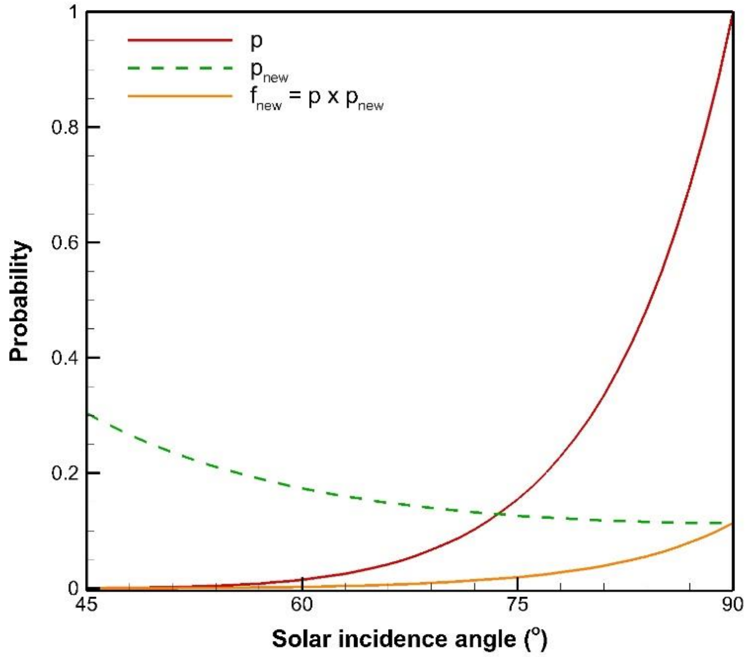

Figure 3.5: Probability of mutual shadowing p, probability of a given mutual shadow being ‘new’ p_{new}, and fractional surface area covered by ‘new’ mutual shadows f_{new} as functions of longitude at the equator (a proxy for solar incidence angle). Shadowing is negligible at solar incidence angles below 45°.

Figure 3.5 shows p, p_{new} and f_{new} (the fractional surface area covered by ‘new’ mutual shadows) as a function of solar incidence angle – equivalent to longitude at the equator. It can be seen that at any given time, the majority of sub-pixel shadows are likely to be at the radiative equilibrium shadow temperature. In addition, as ‘new’ shadows become more prevalent closer to dusk, the difference between the temperatures of illuminated and shadowed surfaces becomes less significant. It should be noted that p_{new} depends on the rate of rotation of the body in question. Over 2 hours, the Moon rotates only ~1°, resulting in only a small change in shadowing probability. On more rapidly rotating bodies, it cannot be assumed that most shadows at any given time are at radiative equilibrium – it may be required to track the evolution of the fraction f_{new} of shadows from the illuminated temperature to the radiative equilibrium shadow temperature.

Besides the assumption on instantaneous radiative equilibrium, it is also assumed that all small-scale shadows are temporary, with no explicitly specified regions of permanent shadow or cold traps on the scale of the modeled roughness (although larger cold traps are included, as described in Section 3.2). For stochastic small-scale roughness superimposed on a smooth surface, the fraction of the surface in permanent shadow at any given latitude may be approximated by the fraction of the surface in shadow at noon at that latitude, which can be obtained by substituting latitude for the solar incidence angle in Smith’s (1967) expression for shadowing probability. In this scenario, the fraction of the surface in permanent shadow increases from 5% at 60° latitude to 100% at 90° latitude. However, the actual incidence of small-scale permanent shadow is likely to be determined by large-scale topography, which calls for an additional level of modeling (e.g. Bussey et al., 2003; Hayne and Aharonson, 2015) that I do not undertake here.

It should be noted that the mere *presence* of shadows may not be sufficient to have a significant influence on volatile migration – the critical factor is likely to be the *temperature* of shadows. Currently, all shadowed sub-pixel surfaces within a given pixel are approximated as having the same temperature, determined by latitude and time of day as discussed in Section 3.4.1. In reality, there is likely to be a distribution of shadow temperatures, due to both non-equilibrium effects and the presence of permanent shadow (Rubanenko et al., 2016). Detailed thermal modeling of stochastically rough surfaces is beyond the scope of this work, but to examine how uncertainties in modeling shadow temperature influence our results, I conducted a separate simulation ('Case 2' in Table 3.1) in which an arbitrary 1% of shadows at any given time were set to be at the pre-dawn temperature at that latitude, introducing small, temporary cold spots that could be considered an approximate representation of doubly shadowed regions.

3.4.4. Coupling Roughness to Monte Carlo Simulations of Volatile Transport

In order to investigate the consequences of small-scale surface roughness for gas dynamics, I conduct a series of five Monte Carlo simulations with different surface boundary conditions, summarized in Table 3.1. Each simulation is initialized by distributing 100 kg of H_2O (in the form of ~3×10^7 representative molecules) uniformly over the lunar surface. This initial condition is not intended to accurately represent any specific source mechanism, but simply to gauge the influence of roughness on volatile transport without biasing results by introducing a localized source of volatiles. As described in Section 3.2, molecules have a mean surface residence time that depends on the local temperature, given by Eq. (3.1). The precise values of v_0 and E_a for the lunar regolith are uncertain, although recent work (e.g. Poston et al., 2015) on the energetics of

H_2O desorption from lunar regolith samples provides useful constraints. To illustrate the sensitivity of results to the uncertain energetics of desorption, I run an additional simulation ('Case 3' in Table 3.1) using a different value of E_a.

#	**Title**	**Nature of Surface**	**Desorption Energy**
1	Case 1-S	Smooth	0.415 eV (Sandford & Allamandola, 1999)
2	Case 1-R	Rough	
3	Case 2	Rough with "deep shadows" (1% of shadows at any given time are at dawn temperature)	
4	Case 3-S	Smooth	0.456 eV (10% higher than S & A, 1999)
5	Case 3-R	Rough	

Table 3.1: Description of Monte Carlo simulations conducted. Case 1 investigates the consequences of our rough surface temperature model for volatile transport. Cases 2 and 3 examine the sensitivity of our results to the temperature of small-scale shadows, and the energetics of water molecule desorption from the lunar regolith, respectively.

Since the modeled exosphere in Cases 1-3 is very tenuous (with mean free paths larger than the radius of the Moon), collisions between molecules can be neglected. However, much of the other physics is modeled as described in Section 3.2. Upon desorption, water molecules leave the lunar surface with velocities drawn from a Maxwellian distribution at the local surface temperature. They then travel ballistically, influenced only by variable gravity, and either return to the surface or cross the upper boundary of the spherical computational domain, 10,200 km above the lunar surface. Gravitational escape is not explicitly modeled, but any molecules that leave the computational domain are considered to escape and removed from the simulation – the exospheric scale height is O(100 km), so this approach should not greatly overestimate escape. Molecular trajectories are tracked using time-steps of ~10 s in order to accurately resolve the ballistic time of ~100 s. While aloft, water molecules may undergo photodestruction, with a rate coefficient of 1.2×10^{-5} s^{-1} (Huebner et al., 1992). Dissociation products are not modeled and the atmosphere is sufficiently thin that any attenuation of destructive solar ultraviolet radiation is negligible. As mentioned in Section 3.2, cold trap capture is modeled by tracking and removing from the simulation any molecules that land in seven specified cold traps. The temperature of these regions is not explicitly modeled and is unaffected by the introduction of surface roughness.

Rather than maintaining a global map of sub-pixel surface temperature, the rough surface temperature model described in Section 3.4.1 is coupled to the Monte Carlo simulations described above (and subsequently, to full-scale DSMC simulations of post-impact volatile transport) through the interaction of simulated molecules with the lunar surface. Gas-surface interactions are implemented as depicted in Figure 3.6. Whenever a molecule strikes the lunar surface, we sample the two angles that determine the orientation of the surface at that location and, based on the mutual shadowing probability at that location and time, specify whether or not the surface is in mutual shadow at that time. At the next time-step, the mutual shadowing probability changes; molecules that were previously resident on shadowed surfaces may (or may not) come out of shadow, and molecules that were previously resident on illuminated surfaces may (or may not) become shadowed. Unlike mutual shadowing, which is computed probabilistically, self-shadowing at each time-step is simply determined based on the surface orientation relative to the solar incidence angle at that time.

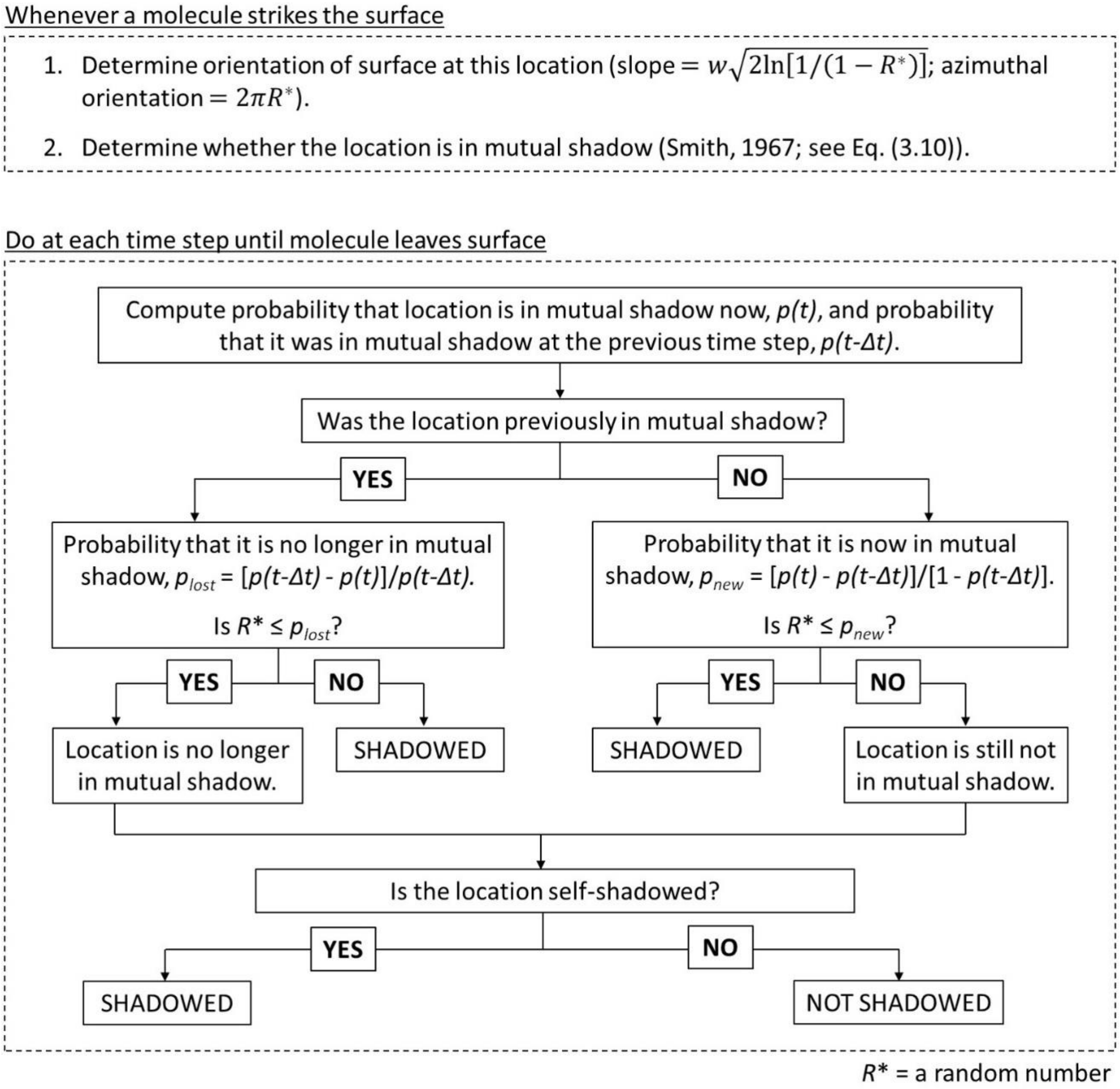

Figure 3.6: Flowchart describing the algorithm through which representative molecules in our Monte Carlo simulations sense small-scale shadows.

Once a location has been determined to be shadowed or illuminated, the local surface temperature is determined according to Eq. (3.5). Based on the surface temperature, molecules may desorb or reside on the surface, such that the mean residence time at a given temperature is given by Eq. (3.1). This approach generally ensures that molecules which reside on the lunar surface for several time-steps sense an appropriate change in temperature during that time. It should be noted that the assumption of instantaneous radiative equilibrium (discussed in Section 3.4.2) may cause some molecules to desorb prematurely as shadowed surfaces that become illuminated warm instantaneously, rather than at a finite rate. However, the consequences of this for overall exospheric structure and transport are expected to be minimal.

3.5. RADIATIVE HEAT TRANSFER

The last major addition to the DSMC code for the purposes of this work was a model for radiative heat transfer, tailored to a rarefied, three-dimensional, asymmetric, temporally evolving impact-generated atmosphere. Sections 3.5.1 to 3.5.5 describe the implementation of this model. (Validation of the model and the influence of radiative heat transfer on post-impact volatile transport are discussed in Chapter 5.) Section 3.5.6 describes a simplified approach to rotational cooling adopted for the simulations described in Chapter 4. Finally, Section 3.5.7 discusses the treatment of vibrational cooling. Most of the standard equations in these sections (unless otherwise specified) may be found in the textbook by Penner (1959).

3.5.1. Coupling Radiative Heat Transfer to the DSMC Simulations: an Overview

There are three primary aspects to the radiative heat transfer problem: (i) the attenuation and reabsorption of spontaneously emitted molecular radiation; (ii) the attenuation and absorption of radiation from the lunar surface; and (iii) the attenuation and absorption of solar radiation. In order to couple these processes to the DSMC simulation, the net rate of atmospheric heating or cooling due to mechanisms (i)-(iii) is computed at appropriately spaced time intervals (during which flow field temperature and density should not change significantly). For the wavelengths considered here (see Section 3.5.2), this corresponds to a net gain or loss of molecular rotational energy for each computational cell in the DSMC simulation. Once this calculation has been performed, the average rotational energy of each cell is modified accordingly at each subsequent time-step. Knowing the average rotational energy of a cell ($\overline{e_{rot}}$), the rotational temperature of the cell, T_{rot}, may be defined (Bird, 1994) as:

$$\overline{e_{rot}} = \frac{\zeta_r}{2} k_B T_{rot} \tag{3.11}$$

The rotational energies (e_{rot}) of simulated molecules within each computational cell are then sampled from the Boltzmann distribution at the rotational temperature T_{rot}, which has the following form:

$$f(e_{rot}) = \frac{1}{\Gamma(\zeta_r/2) k_B T_{rot}} \left(\frac{e_{rot}}{k_B T_{rot}}\right)^{\frac{\zeta_r}{2}-1} \exp(-\, e_{rot}/k_B T_{rot}) \tag{3.12}$$

In the equations above, Γ denotes the gamma function, ζ_r is the number of rotational degrees of freedom ($\zeta_r = 3$ for H_2O) and k_B is the Boltzmann constant.

After molecule rotational energies have been sampled and assigned, this rotational energy may be exchanged with other molecules and other internal modes during the next collision step, thereby raising or lowering the total temperature of the gas. The major assumption behind this approach to modeling radiative heat transfer is that molecular rotational energies have a Boltzmann distribution, corresponding to thermodynamic equilibrium. Although this may not strictly be the case, the Larsen-Borgnakke model for kinetic-internal energy exchange used in the DSMC code also generates Boltzmann energy distributions. However, non-equilibrium effects are represented, in that the rotational temperature may be different from the translational and vibrational temperatures. As discussed in Chapter 2 (Section 2.3), Combi (1996) adopts a similar approach when modeling radiative cooling in cometary atmospheres.

3.5.2. Preliminary Considerations and Simplifying Assumptions

The key step in solving the radiative transfer problem is the computation of net atmospheric heating/cooling rates due to the mechanisms outlined above. As mentioned before, the DSMC simulations are highly parallel, with the computational domain divided between several hundred processors. Relatively few molecules move between processors at any given time-step, keeping the communication overhead under control. However, radiation propagates almost instantaneously and in all directions throughout the entire domain – and the amount of radiation reaching any point depends on the path traveled. As a first step in parallelizing the radiative transfer problem, all simulated molecules are sorted on to a relatively coarse Cartesian grid (for convenience, the same grid used in Section 3.3. to handle atmospheric self-shielding from the solar ultraviolet), and the radiative heat transfer calculation is performed on this grid. The number of molecules, and the average translational and rotational temperatures in each Cartesian grid cell are sampled, and this information is disseminated to all processors. Solving for the attenuation and absorption of radiation in a three-dimensional domain with non-uniform density and temperature fields is further complicated by the fact that the wavelengths at which molecules absorb and emit depend on the local temperatures. Due to the complexity of the problem, a photon Monte Carlo approach is adopted.

In order to calculate radiative heating/cooling rates, it is first necessary to define a wavelength range of interest. The characteristic temperatures for the two vibrational stretching modes of water are 5268 K and 5410 K, while the characteristic temperature for the vibrational bending mode is 2298 K (Penner, 1959). The simulations indicate that the temperature of the comet impact-generated atmosphere is sufficiently low that vibrational modes are practically inactive. Therefore, I consider the 212 strongest rotational lines (with strengths greater than 10^{-20} $\mathrm{cm}^{-1}/(\mathrm{molecule}/\mathrm{cm}^2)$) for H_2O in the ground vibrational state at 300 K, a temperature representative of warmer regions of the atmosphere in the calculations without radiative heating. (Most of the atmosphere is at much lower temperatures, where the contribution from only a few of these lines dominates.) The lines considered fall in the far-infrared to microwave region and correspond to a wavenumber range from 18.58 to 525.96 cm^{-1} i.e. 538.21 to 19.01 μm. Absorption line strengths (in $\mathrm{cm}^{-1}/(\mathrm{molecule}/\mathrm{cm}^2)$) and the associated lower level energies (in cm^{-1}) are obtained from the online HITRAN database, and this information is provided as input to the DSMC code.

Although the impact-generated atmosphere is collisional, local pressures are generally very low – $O(10^{-8})$ bar at most. At pressures this low, collision broadening of lines can be neglected. However, Doppler broadening of lines due to relative translational motion of molecules is taken into account. At a translational temperature T_{tr}, the Doppler half-width at half-maximum γ_D of a line centered at frequency ω_0 is given by:

$$\gamma_D = \left[\frac{2k_B T_{tr}\ln(2)}{mc^2}\right]^{\frac{1}{2}} \omega_0 \tag{3.13}$$

where m is the mass of the molecule under consideration ($m = 29.9 \times 10^{-27}$ kg for H_2O) and c is the speed of light. Lines may also be Doppler shifted due to bulk relative motion between regions of photon emission and absorption. For a bulk velocity difference Δv, the Doppler shift $\Delta\omega_0$ of a line originally centered at frequency ω_0 is given by:

$$\Delta\omega_0 = \frac{\Delta v}{c}\omega_0 \tag{3.14}$$

Considering the density and velocity fields of the transient atmosphere at representative times during the DSMC simulation, the magnitude of the Doppler shift is inferred to be much smaller than the Doppler half width of the lines considered (i.e. bulk velocity gradients between locations of photon emission and absorption are small, particularly in dense, strongly absorbing regions of the atmosphere – where the effects of radiative heat transfer are in general most important). Thus, Doppler shifts are neglected in the present computations.

3.5.3. Attenuation & Reabsorption of Spontaneously Emitted Molecular Radiation

Spontaneous emission by the molecules within a cell is modeled by dividing each Doppler-broadened spectral line profile into three wavenumber bins spanning the range from $\omega_0 \pm 3\gamma_D$, as shown in Figure 3.7. The number of bins and the wavenumber range may be adjusted to strike an appropriate balance between computational accuracy and speed. The amount of energy ϵ_{bin} (in W/molecule) emitted in each bin is given by:

$$\epsilon_{bin} = \frac{S_{ul}(T_{rot})}{\gamma_D}\sqrt{\frac{\ln(2)}{\pi}}\exp[-(\omega_{bin}-\omega_0)^2\ln(2)/{\gamma_D}^2]\cdot\Delta\omega \tag{3.15}$$

where $S_{ul}(T_{rot})$ is the strength (in W/molecule) of the emission line centered at frequency ω_0, at the cell rotational temperature T_{rot}, ω_{bin} is the frequency at the bin center, and $\Delta\omega$ is the width of the bin ($\Delta\omega = 2\gamma_D$ when three bins are specified) . At the temperatures and pressures considered, even Doppler-broadened lines remain sufficiently narrow that they do not overlap – therefore, the energy emitted in each wavenumber bin comes only from a single line. The emission line strength $S_{ul}(T_{rot})$ is related to the absorption line strength $S_{lu}(T_{rot})$ for the transition between lower level l and upper level u. Based on the principle of detailed balance, this relationship can be expressed as:

$$S_{ul}(T_{rot}) = S_{lu}(T_{rot})\frac{8\pi hc^2{\omega_0}^3}{\exp(hc\omega_0/k_BT_{rot})-1} \tag{3.16}$$

Given the rotational temperature of the cell, T_{rot}, the strength of each absorption line at that temperature, $S_{lu}(T_{rot})$, can be calculated from the reference absorption line strength $S_{lu}(T_0)$ at $T_0 = 300$ K as:

$$S_{lu}(T_{rot}) = S_{lu}(T_0)\frac{\exp(-E_l/k_BT_{rot})}{\exp(-E_l/k_BT_0)}\frac{Q_{rot}(T_0)}{Q_{rot}(T_{rot})}\frac{[1-\exp(-hc\omega_0/k_BT_{rot})]}{[1-\exp(-hc\omega_0/k_BT_0)]} \tag{3.17}$$

where E_l is the energy (in J) of the lower level, $Q_{rot}(T_{rot})$ denotes the rotational partition function at the temperature of interest, and h is Planck's constant. Given a reference value of the partition function $Q_{rot}(T_0)$ at temperature T_0, $Q_{rot}(T_{rot})$ can be approximated, according to Verdes et al. (2005), as:

$$Q_{rot}(T_{rot}) = Q_{rot}(T_0)\left(\frac{T_{rot}}{T_0}\right)^{\frac{3}{2}} \tag{3.18}$$

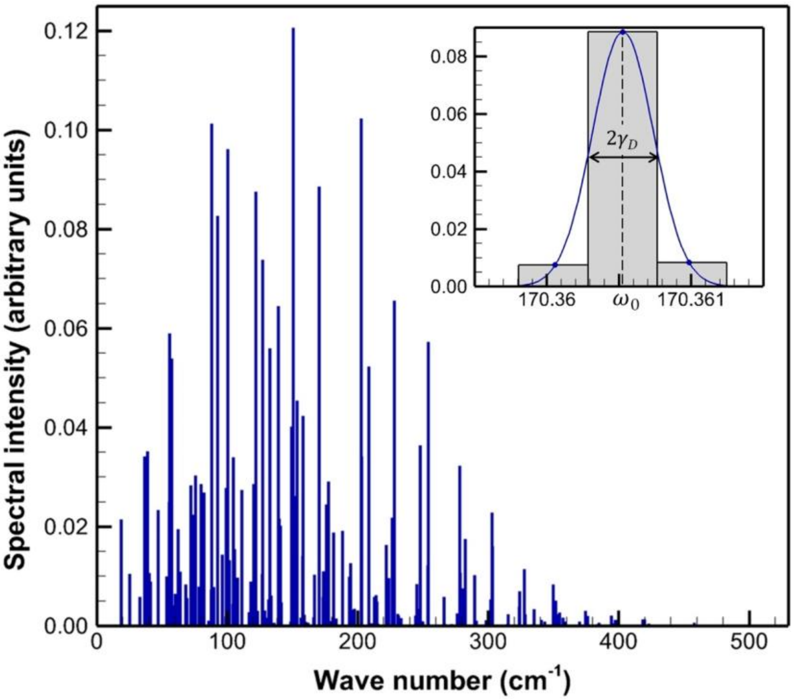

Figure 3.7: The spectrum of water vapor at 300 K, with Doppler-broadened line profiles. The inset figure illustrates how each line is divided into three (or more, if desired) wavenumber bins, each associated with a discrete frequency. Energy packets are generated at each of these frequencies and propagated throughout the medium. Similar wavenumber bins are used to compute absorption.

By combining Eq.'s (3.15) through (3.18), it is possible to compute the total radiative cooling rate (in W/molecule) as a function of temperature (assuming translational and rotational temperature to be equal). Figure 3.8 compares the computed radiative cooling rate to the rate expression for radiative cooling of water vapor given by

Gombosi et al. (1986), based on the work of Crovisier (1984), as well as an earlier rate expression derived by Shimizu (1976). It is seen that the rate computed here differs by a factor of 0.5-2.5 from Gombosi et al.'s expression over the temperature range shown. This may be due to differences between the wavelength ranges considered or the databases used (GEISA by Crovisier, 1984 vs. the current version of HITRAN here).

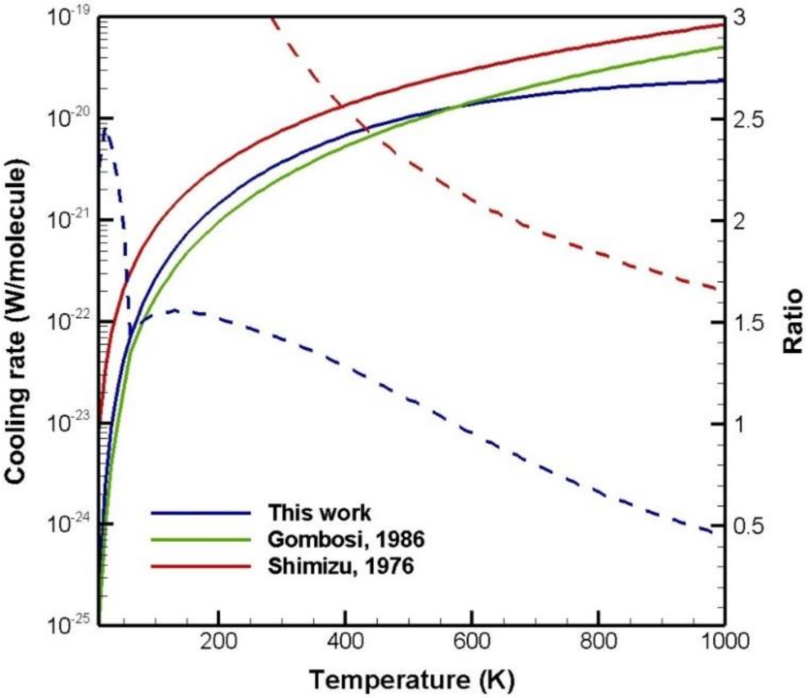

Figure 3.8: Equilibrium radiative cooling rate for H_2O as a function of temperature computed in this work, compared to earlier expressions given by Shimizu et al. (1976) and Gombosi et al. (1986). The dashed blue and red lines show the ratio of the cooling rates in this work and that of Shimizu et al., respectively, to that of Gombosi et al.

The total energy spontaneously emitted (in each wavenumber bin, per unit time) within a cell is obtained by multiplying ϵ_{bin} by the number of molecules in that cell. This energy is divided among a specified number of energy packets that are then propagated throughout the computational domain. Random numbers are drawn to determine the starting point of each packet and the direction of propagation, assuming isotropic emission and uniform spatial distribution of packets within the cell of origin. Each energy packet is moved along the chosen path through spatial steps sufficiently small in size that a packet cannot cross more than two cells in any coordinate direction during a single step. Since scattering of energy by water molecules is neglected, the direction of propagation does not change between successive steps. During any given step, an energy packet may remain in the same cell or cross over to an adjoining cell.

The amount of energy absorbed within each cell depends on the path length of propagation within that cell. The rate of radiative heating, ϵ_{abs} (in W) is given by:

$$\epsilon_{abs} = \epsilon_{packet}[1 - \exp(-nLk)] \tag{3.19}$$

where L is the path length of propagation (in a given cell) of a packet with energy ϵ_{packet}, n is the number density of absorbing molecules (in molecules/m^3) in that cell and k is the molecular absorption cross-section (in m^2/molecule). After travelling a distance L, the packet energy reduces to a value ϵ'_{packet}, which is given by:

$$\epsilon'_{packet} = \epsilon_{packet} \exp(-nLk) \tag{3.20}$$

Energy packets are tracked until they are completely absorbed (i.e. until ϵ'_{packet} drops below some reasonably small threshold energy) or cross the boundaries of the computational domain. When the energy of a packet drops below the specified threshold value, propagation is ended and the residual energy is absorbed by the cell that the packet is in (provided that the cell is not empty). It should be noted here that the propagation of energy is treated as instantaneous, an approach that may introduce slight discrepancies. For instance, in the simulations presented here, the radiative heat transfer calculation is performed for a spherical computational domain 80,000 km in diameter; photons may traverse this domain in ~0.27 s at most, a time-scale that is not negligible (though small) compared to the DSMC time-step size of 1 s.

The absorption cross-section in Eq. (3.20) is a function of wavenumber and temperature for a given gas. Taking Doppler broadening into account, the absorption cross-section $k(\omega, T_{rot})$ is given by:

$$k(\omega, T_{rot}) = \frac{S_{lu}(T_{rot})}{\gamma_D}\sqrt{\frac{\ln(2)}{\pi}}\exp[-(\omega - \omega_0)^2 \ln(2)/{\gamma_D}^2] \tag{3.21}$$

The energy transmission calculations described above are performed for all the specified wavenumber bins and each cell in the (Cartesian) computational domain. Let us denote the rate of radiative heating of a cell i due to the absorption of packets released in that cell by $\epsilon_{abs,i\to i}$ and the rate of radiative heating due to the absorption of packets released by all other cells j ($j \neq i$) by $\epsilon_{abs,j\to i}$. The reason for distinguishing between these two quantities is that $\epsilon_{abs,i\to i}$ depends only on the temperature and density of cell i, while $\epsilon_{abs,j\to i}$ depends also on the temperature and density fields surrounding the cell. During the propagation/absorption calculation, we keep track of both $\epsilon_{abs,i\to i}$ and $\epsilon_{abs,i\to i}$ for every cell, and also compute an opacity factor f_i, defined as:

$$f_i = \epsilon_{abs,i\to i}/\epsilon_{emit,i} \tag{3.22}$$

where $\epsilon_{emit,i}$ denotes the total energy released from cell i (obtained by summing ϵ_{bin}, from Eq. (3.15), over all wavenumber bins and multiplying by the number of molecules in the cell). When $f_i = 1$, a cell is completely opaque i.e. all the energy released within the cell is reabsorbed in the same cell.

Like the main DSMC code, the radiative heat transfer calculation is also parallelized; each processor tracks the propagation of energy packets from an equal share of Cartesian cells. At the end of the propagation/absorption calculation, information is exchanged so that all processors have access to the values of $\epsilon_{abs,i\to i}$ (in W) and f_i for each Cartesian cell i. Since we are ultimately interested in the rate of change of average rotational energy $\overline{e_{rot}}$ for each DSMC cell, the DSMC cell centers are mapped to Cartesian grid cells and $\epsilon_{abs,j\to i}$ is divided by the number of molecules in the Cartesian cell to obtain a heating rate $(\partial\overline{e_{rot}}/\partial t)_{j'\to i'}$ (in W/molecule) for each DSMC cell i'.

The net rate of rotational energy loss or gain (i.e. radiative cooling or heating) for each DSMC cell due to spontaneous emission and reabsorption, $\partial\overline{e_{rot}}/\partial t$ can then be computed at every DSMC time-step as:

$$\partial\overline{e_{rot}}/\partial t = (\partial\overline{e_{rot}}/\partial t)_{j'\to i'} - (1-f_{i'})(\partial\overline{e_{rot}}/\partial t)_{emit,i'} \tag{3.23}$$

The terms $(\partial\overline{e_{rot}}/\partial t)_{j'\to i'}$ and $f_{i'}$ ($\equiv f_i$) in Eq. (3.23) are only computed each time the photon Monte Carlo radiative heat transfer calculation is performed. Due to the computational expense involved, this is not done at every time-step, but at appropriately spaced time intervals (as discussed in Section 3.5.1). However, $(\partial\overline{e_{rot}}/\partial t)_{emit,i'}$, the rate of radiative cooling due to spontaneous emission (obtained by summing ϵ_{bin}, from Eq.

(3.15), over all wavenumber bins) is pre-computed for a range of temperatures, and is updated at every time-step based on the cell temperature(s) at that time.

3.5.4. Attenuation & Absorption of Lunar and Solar Radiation

The attenuation and absorption of energy emitted from the lunar surface is treated in a manner similar to that described above. The primary difference in this case is that energy packets are released from the lunar surface (rather than from within the atmosphere). The lunar surface is discretized into ~1° × 1° cells, each with an appropriate brightness temperature (see Section 3.4). For the radiative heat transfer calculation, I assume that each surface cell behaves as a black surface with an emission spectrum described by the Planck function. Since the calculations limit absorption by water vapor to a certain number of lines, I only initialize and track energy packets within a frequency range of $\omega_0 \pm 3\gamma_{D,ref}$ for each of the lines considered (where $\gamma_{D,ref}$ is the Doppler half-width at half-maximum at 300 K), as opposed to applying the photon Monte Carlo method to the entire black body spectrum. Since the black body spectrum is relatively flat over the widths of the lines considered, the power ϵ_{cell} (in W) emitted from a surface cell with temperature T_{cell} and area A_{cell}, in the frequency range $\omega_0 \pm 3\gamma_{D,ref}$, is given by:

$$\epsilon_{cell} = \frac{2\pi hc^2{\omega_0}^3}{\exp(hc\omega_0/k_B T_{cell})-1} A_{cell} 6\gamma_{D,ref} \tag{3.24}$$

Once again, this energy is divided between a specified number of photon packets that are propagated outward from the lunar surface. Unlike in the case of spontaneously emitted radiation, where packets were associated with discrete frequencies on the line profile, in this case each packet is associated with a line, thus reducing the computational workload. A line profile-averaged absorption cross-section is used to determine how energy carried by these packets is attenuated and absorbed. The line profile-averaged absorption cross-section, $k_{avg}(\omega_0, T_{rot})$, associated with a line centered at frequency ω_0 is computed by dividing the line profile into bins (as in Figure 3.7), such that:

$$k_{avg}(\omega_0, T_{rot}) = \frac{1}{n_{bin}} \sum_{i=1}^{n_{bin}} \frac{S_{lu}(\omega_0, T_{rot})}{\gamma_D} \sqrt{\frac{\ln(2)}{\pi}} \exp[-(\omega_i - \omega_0)^2 \ln(2)/{\gamma_D}^2] \tag{3.25}$$

where n_{bin} is the number of bins (generally three). Once again, energy packets are tracked until they are completely absorbed or cross the boundaries of the computational domain. The lower boundary of the computational domain coincides with the lunar surface; reflection of energy from the surface is neglected and heat transfer from the transient atmosphere to the surface is also anticipated to be negligible (surface temperature is therefore modeled independently). Energy deposited in the atmosphere contributes to the heating term, $(\partial \overline{e_{rot}}/\partial t)_{j' \to i'}$, in Eq. (3.23).

The final contribution to radiative heat transfer included in the model is from solar infrared radiation in the frequency range of interest. Since sunlight can be treated as a unidirectional beam of energy, computation of the attenuation and absorption of solar radiation does not require a Monte Carlo method, and is instead treated in a manner similar to the attenuation of ultraviolet radiation. As done for the calculation of column density in Section 3.3, DSMC molecules are sorted on to a Cartesian grid with one of the grid axes pointing towards the Sun. The incoming (unattenuated) spectrum is computed by treating the Sun as blackbody with temperature 5780 K, at a distance of 1 AU. Again, since the blackbody spectrum is fairly flat over the bandwidths considered, I use line profile-averaged absorption cross-sections computed according to Eq. (3.25). Attenuation and absorption of this energy are computed according to Eq's. (3.19) and (3.20), with the sole difference that the propagated energy is no longer divided into packets. Once again, absorbed energy contributes to the heating term, $(\partial \overline{e_{rot}}/\partial t)_{j' \to i'}$, in Eq. (3.23).

3.5.5. Statistical Considerations

Due to the statistical nature of the DSMC simulations, certain considerations must be kept in mind when conducting the photon Monte Carlo simulations described above. Ideally, all DSMC cells should contain large numbers of simulated molecules to ensure "good" statistics, but this may not always be achieved. In such situations, two issues may arise when coupling the radiative transfer calculation to DSMC simulations.

The first issue relates to the sampling of the DSMC flow field on to a Cartesian grid in order to carry out the radiative transfer calculation. If Cartesian grid cells are too small, this may result in a noisy sampling of temperature(s), particularly near the axis of the spherical DSMC grid, where cells are smaller and contain fewer simulated molecules. Noise in the sampled temperature field can lead to unrealistic computed rates of radiative heating/cooling, which may exacerbate the initial noise in an unstable way. Other than ensuring that each DSMC cell contains a sufficiently number of molecules, this issue can also be addressed by constraining Cartesian grid cells to be sufficiently large that noise in the DSMC solution is averaged out when sampled on to the Cartesian grid.

A second statistical issue arises when sampling molecular rotational energies from the Boltzmann distribution described by Eq. (3.12). If there are too few molecules in a cell, the sampled energies may not accurately represent the rotational temperature defined by Eq. (3.11), such that the average rotational energy of the cell is incorrectly updated – leading in turn to incorrectly computed rates of radiative heating/cooling. To avoid this situation, I check at every time-step that the change in average rotational energy of molecules within a cell remains consistent with the computed radiative heating/cooling rate. If sampled molecular rotational energies amount to an average value that is different than that prescribed by the radiative transfer calculation, a proportional correction is applied to the rotational energy of each molecule.

3.5.6. A Simplified Approach to Rotational Cooling

This section discusses a simplified approach to radiative heat transfer adopted for the simulations discussed in Chapter 4 in lieu of the more detailed treatment described in Sections 3.5.1 to 3.5.5. The key simplifying assumption is that the transient atmosphere is transparent to infrared radiation, such that there is no trapping of spontaneously emitted energy or attenuation of solar energy. Radiative heating of the vapor by the lunar surface was also neglected. Thus, in Chapter 4, rotational cooling is modeled by adopting an approach similar to that of Combi (1996), using the H_2O radiative cooling rate expression specified by Gombosi et al. (1986) based on the work of Crovisier (1984). Accordingly, in the optically thin limit, each simulated molecule loses rotational energy at a rate Q_{rad} (in W/molecule) given by:

$$Q_{rad} = (4.4 \times 10^{-29})T_{rot}^{3.35} \qquad \text{for } T_{rot} < 52\ \text{K} \qquad (3.26a)$$

$$Q_{rad} = (2.0 \times 10^{-27})T_{rot}^{2.47} \qquad \text{for } T_{rot} \geq 52\ \text{K} \qquad (3.26b)$$

where T_{rot} is the rotational temperature representative of the rotational energy of the molecule (e_{rot}), given by:

$$e_{rot} = \tfrac{3}{2}k_B T_{rot} \qquad (3.27)$$

As discussed previously, it should be noted that radiative cooling affects translational temperature only when molecules exchange rotational and translational energy through collisions. Rotational energy gain due to absorption of unattenuated solar infrared radiation is accounted for by subtracting 6.835 × 10^{-25} W/molecule from Q_{rad} as calculated through Eq. (3.26a) or (3.26b). This is a band-averaged value over the 10-500 μm range obtained using molecular absorption coefficients (at STP) from the HITRAN database and approximating the Sun as a black body at 5780 K. It should be noted that this simplified approach does not account for variation of the absorption coefficients with temperature and at the low pressures seen in the DSMC simulations, leading (in general) to an overestimation of rotational heating due to solar radiation. These issues are addressed in the more detailed photon Monte Carlo modeling, and the simplified approach is deemed acceptable as a first approximation.

3.5.7. Vibrational Cooling

Both the Monte Carlo radiative transfer model and the simplified approach described above have focused on the influence of radiation on the rotational energy of water molecules, since gas temperatures in the problem tend to be sufficiently low that vibrational modes are practically inactive. However, the simulations do account for vibrational cooling through spontaneous emission through the approach of Zhang (2004). In this approach, the probability that a molecule with its i^{th} vibrational mode (i = 1, 2, 3 for H_2O) excited to level n, transitions to level (n – 1) in a time interval Δt is given by:

$$p_{emit} = 1 - \exp(-r_{emit}\Delta t) \tag{3.28}$$

Considering only spontaneous emission (i.e. neglecting stimulated emission due to solar radiation), the parameter r_{emit} is given by $nA_{i,1\rightarrow 0}$, where $A_{i,1\rightarrow 0}$ is the Einstein A coefficient corresponding to the 1→0 transition of the i^{th} mode (assuming – after Penner, 1959 – that $A_{i,n\rightarrow n-1} = nA_{i,1\rightarrow 0}$).

Due to the rapid cooling of impact-generated vapor during expansion and the relatively high characteristic vibrational temperatures of water, molecules largely remain in the vibrational ground state, where the probability of excitation through absorption is at its lowest; should a molecule be excited to a higher state, the probability that it will spontaneously de-excite is several orders of magnitude greater than the probability that it will be excited further. This suggests that rotational heating/cooling has a more significant influence on the thermodynamics of the impact-generated atmosphere; therefore, the DSMC code does not presently account for coupling between solar mid-infrared radiation and vibrational energy H_2O molecules.

Chapter 4: Transport of Water in a Transient Impact-Generated Lunar Atmosphere[1]

4.1. CHAPTER OVERVIEW

In this chapter, I present results concerning the structure of an impact-generated atmosphere and the associated cold trap deposition patterns, and briefly explore how these characteristics may be influenced by impact parameters and multi-species interactions. The simulations discussed in this chapter used the hybrid SOVA-DSMC approach described in Chapter 3 (Section 3.2), including atmospheric self-shielding (Section 3.3) and a simplified treatment of radiative (rotational and vibrational) cooling (Sections 3.5.6 and 3.5.7). To facilitate the comparison of results to the previous work of Stewart et al. (2011), the rough surface temperature model presented in Section 3.4 was not used; instead, lunar surface temperature was modeled as in Stewart (2010). Chapters 5 and 6 address surface roughness and radiative transfer in more detail.

Section 4.2 discusses the short-term evolution of the impact-generated atmosphere (from seconds to hours after impact), and how the collisional nature of the atmosphere affects volatile transport. Section 4.3 focuses on the patterns that arise as water accumulates on the cold lunar night-side surface and in the modeled cold traps. Section 4.4 briefly explores how impact parameters may affect post-impact gas dynamics, and

---

[1] Parts of Chapter 4 have previously been published as part of Prem, P., Artemieva, N. A., Goldstein, D. B., Varghese, P. L. & Trafton, L. M., 'Transport of water in a transient impact-generated lunar atmosphere', *Icarus* (2015). P.P. (the author of this dissertation) performed the DSMC simulations described in that work, and drafted the manuscript. N.A.A. was responsible for the SOVA simulations. D.B.G., P.L.V. and L.M.T. provided useful ideas, suggestions and feedback, and proofread the manuscript.

Section 4.5 discusses potential consequences of multi-species interactions in a collisional atmosphere. Section 4.6 summarizes key results and outstanding questions.

4.2. EVOLUTION AND STRUCTURE OF AN IMPACT-GENERATED ATMOSPHERE

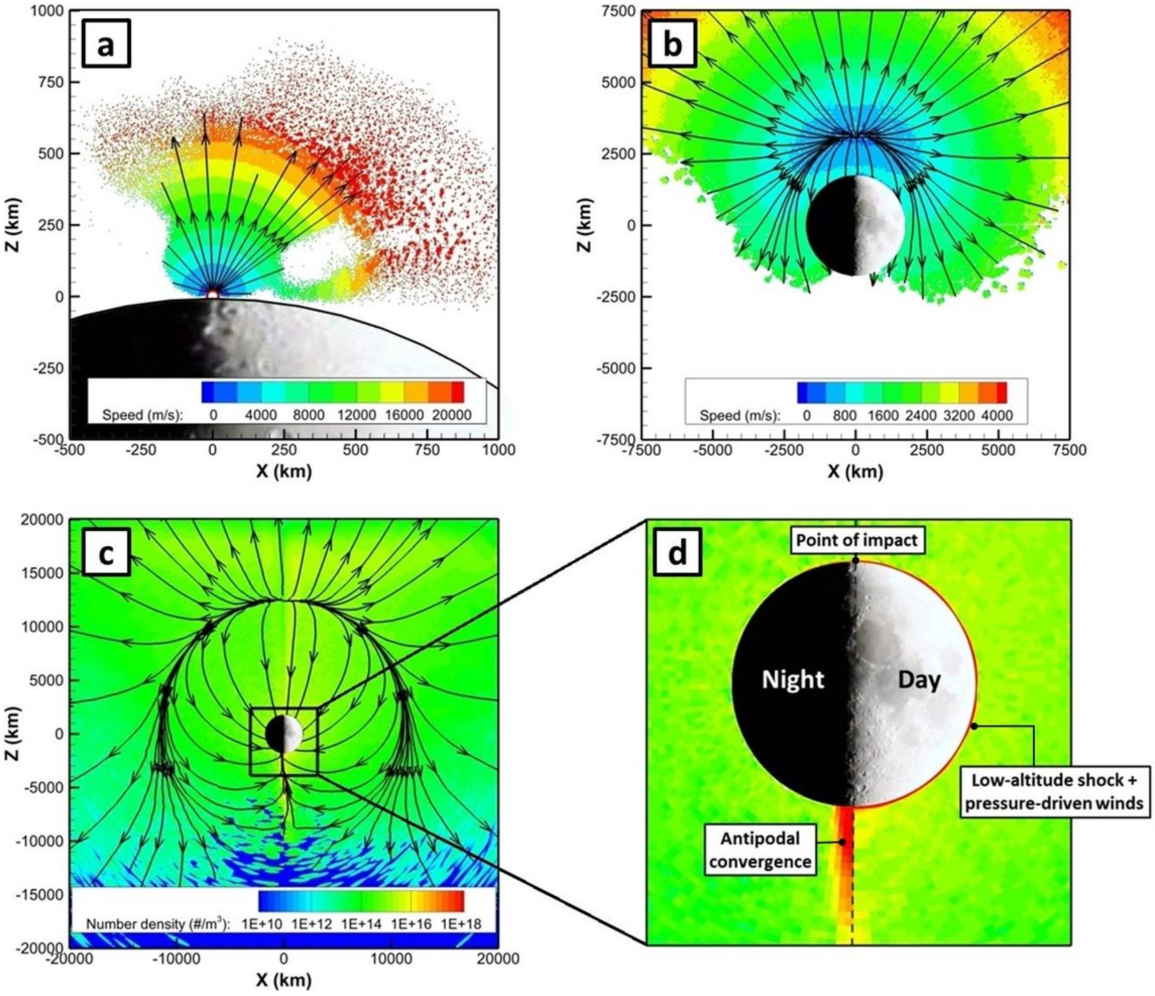

Figure 4.1: Cross-sectional views of the transient atmosphere in the plane of impact, at (a) 30 s; (b) 40 min; (c) and (d) 6 hours after impact. The image of the lunar surface is included only for perspective – although the simulations do account for diurnal variations in lunar surface temperature, actual topography is not modeled. Colors indicate speed (m/s) in (a) and (b), and number density (molecules/m^3) in (c) and (d). Streamlines, indicating flow direction, are superimposed in (a) to (c). Note the differences in color-scale between (a) and (b), and the different spatial extents of all four views.

The initial evolution of the post-impact atmosphere is characterized by the rapid, radially outward expansion of impact-generated water vapor away from the point of impact. Figure 4.1 shows cross-sectional views (in the plane of impact) of the transient atmosphere at seconds, minutes and hours after a 30 km/s, 60° impact. Due to the oblique nature of the impact, the initial vapor plume seen in Figure 4.1(a) is asymmetric, with most of the vaporized projectile material expanding downrange of the direction of impact. At this initial stage, a large part of the vapor plume travels at speeds far greater than lunar escape velocity (2.38 km/s at the surface) and is not gravitationally bound. However, vapor emerging at later times travels at progressively lower speeds, as apparent from the nested shells of constant speed in Figure 4.1(a). Within an hour after impact, slower-moving, gravitationally bound vapor begins to fall back to the lunar surface, as seen in Figure 4.1(b). Thereafter, the transient atmosphere maintains the characteristic structure depicted in Figure 4.1(c) for around 48 hours, until all gravitationally bound vapor has begun to fall back or has crossed the Moon's Hill sphere (~60,000 km in radius). It should be noted that the simulations track water vapor only out to 50,000 km from the lunar surface, thereby neglecting the small fraction of vapor that begins to fall back only beyond this distance, or goes into orbit around the Earth.

It can be seen from the velocity field shown in Figure 4.1(c) that several hours after impact, high-altitude streamlines form a near-spherical, slightly off-centered envelope around the Moon; vapor within this envelope falls back to the lunar surface, while vapor outside continues to expand away. Since vapor that is faster to begin with travels further and takes longer before it starts to fall back, the fallback envelope becomes progressively larger with time. The growth of the fallback envelope can be approximated analytically by considering the evolution of nested shells of constant velocity (as seen in Figure 4.1(a)) under variable gravity, treating each shell as though it is made up of non-interacting tracer particles, governed by the following equations of motion:

$$dv_r/dt = -\,GM/r^2 \qquad v_r = dr/dt \tag{4.1a}$$

$$dv_\theta/dt = 0 \qquad v_\theta = r d\theta/dt \tag{4.1b}$$

where r is radial distance (from the center of the Moon), θ is the polar angle, v_r and v_θ are velocities in the r and θ directions respectively, t is time, G is the gravitational constant and M is the mass of the Moon. When $v_r = 0$, a tracer particle begins to fall back, marking the boundary of the fallback envelope at that time.

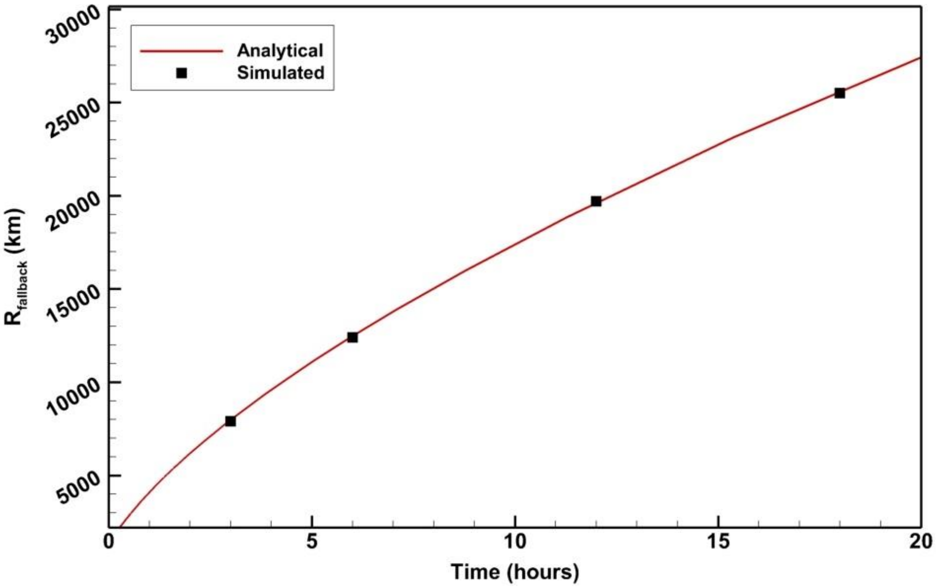

Figure 4.2: Comparison of simulated and analytically calculated values of $R_{fallback}$ as a function of time after impact. $R_{fallback}$ is a representative measure of the size of the fallback envelope, defined as the radial distance from the center of the Moon to the fallback envelope, measured through the point of impact.

This analytical treatment is possible because, although the vapor is collisional, the high velocities and low temperatures reached during the expansion into vacuum mean that at high altitudes, molecular trajectories are close to ballistic. Therefore, although non-interacting tracer particles cannot capture gas dynamic interactions such as those which occur antipodal to the point of impact, Eq. (4.1) can be used to estimate the size of the fallback envelope at a given time with reasonable accuracy. Figure 4.2 demonstrates the close agreement between simulated and analytically derived values of a representative dimension, $R_{fallback}$ (the radial distance from the center of the Moon to the boundary of the fallback envelope, measured through the point of impact), calculated by setting $v_\theta = 0$ (for a tracer particle moving radially outward) and using Eq. (4.1a) to compute the radial distance at which $v_r = 0$ as a function of time after impact. For the specific impact simulated here, we find from the hydrocode results that the radial velocity at a point 20 km above the lunar surface can be approximated by $v_r = 1000 + 9800e^{-0.169(31-t)}$ for times $t = 11$ to 30 s after impact. Based on this expression for v_r, the fallback envelope reaches the Hill sphere (i.e. $R_{fallback} = 60{,}000$ km) at ~65 hours after impact.

As the expanding vapor cloud grows to completely surround the Moon, the streamlines that delineate the fallback envelope reconverge, approximately antipodal to the point of impact. Since the expansion flow is supersonic, this reconvergence leads to the formation of a columnar shock that compresses and channels the vapor down towards the lunar surface. For the North Polar impact shown in Figure 4.1, antipodal reconvergence occurs above the lunar South Pole, as seen in Figure 4.1(c). Despite the asymmetry of the initial vapor plume, it is seen that fallback and antipodal reconvergence occur in a near-symmetric manner, since the slower, late-emerging vapor, which remains gravitationally bound to the Moon, tends to be less strongly downrange-focused than the early, high-velocity component. An antipodal shock should form after any sufficiently large-scale release of volatiles, leading to preferential redistribution of water in the vicinity of the antipode (at least in the short term). In the simulations presented here, the impact location is such that the antipodal shock intersects the cold night-side; if instead, the antipode happened to be located on the day-side, the antipodal shock would still drive a concentrated jet of water vapor down towards the surface, but interaction of this jet with day-side winds could lead to more complex deposition patterns. Interestingly, antipodal effects related to impacts have previously been explored in other, different contexts; e.g. Hood and Artemieva (2008) investigate the role of antipodal reconvergence in the origin of magnetic anomalies antipodal to large lunar impact basins. It should be noted that the shock results from the collisional nature of the atmosphere. If the atmosphere were collisionless, molecules would simply stream past each other as the expanding flow reconverged; the abrupt turning and compression of water vapor across a shock would be absent, and there would be no preferential redistribution around the antipode.

The collisional nature of the transient atmosphere also gives rise to a stratified atmospheric structure over the day-side hemisphere. This structure is absent over the night-side hemisphere, since the cold night-side surface acts as a temporary cold trap – the average modeled night-side surface residence time for a water molecule is ~37 hours, so molecules that fall back to the night-side remain largely immobile until sunrise, whereas molecules falling back to the warm day-side have much shorter residence times

(~0.1 µs at the sub-solar point) and largely remain aloft. When cold, rarefied, supersonic vapor falling back from higher altitudes encounters vapor lofted by the warm day-side surface, a low-altitude shock forms over the day-side hemisphere.

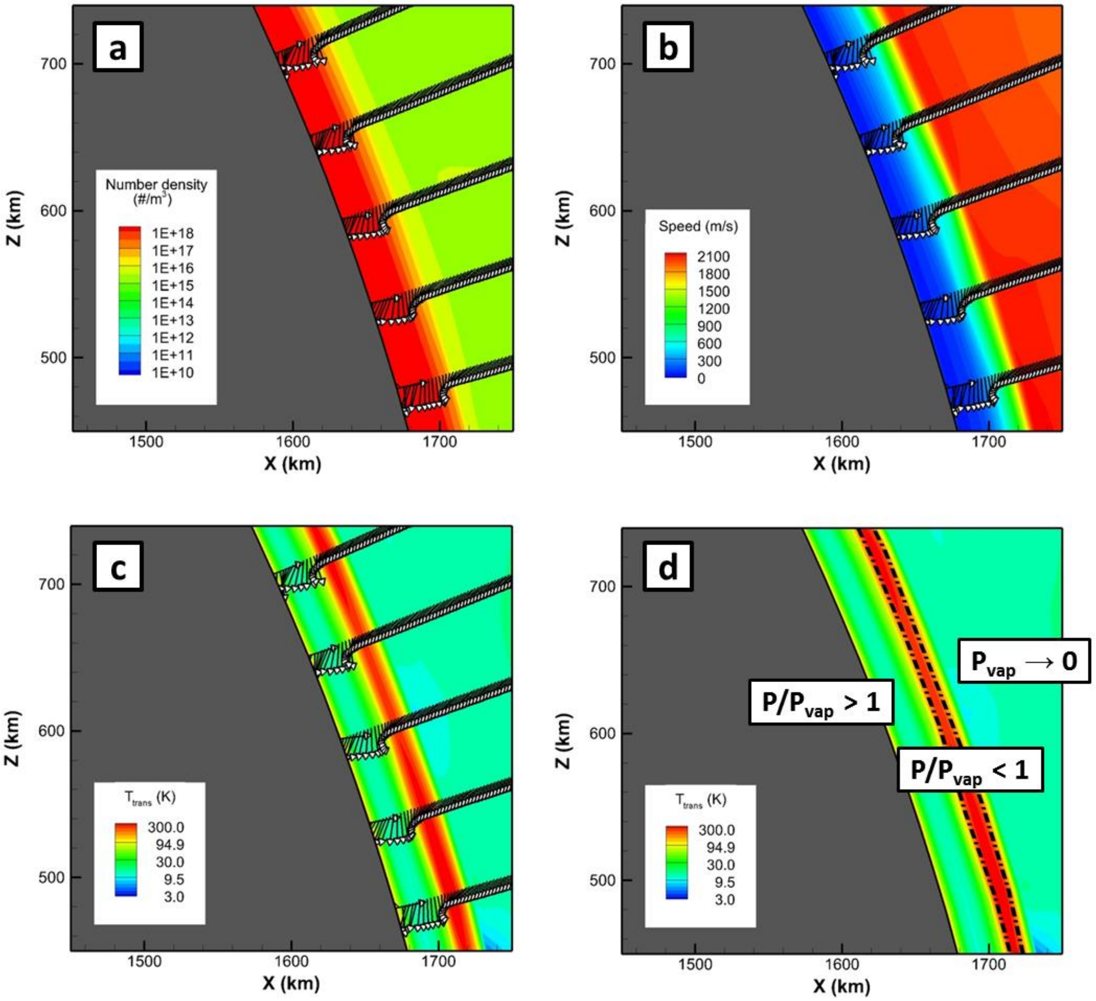

Figure 4.3: Cross-sectional views (in the plane of impact) of the low-altitude shock that forms over the lunar day-side, shown at 6 hours after impact. The x- and z- axes indicate distance (km) from the center of the Moon. Contours of (a) number density (molecules/m^3); (b) speed (m/s); and (c), (d) translational temperature (K) show the compression, deceleration and heating of water vapor across the shock. The arrows in (a) to (c) indicate the direction of the flow. The dotted lines in (d) mark the boundary of the region within which the ratio of kinetic pressure, p, to the saturation vapor pressure, p_{sat} is less than 1. Vapor is supersaturated (i.e. $p/p_{sat} > 1$) above and below this region.

Figure 4.3 depicts the structure of the day-side atmosphere in more detail. As the infalling vapor passes through the shock, the flow decelerates and turns to travel parallel to the surface. The vapor is also compressed and heated. (Note that due to the relatively low number of simulated molecules in the low density pre-shock region, there is some noise in the DSMC solution, which is most visible in the temperature contours.) Below the shock, the flow is driven by global pressure gradients and the pre-shock momentum of the infalling vapor, giving rise to winds that travel from the day-side to the night-side and away from the point of impact. These winds transport vapor from the day-side to the night-side, leading to the temporary accumulation of water ‘frost’ (adsorbate) on the cold night-side surface. These results serve to illustrate that volatile transport in a transient atmosphere, characterized by shocks and pressure-driven winds, is qualitatively very different from typical exospheric transport through collisionless, ballistic hops. The directional, pressure-driven flow of water to cold traps and to the shelter of the night-side after an impact is a more efficient transport mechanism than the random walk that occurs in the collisionless limit. (In the latter case, migrating molecules are as likely to move towards the day side as to night side.)

Another notable feature is the thermal structure of the transient atmosphere (Figures 4.3(c) and (d)). With the simplified radiative cooling model used in this chapter, cold infalling vapor is heated as it passes through the shock, but subsequently cools through radiation. Since we assume complete thermal accommodation of molecules that interact with the lunar surface, there is also a thin, warm layer adjacent to the surface. Sandwiched between the layers of vapor heated by the shock and the day-side surface is a cold, intermediate-altitude layer. The presence of this cold, relatively dense layer raises the question of whether condensation of water could occur in an impact-generated atmosphere. From Fleagle and Businger (1980), the saturation vapor pressure of water vapor over ice is given by:

$$p_{sat} = (3.27 \times 10^{12})\exp(-6119/T_{tr}) \tag{4.2}$$

where T_{tr} is translational temperature. This can be compared to the kinetic pressure of the vapor, given by the ideal gas law:

$$p = nk_B T_{tr} \tag{4.3}$$

where n is number density. If $p/p_{sat} > 1$, the vapor is super-saturated and could condense in the presence of condensation nuclei (e.g. lunar or cometary dust). Condensation is not modeled here, but it can be seen from Figure 4.3(d) that the vapor is super-saturated above and below the shock-heated layer. Although $p_{sat} \rightarrow 0$ above the shock-heated layer, the low gas density in this region makes condensation unlikely (since molecular collision rates are very low). The cold, dense, super-saturated layer below the shock-heated layer provides conditions more favorable for condensation; condensation in this layer could create a day-side mist or lead to the precipitation of ice crystals or water droplets. However, it is important to note that saturation vapor pressure is strongly dependent on gas temperature, which is underestimated here due to the simplified treatment of radiative cooling – detailed investigation of potential phase changes would require a more accurate treatment of radiative heat transfer (as in Chapter 6) as well as a condensation model.

The transient atmosphere maintains the general structure discussed above until most of the remaining gravitationally bound vapor has fallen back to low altitudes. As fallback diminishes, the surface and antipodal shocks dissipate, but the atmosphere remains collisional, with higher densities over the day-side and around the antipode. As observed in the simulations of Stewart et al. (2011), only several lunar days after impact does the atmosphere become largely collisionless, although the sublimation of night-side frost at sunrise continues to sustain localized collisional transport across the dawn terminator for some time. Ultimately, all of the gravitationally bound water is either photodestroyed or cold-trapped.

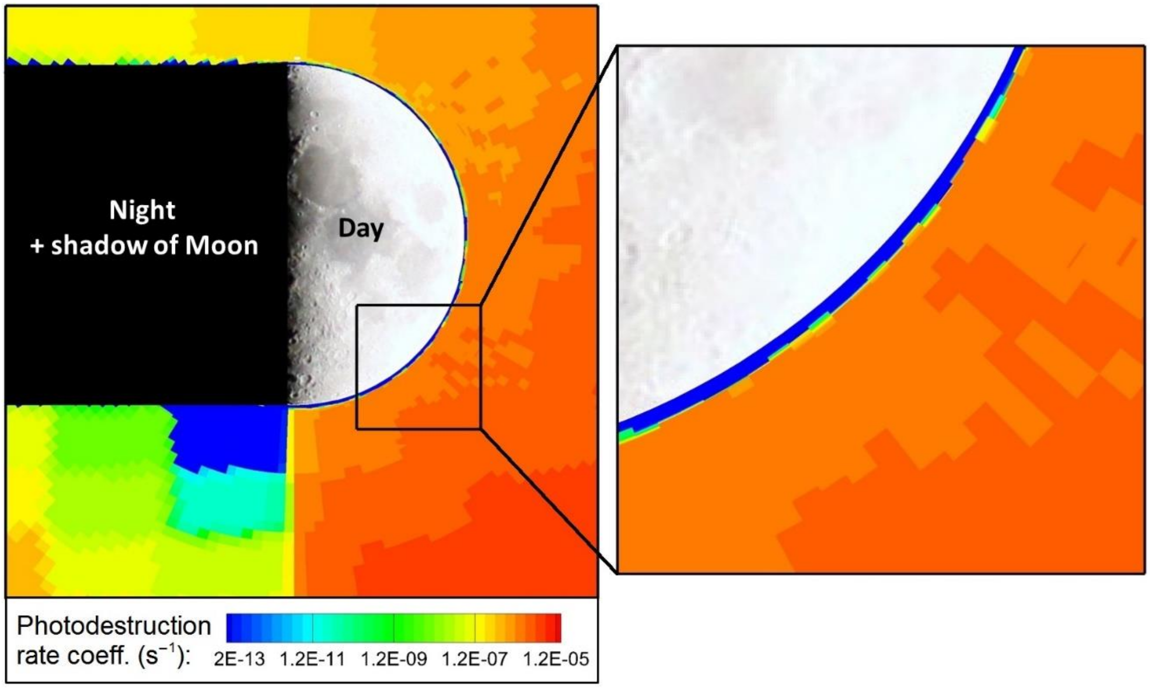

Figure 4.4: Local photodestruction rate coefficients (s^{-1}) in a plane-of-impact cross-section of the water vapor atmosphere, 6 hours after impact, showing reduced rates of photodestruction over the day-side and behind the antipodal shock. The atmosphere is illuminated by sunlight coming from right to left.

In an optically thick atmosphere, partial shielding from photodestruction may extend the lifetime of molecules, allowing more water to reach the cold traps. Since the lifetime of a water molecule in unattenuated sunlight at 1 AU is ~24 hours (Huebner et al., 1992), self-shielding does not have a visible effect on the structure of the transient atmosphere over the timescales shown in Figure 4.1. However, the structure of the transient atmosphere does have a significant influence on the rate of atmospheric loss, as illustrated by Figure 4.4. It can be seen that several hours after an impact, there is negligible photodestruction in the dense, post-shock day-side atmosphere, as well as immediately behind the dense antipodal shock. Due to the relatively coarse Cartesian grid used for calculations of column density (see Section 3.3), there is some "blockiness" in the rate coefficient contours, but selective refinement of the grid in the vicinity of the lunar surface, where the major density jumps take place, allows us to resolve the resulting drops in the intensity of sunlight (and thereby, photodestruction rate) across the day-side and antipodal shocks. (Note that the apparent truncation of the shadow cast by the antipodal shock is a computational artefact – because the DSMC grid is spherical, computational cells become larger further away from the N-S axis; the antipodal shock thus blocks only part of the sunlight entering the relatively large cells behind it, so that these cells have a higher total photodestruction rate than smaller cells closer to the axis that are completely shielded by the antipodal shock.) Over the first 120 hours after impact, the overall reduced photodestruction rate due to atmospheric self-shielding leads to the cold-trapping of approximately five times as much water as when the atmosphere is treated as transparent to ultraviolet radiation (i.e. when self-shielding is neglected).

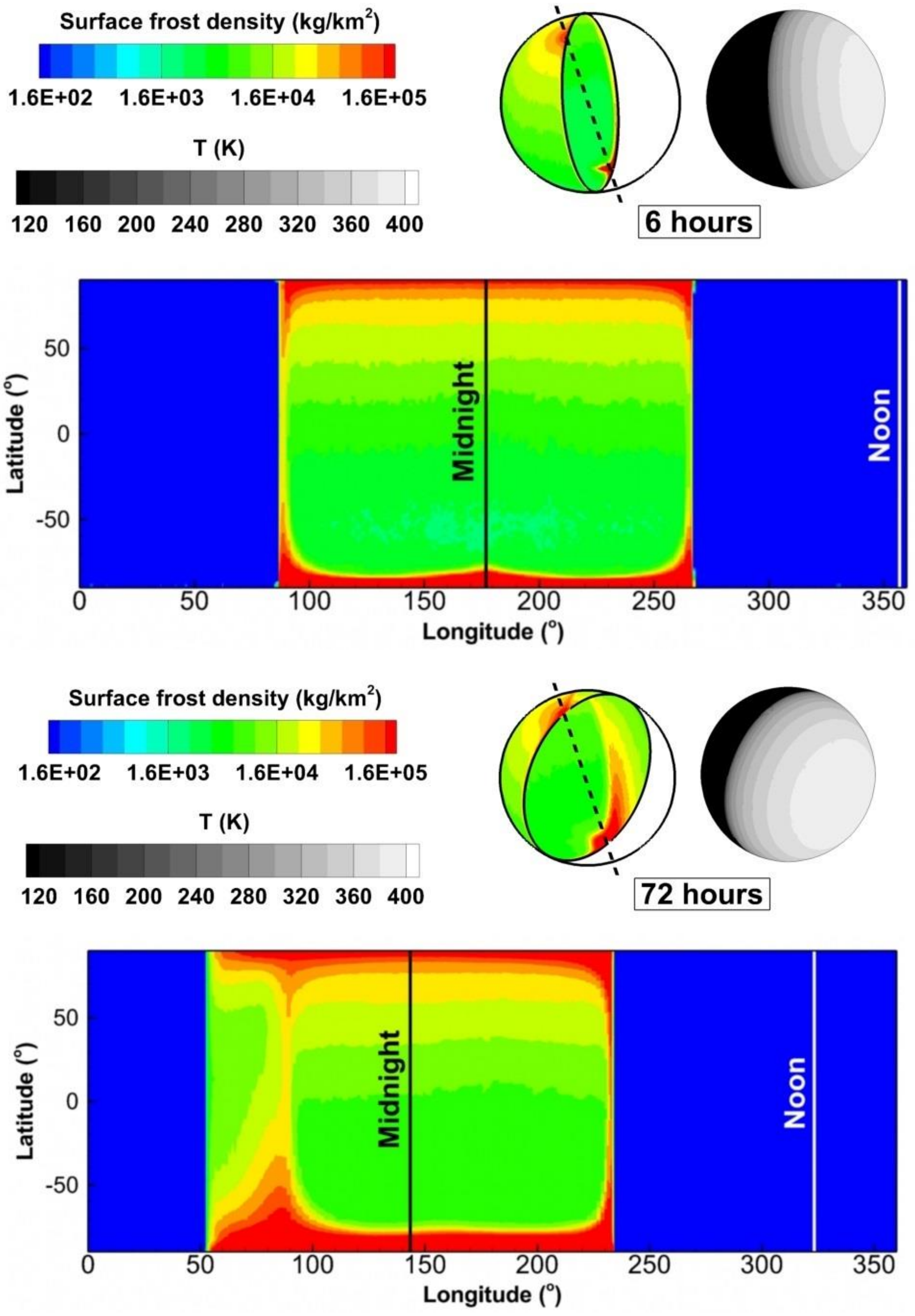

Figure 4.5: Cylindrical projections of the lunar surface, showing surface frost patterns at 6 hours (top) and 72 hours (bottom) after impact. The inset images show cut-away views of the lunar night side (color) and surface temperature (grayscale). Due to the warm day-side temperatures, the blue regions in the cylindrical projections have very little frost.

4.3. EVOLUTION OF NIGHT-SIDE FROST AND COLD TRAP DEPOSITION PATTERNS

Besides atmospheric structure, the distribution and temporal evolution of night-side ‘frost’ (adsorbed water molecules) offers some insights into the post-impact volatile transport process. Figure 4.5 shows snapshots of global surface density (in kg/km^2) of water frost at 6 hours and 72 hours after impact. Concentrated deposits are seen around the North Polar point of impact and the South Polar antipode. At the times shown, the thickest night-side deposits are O(10^5) kg/km^2. Following the approach of Hodges (2002), a monolayer of water is equivalent to ~0.3 kg/km^2 (or 176 ppm). By this measure, the entire lunar night-side has substantially more than a monolayer coating of water. A few monolayers of water may also form on the day side, since at typical post-shock pressures over the day-side hemisphere, the monolayer formation time (O’Hanlon, 2003) is less than a second. However, any subsequent accumulation of water would be hindered by low surface residence times at day-side surface temperatures.

Figure 4.5 also shows longitudinal banding of the night-side frost deposits near the dawn and dusk terminators. The band of frost at the dawn terminator is continuously replenished as water that desorbs at dawn is pushed back across the terminator by day-side winds. This enhancement in density at the dawn terminator persists even in the collisionless limit. Meanwhile, the band of frost deposited along the original dusk terminator reflects the diminishing intensity of fallback from altitude with time, and is preserved for only half a lunation.

Figure 4.6 tracks the amount of water deposited at the North and South Polar cold traps over the course of the first 120 hours after impact, as well as the amount that is lost (i.e. either photodestroyed or crosses the computational domain boundary at 50,000 km from the lunar surface). Interestingly, Figure 4.6 indicates that for an impact at the North Pole, antipodal effects lead to cold-trap deposits at the South Pole that are not only more massive (as anticipated, due to the greater cold-trapping area available at the South Pole), but also more concentrated. It is found that 120 hours after a 60°, 30 km/s impact, the North and South Polar cold traps have accumulated an amount of water equivalent to ice cover O(1 mm) thick over a total area of 5831 km^2 (1257 km^2 at the North Pole and 4574 km^2 at the South Pole). It should be noted that deposition in cold traps continues for several lunar days beyond the time interval shown in Figure 4.6 (Stewart et al., 2011).

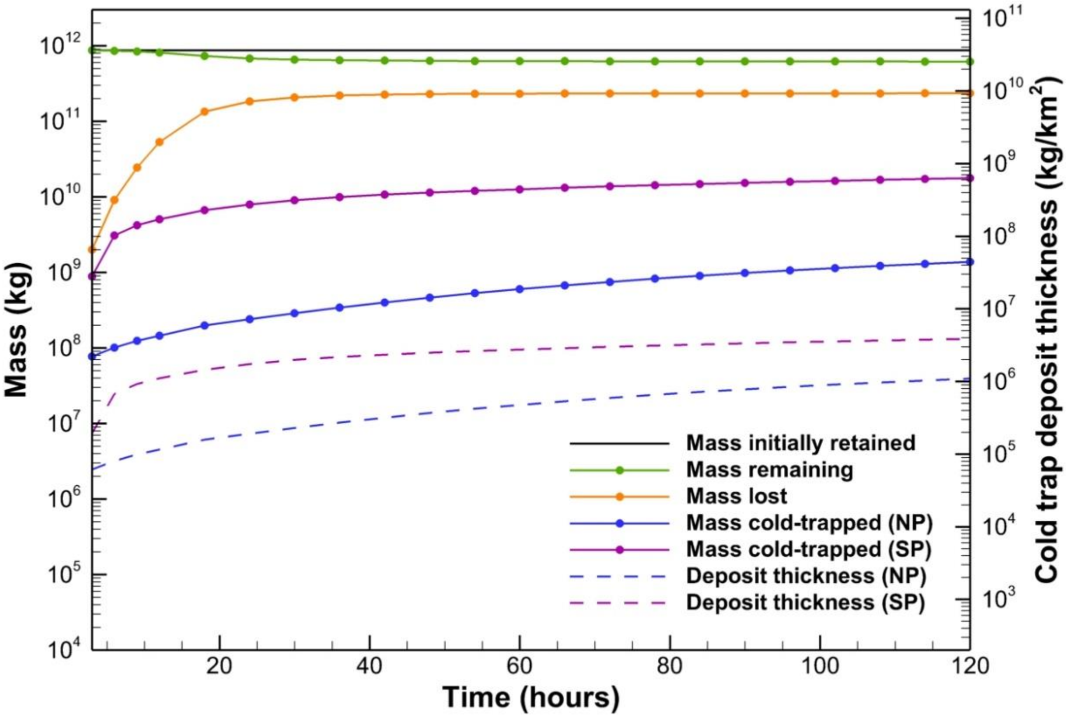

Figure 4.6: The amount of water that is lost (i.e. photodestroyed or crosses the computational domain boundary) and cold-trapped over the first 120 hours after impact. Also shown are the amount of water initially retained (gravitationally bound) and the amount remaining (aloft or as transient night-side frost).

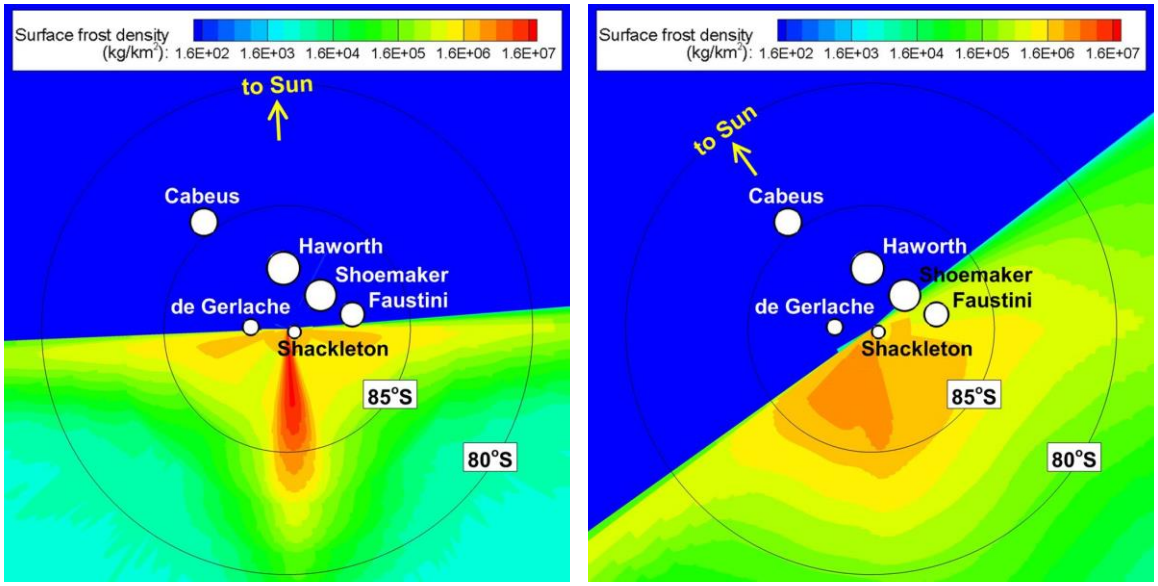

Figure 4.7: The simulated South Polar cold traps overlaid on frost density maps, 6 hours and 72 hours after impact. Cold trap boundaries do not precisely mark the location of actual regions of permanent shadow, but are representative in size.

Cold trap	**Area (km^2)**	**6 hours**		**72 hours**	
		Water captured (kg/km^2)	*Relative magnitude*	*Water captured (kg/km^2)*	*Relative magnitude*
Cabeus	897	4.65×10^5	**1.00**	2.80×10^6	1.17
Faustini	697	6.09×10^5	1.31	2.86×10^6	1.20
de Gerlache	314	8.31×10^5	1.79	3.85×10^6	1.61
Haworth	1295	5.75×10^5	1.24	3.01×10^6	1.26
Shackleton	201	2.20×10^6	**4.73**	6.49×10^6	**2.72**
Shoemaker	1170	6.84×10^5	1.47	2.39×10^6	**1.00**

Table 4.1: Comparison of amounts of water captured by the modeled South Polar cold traps at 6 hours and 72 hours after impact. The lowest and highest concentrations at both times are highlighted. Note that 10^5 kg/km^2 corresponds to an ice thickness of ~ 0.1 mm.

A question of particular interest is whether the collisional and markedly non-uniform structure of the transient atmosphere can lead to non-uniform deposition of water at cold traps. Figure 4.5 indicates that there are non-uniformities in night-side frost cover even at 72 hours after impact, when the antipodal shock has dissipated. Table 4.1 compares the amount of water captured by the six modeled South Polar cold traps, while Figure 4.7 situates these cold traps in the context of transient frost cover. It is observed that Shackleton crater, which happens to coincide with the antipode for the chosen location of impact, maintains the highest concentration of water, consistent with its location where the surface footprint of the antipodal shock is strongest. At 6 hours after impact, the cold trap deposit at Shackleton is almost five times as concentrated as the least concentrated deposit, at nearby Cabeus. However, by 72 hours after impact – after the antipodal shock has vanished and some slow migration of night side frost has taken place – the initial contrast between the different cold traps has reduced.

Although it is interesting to note that the collisional nature of the impact-generated atmosphere can create non-uniform cold trap deposition patterns, longer-term simulations are required to ascertain to what degree initial non-uniformities are preserved as the atmosphere transitions to the collisionless limit and deposition becomes more uniform. It should also be noted that a different impact location could lead to more or less heterogeneous distribution of water between cold traps. Additionally, we do not model topography and thermal conditions within individual cold traps, which could further affect the heterogeneity of deposition patterns.

4.4. A BRIEF EXPLORATION OF IMPACT PARAMETERS

The simulation results discussed above are for a specific set of impact parameters. The modeled impact velocity and impactor size are representative of Jupiter-family comets, which have mean encounter velocities of ~20 km/s and estimated radii O(1 km) (Weissman, 2006), but generalizing these results requires a broader understanding of how these and other parameters affect post-impact volatile transport. In this section, I briefly discuss how impact parameters influence the results presented in preceding sections.

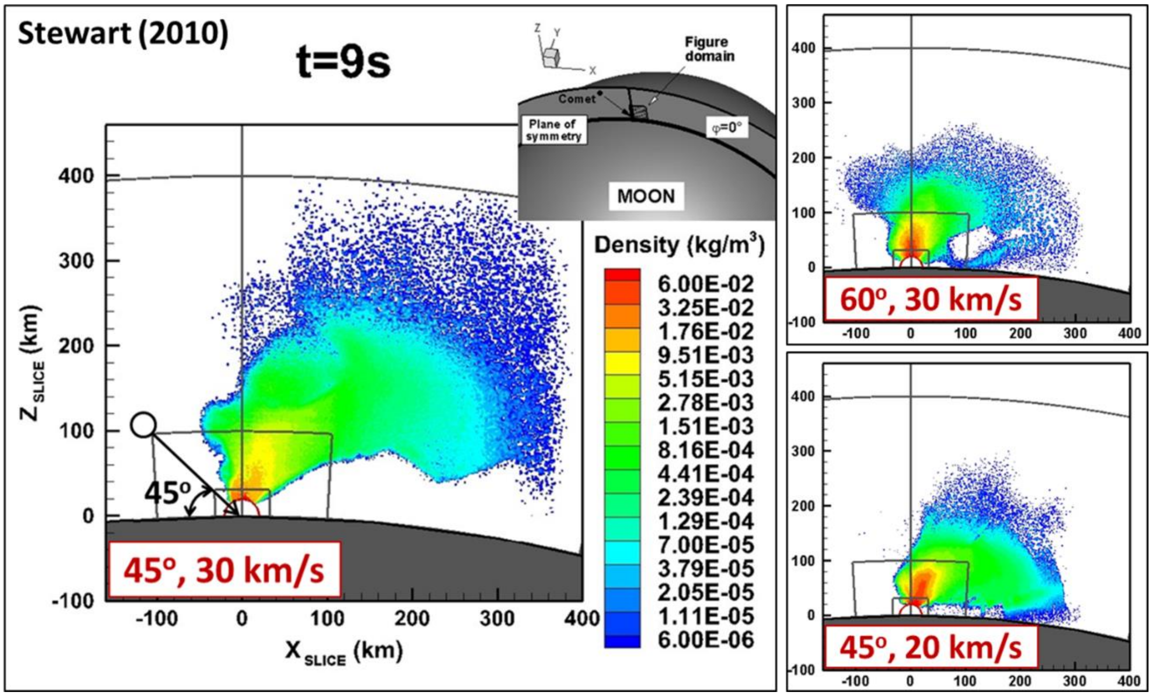

Figure 4.8: Mass density contours in the plane of impact at 9 s after impact, for the 45°, 30 km/s impact simulated by Stewart (2010) compared to a 60°, 30 km/s case (different impact angle) and a 45°, 20 km/s case (different impact velocity).

Figure 4.8 compares the vapor plumes generated by three different impacts; the 45°, 30 km/s impact modeled by Stewart et al. (2011) is treated as a baseline case, shown alongside the 60°, 30 km/s case discussed above, as well as a 45°, 20 km/s case. Comparing the 45° and 60° cases, it can be seen that the more oblique impact results in more pronounced downrange focusing of the vapor plume; when the impact is closer to vertical, the initial plume is more symmetric. This is consistent with hydrocode modeling carried out by Pierazzo and Melosh (2000). More significant from the perspective of volatile retention is the finding that the more oblique impact partitions more energy into the projectile (also observed by Gisler et al., 2006 and Pierazzo and Melosh, 2000 in their modeling), resulting in a lower fraction of vaporized projectile material remaining gravitationally bound. All other impact parameters being the same, ~28% of the comet mass remains gravitationally bound in the 60° case, compared to ~3% in the 45° case.

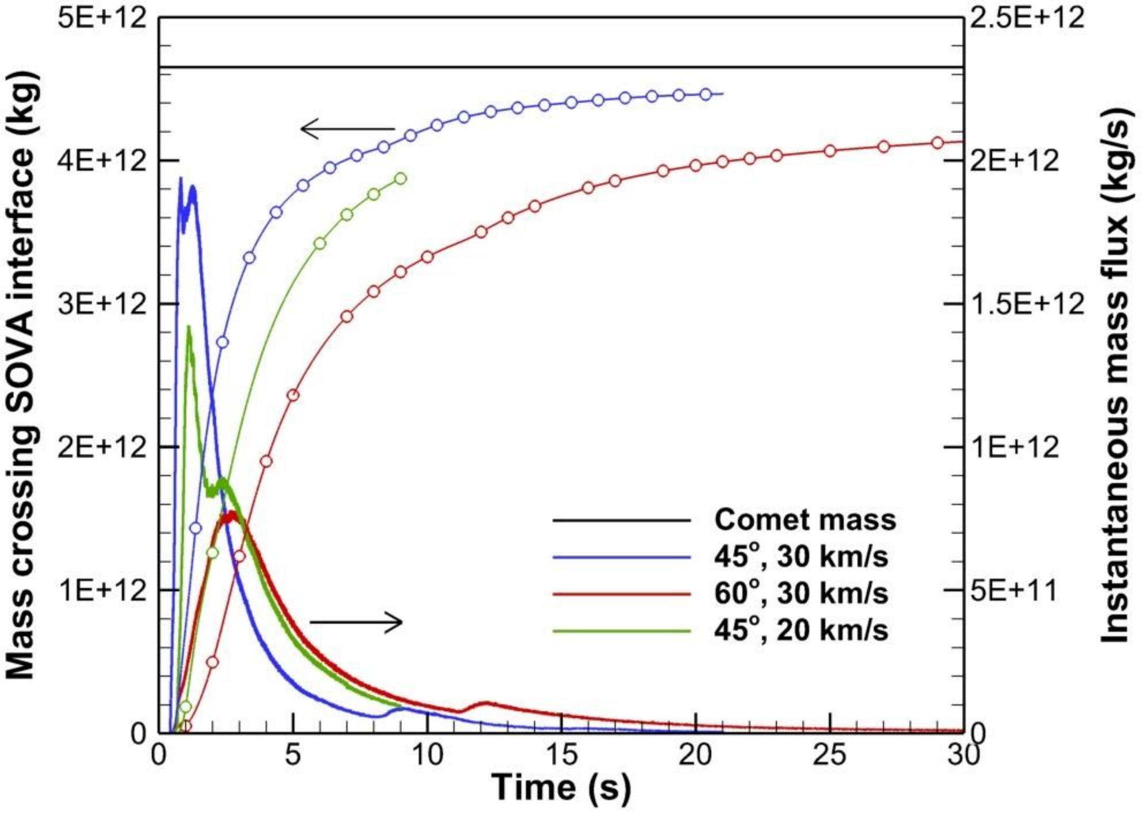

Figure 4.9: Total mass and instantaneous mass flux across the SOVA interface (20 km from the point of impact) as a function of time, for the three different impact scenarios shown in Figure 4.8. Due to computational constraints, the 45°, 20 km/s run was paused at a point where there was still significant mass flux across the interface.

Figure 4.9 shows the total mass and mass flux across the SOVA interface into the DSMC domain for the three different impact scenarios modeled. In all three cases, most of the material that crosses the interface during the initial ~10 s after impact travels faster than the escape velocity. Thus, from Figure 4.9, it appears that the amount of vapor remaining gravitationally bound in the 45°, 20 km/s case would be higher than in the 45°, 30 km/s case (as expected, due to the lower initial kinetic energy) and lower than in the 60°, 30 km/s case. (Due to computational constraints, the 45°, 20 km/s case could not be run to completion.) Considering a broader range of impact velocities, Ong et al. (2010) conclude that low velocity impacts play a dominant role in the delivery of lunar water, since more vapor remains gravitationally bound after low velocity impacts. Similarly, the preliminary investigations into the influence of impact angle presented here suggest that less-oblique impacts may have made a more significant contribution to the lunar volatile inventory, although the most probable impact angle is 45° (Pierazzo and Melosh, 2000). This suggests that better quantification of how much material comets may have delivered to the Moon (an important question, though not the focus of this work) requires a broader exploration of parameter space, taking into account the influence of impact angle as well as velocity.

Since the transient atmosphere is composed of the fraction of impact-generated vapor that remains gravitationally bound, parameters that determine this fraction – such as impact velocity, angle and material properties of the target and impactor – determine whether or not a transient, collisional atmosphere forms, as well as the longevity of this atmosphere. The amount of material present in the atmosphere also determines the degree of self-shielding from photodestruction, and the strength of the shock structures discussed in Section 4.2 – thereby determining the velocity of the day-side winds and the shape and size of the surface footprint of the antipodal shock, which in turn affect the rate of volatile transport and the nature of deposition patterns.

Another variable parameter is impact location. Since it is difficult to conclusively identify particular lunar craters as having been created by comet impacts, and since any latitudinal variation in impactor flux is likely to be small (Le Feuvre and Wieczorek, 2008), the decision to simulate an impact at the North Pole was motivated chiefly by considerations of computational cost. As mentioned in Section 4.2, a key consequence of the chosen impact location is that the antipodal shock directly intersects the cold night-side; had the impact location (latitude and time) been such that the antipode was situated on the day-side, interaction of the antipodal shock with the low-altitude day-side shock could have led to more complex post-shock winds and different deposition patterns – a possibility that deserves further investigation.

4.5. PHOTOCHEMISTRY AND OTHER MULTI-SPECIES INTERACTIONS

The simulations presented here model a comet as composed solely of H_2O ice and consider only the behavior of water vapor – neglecting photodissociation products, as well as any reactions between them. In reality, a comet impact may release multiple gaseous species, and *in a collisional atmosphere*, these species and their dissociation products may participate in further reactions. Although such chemistry is not modeled in detail in this work, the simulation results discussed in preceding sections give rise to several interesting questions regarding the role of multiple gaseous species in an impact-generated atmosphere.

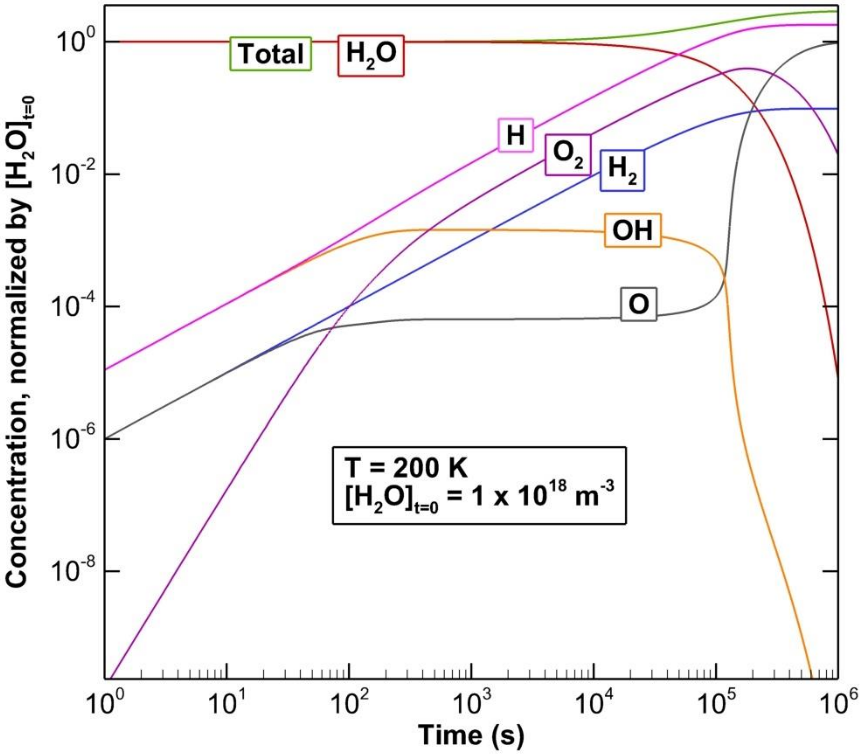

Figure 4.10: The evolution over time of the composition of a nominal water vapor atmosphere (homogeneous and held at constant temperature) as a result of the reactions summarized in Table 4.2. The graph shows the concentrations of various species and the total number density, relative to the initial concentration of H_2O.

To gauge how the composition of the impact-generated atmosphere might change if photochemistry and chemical reactions were accounted for, I used an approach similar to Berezhnoy et al. (2003) to model the change in composition over time of a homogeneous, constant temperature 'atmosphere' initially composed of water vapor, due to photodissociation and chemical reactions between dissociation products. The model included six likely photodissociation and neutral-neutral reactions, selected from Huebner et al. (1992) and Cochran (1982), with dissociation rate constants from Huebner et al. (1992) and Crovisier (1989), and equilibrium rate constants from Giguere and Huebner (1978) and Tsang and Hampson (1986). This reaction and rate information is summarized in Table 4.2. The resulting change in the relative concentrations of the six modeled species over time is shown in Figure 4.10.

Reaction	**Rate coefficient [units]**	**Reference**
$H_2O + h\nu \rightarrow H + OH$	1.1×10^{-5} [s^{-1}]	[1]
$H_2O + h\nu \rightarrow H_2 + O$	0.1×10^{-5} [s^{-1}]	[1]
$OH + h\nu \rightarrow O + H$	7.5×10^{-6} [s^{-1}]	[2]
$OH + OH \rightarrow H_2O + O$	$(3.5 \times 10^{-16})T^{1.4}\exp(200/T)$ [$cm^3 molecule^{-1} s^{-1}$]	[3]
$OH + O \rightarrow H + O_2$	$(5 \times 10^{-11})(T/300)^{0.167}$ [$cm^3 molecule^{-1} s^{-1}$]	[4]
$O_2 + h\nu \rightarrow O + O$	4.2×10^{-6} [s^{-1}]	[2]

Table 4.2: Reaction and rate information used to create Figure 4.10. Rate coefficients were obtained from [1] Crovisier, 1989; [2] Huebner et al., 1992; [3] Tsang and Hampson, 1986; [4] Giguere and Huebner, 1978. Temperature $T = 200$ K for Figure 4.10.

One notable result from this simple model is that over the lifetime of the transient atmosphere, species likely to be non-condensable at lunar night-side pressures and temperatures, such as O_2 (NIST Chemistry WebBook), could accumulate as a result of chemical reactions between photodissociation products. This may influence the cold-trapping process, since the presence of less condensable species can slow the rate of condensation of a species that condenses more readily, such as water (a possibility noted by Arnold (1979) in their discussion of the effects of a temporary lunar atmosphere, and has also been demonstrated by Moore et al. (2009) in the context of atmospheric collapse on Jupiter’s moon Io). The presence of non-condensable species may also strengthen the atmospheric self-shielding effect and sustain pressure-driven winds for a longer period of time after impact. This in turn may lead to increased cold-trapping of species with relatively short photo-lifetimes, which may not be expected to survive long enough to migrate to the shelter of a cold trap if the atmosphere is transparent and migration occurs through diffusive, collisionless hopping.

It should be noted that Figure 4.10 does not represent the full complexity of chemistry in an impact-generated atmosphere – for instance, the simplified model does not account for the removal of species from the atmosphere through condensation or thermal/hydrodynamic escape, for spatial and temporal variations in the structure of an impact-generated atmosphere, or for non-equilibrium reaction rates. Indeed, the discussion in this section primarily serves to illustrate that even a very simple chemical model, based on a very simple initial atmospheric composition, gives rise to a cocktail of multiple species which, combined with the collisional nature of the simulated impact-generated atmosphere, has several interesting potential consequences.

4.6. KEY RESULTS AND OUTSTANDING QUESTIONS

The simulations presented in this chapter were motivated by the finding that for representative impact parameters, a significant amount of cold trap capture occurs while the impact-generated atmosphere is collisional (Stewart et al., 2011) – in this context, linking current observations of potential water ice in lunar cold traps to ancient impacts calls for an understanding of how collisional gas dynamics influences volatile fallout.

We find that within hours after impact, the transient atmosphere acquires a characteristic structure, which it maintains until the fallback of vapor from high altitudes diminishes. Cold, rarefied vapor falling back (in a near-ballistic manner) to the day-side hemisphere is compressed and heated by a low-altitude shock; below this shock, volatile transport over the day-side hemisphere occurs through pressure-driven winds. Antipodal reconvergence of the expanding vapor cloud leads to the formation of a near-cylindrical ‘antipodal shock’, which may leave a perceptible footprint where it intersects the lunar surface, depending on the impact location. In the case modeled here, the day-side and antipodal shocks dissipate at around 48 hours after impact, but the day-side winds prevail as long as the atmosphere remains collisional, and high atmospheric density in the vicinity of the antipode also persists for some time.

The longevity of a transient atmosphere and the strength of the features identified above depend on various impact parameters, such as impact angle and velocity, which determine the fraction of vaporized cometary material that remains gravitationally bound i.e. the initial mass of the transient atmosphere. However, the characteristic structure and the nature of transport processes should be similar whenever an airless body holds a significant quantity of volatiles gravitationally bound after an impact.

It is also important to note that in a collisionally and optically thick atmosphere, certain physical processes such as shielding from photodestruction, chemical reactions and radiative heat transfer, which are negligible in a collisionless and typically optically thin) exosphere, become significant. The simulations presented in this chapter account for atmospheric self-shielding, which is found to increase the amount of water captured at polar cold traps. Water is the only species modeled in this work, but the results discussed here raise several interesting questions concerning the role of multiple species, which deserve further investigation. For instance, does the presence of other species (released during the impact process, or formed subsequently through chemical reactions) influence the cold-trapping of water, either by depleting or enhancing the concentration of water through chemical reactions, or by impeding condensation into cold traps? Also, do interactions between different species and the lunar surface result in preferential condensation of certain compounds, such that the composition of cold trap deposits may not mirror the composition of the impactor?

The fallout of volatiles after a comet impact is seen to be non-uniform, particularly in the vicinity of the antipode, suggesting that in principle, volatile-rich impacts could result in heterogeneous cold trapping, as indicated by remote sensing observations. However, it should be noted that late-term, collisionless transport may obscure the sharp non-uniformities seen in the short-term fallback patterns discussed in is chapter – longer simulation run-times are required to quantify the degree to which this may occur. Additionally, the role of an antipodal shock in creating non-uniform deposition patterns implies that different impact locations (both at different latitudes and different times of day) could result in more or less uniform cold-trap deposits.

The results presented in this chapter also provide a rationale for revisiting certain simplifying assumptions that were made. For instance, although the simulations accounted for the attenuation of ultraviolet radiation, the transient atmosphere was assumed to be transparent to infrared radiation, resulting in an overestimation of radiative cooling at most times. This simplification may affect the structure of the atmospheric shocks, which in turn influences the dynamics of day-side winds, and cold-trap deposition patterns. Radiative heat transfer may also affect the thermal structure of the atmosphere, with consequences for phase changes and chemistry. The influence of radiative heat transfer on the gas dynamics of the impact-generated atmosphere is investigated further in Chapter 6.

Another issue that deserves further consideration is the thermal model used for the lunar surface. The simulations in this chapter used the surface temperature model of Stewart et al. (2011), which approximates day-side temperatures well, but does not take into account the cooling of the surface during the lunar night (although night side temperatures are so cold that this is not expected to be a significant issue). More significantly, this model does not account in any way for lunar topography, except inasmuch as selected regions of permanent shadow are specified. Chapter 5 introduces stochastic, small-scale surface roughness into the surface thermal model in order to investigate how the distinctive lunar surface thermal environment affects volatile transport, loss and deposition.

Chapter 5: The Influence of Lunar Surface Roughness on Volatile Transport[1]

5.1. CHAPTER OVERVIEW

This chapter discusses the influence of lunar surface roughness on the transport, loss and sequestration of water, both in the short-term collisional stage of the post-impact atmosphere (discussed in Chapter 4), as well as in the late-term collisionless limit. The simulations presented in this chapter used the rough surface temperature model(s) described in Section 3.4. Although this dissertation focuses on the fate of impact-delivered water, the lunar surface thermal environment may also influence the behavior of other volatile species, delivered by other source mechanisms. Furthermore, as mentioned in Section 2.3, similar thermal environments may exist on other 'airless' bodies. Thus, given the broad scope of the problem, this chapter begins by investigating the general influence of lunar surface roughness on volatile transport (through the collisionless Monte Carlo simulations described in Section 3.4.4), before discussing the more specific case of an impact-generated atmosphere.

Section 5.2 examines the question of whether it is possible to gauge the influence of sub-pixel temperature variations on volatile transport, preliminary to detailed simulations. Section 5.3 focuses on the simulations labeled Case 1 and Case 2 in Table

---

[1] Parts of Chapter 5 have been submitted for publication as part of Prem, P., Goldstein, D. B., Varghese, P. L. & Trafton, L. M., 'The influence of surface roughness on volatile transport on the Moon', *Icarus* (2017). P.P. (the author of this dissertation) performed the Monte Carlo simulations described in that work, and drafted the manuscript. D.B.G., P.L.V. and L.M.T. provided useful ideas, suggestions and feedback, and proofread the manuscript.

3.1, which investigate how surface roughness affects the fate of exospheric water and exospheric structure and test the sensitivity of results to the sub-pixel temperature distribution. Section 5.4 discusses the results of Case 3 in Table 3.1, intended to illustrate the significance of desorption activation energy. Section 5.5 couples the rough surface temperature model to the DSMC simulations presented in Chapter 4 to explore the consequences of surface roughness for volatile transport in the more complex case of an impact-generated atmosphere. Section 5.6 summarizes key results and conclusions.

5.2. GAUGING THE INFLUENCE OF SURFACE ROUGHNESS ON VOLATILE TRANSPORT

Surface temperature is a useful measure of the mobility and stability of water (and other volatiles) over the lunar surface. However, when roughness is introduced into a surface temperature model, there is no longer a single temperature associated with a given latitude and time of day (instead, there is a distribution of temperatures). This raises the question of how best to think about volatile transport in the presence of surface roughness; can we identify a representative temperature, or another suitable parameter, to measure the influence of surface roughness on the mobility of a given volatile species? If a suitable parameter can be identified, the advantage is that this metric can then be used to compare various rough surface temperature models (e.g. Cases 1 to 3 in Table 3.1) or to estimate how the surface roughness affects the transport of various volatile species, preliminary to detailed simulations, which are often computationally intensive.

Due to the exponential relationship between surface temperature and molecular residence time expressed by Eq. (3.1), a major consequence of introducing surface roughness is the change in the distribution of residence times at any location on the lunar surface. Long residence times on cold sub-pixel surfaces (shadowed or simply tilted away from the Sun) may slow the overall rate of migration of molecules over the day side, but this effect should be significant only at temperatures where the surface residence time is longer than the ballistic timescale – otherwise, any time spent on the surface is a negligible part of the molecule's lifetime. Other than residence time, sub-pixel temperatures also determine the mean velocity with which molecules leave the surface. However, since mean thermal velocity is less strongly influenced by surface temperature than residence time ($\bar{v} \propto \sqrt{T_{surf}}$ vs. $t_{res} \propto e^{E_a/k_B T_{surf}}$), roughness should have a comparatively small influence on molecular velocities and exospheric scale height.

One way to account for the change in the sub-pixel temperature distribution is to define an 'effective' pixel temperature, T_{eff}, based on the average residence time. T_{eff} can be computed by sampling a large number, n, of sub-pixel locations to find an average residence time, $t_{res,avg}$, and then inverting Eq. (3.1), such that:

$$T_{eff} = \frac{E_a}{k_B \ln(\nu_0 t_{res,avg})} \qquad \text{where} \quad t_{res,avg} = \frac{\sum_{i=1}^{n} t_{res,i}(T_{surf,i})}{n} \tag{5.1}$$

Here, $t_{res,i}$ is the residence time at the i^{th} sub-pixel surface with temperature $T_{surf,i}$. For a smooth surface, $T_{eff} = T_{surf}$, where T_{surf} is given by Eq. (3.6).

Figure 5.1 compares T_{eff} for Cases 1 and 2. The presence of cool/shadowed sub-pixel surfaces in Case 1-R and of "deep shadows" (specified to be at the pre-dawn temperature) in Case 2 are reflected in colder effective temperatures in those cases.

However, Figure 5.1 also illustrates how the parameter T_{eff} may be misleading. Due to the steep exponential increase in residence time at lower temperatures, the average residence time in Eq. (5.1) is largely determined by the lowest sub-pixel temperatures, leading to an overstatement of the importance of colder surfaces. For instance, the very small fraction of "deep shadows" introduced in Case 2 should not cause a large swathe of the lunar day-side to behave as if it were at night-time temperatures (as suggested by Figure 5.1(c)).

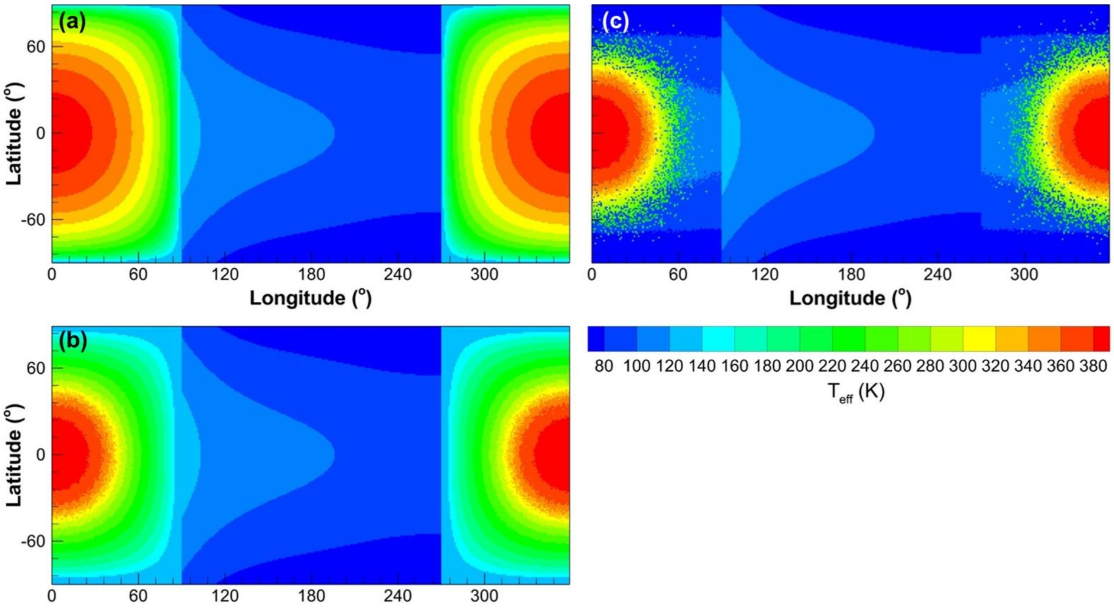

Figure 5.1: Effective temperature, T_{eff}, based on average residence time for (a) Case 1-S, (b) Case 1-R and (c) Case 2, computed by sampling $n = 1000$ points per pixel. Midnight is at 180° longitude and the dawn terminator is at 270° longitude. Note that the night side is modeled as smooth in all three cases.

It should be noted that the parameter T_{eff} captures only the influence of sub-pixel roughness on residence time, and not on volatile transport as a whole; e.g. although many of the rough day-side surface pixels in Figure 5.1(b) have effective temperatures considerably colder than the corresponding smooth pixels, average day-side residence times of water molecules are still very short compared to the ballistic time-scale. To obtain a more holistic measure of how the different surface boundary conditions affect volatile transport, we can compute a 'sticking probability' p_{stick} for each surface pixel, defined as the fraction of molecules interacting with each pixel that are likely to have residence times longer than the ballistic timescale, given by:

$$p_{stick} = \frac{\sum_{i=1}^{n} s_i}{n} \tag{5.2}$$

where $s_i = 1$ if $t_{ballistic,i}/t_{res,i} < R_i$ or 0 if $t_{ballistic,i}/t_{res,i} \geq R_i$

Again, n is the number of sub-pixel locations sampled within each pixel; $t_{ballistic,i}$ and $t_{res,i}$ are the ballistic time and residence time, respectively, associated with location i. The ratio of these two times is compared to a random number R_i to determine whether a molecule sampling that location would reside for longer than the ballistic timescale. Residence time $t_{res,i}$ is found from Eq. (3.1) and the ballistic time-scale $t_{ballistic,i}$ is a function of gravitational acceleration ($g = 1.62$ m/s^2 for the Moon), the temperature $T_{surf,i}$ at location i and molecular mass ($m = 29.9 \times 10^{-27}$ kg for water), given by Hodges (1972) as:

$$t_{ballistic,i} = \frac{1}{g}\sqrt{\frac{8k_B T_{surf,i}}{\pi m}} \tag{5.3}$$

Figure 5.2 shows the sticking probabilities for the five different cases described in Table 3.1. Although the bolometric temperature of each pixel in all five cases is near-identical, it can be seen that sticking probabilities are noticeably different, due to the different sub-pixel temperature distributions and/or different desorption activation energies. In Case 3, I use a desorption energy for H_2O that is 10% greater than is used in Cases 1 and 2. It should also be noted that different species would have different desorption energies, with the interesting consequence that the same degree of roughness may affect the transport of some species more or less than others.

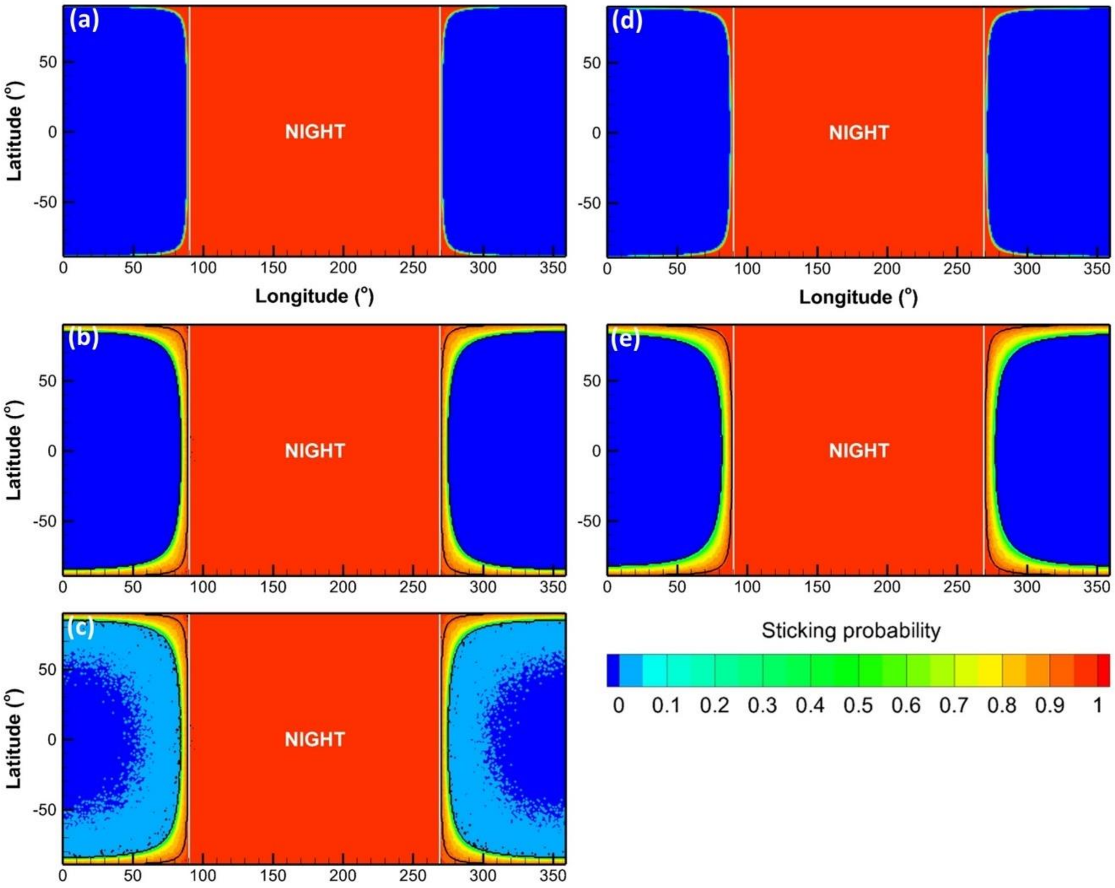

Figure 5.2: Sticking probabilities, from Eq. (5.2), for (a) Case 1-S, (b) Case 1-R, (c) Case 2, (d) Case 3-S and (e) Case 3-R, computed by sampling n = 1000 points per pixel. The black line contours mark regions where the difference between rough and smooth surface sticking probabilities exceeds 0.01.

Comparing rough and smooth surface sticking probabilities in Figure 5.2, it can be inferred that surface roughness plays a significant role in volatile transport chiefly at high solar incidence angles i.e. at the dawn/dusk terminators and around the poles – despite the fact that sub-pixel temperature distributions differ globally. To quantify what this means for volatile migration, loss and capture, we turn to the results of the previously described Monte Carlo simulations.

5.3. ROLE OF ROUGH SURFACE TEMPERATURE DISTRIBUTIONS

This section discusses how rough surface temperature distributions affect volatile transport, based on the illustrative Monte Carlo simulations described in Section 3.4.4, focusing on Cases 1 and 2 in Table 3.1. To recap, these simulations track the evolution of a temporary exosphere created by the release of 100 kg of water, initially uniformly and globally distributed over the lunar surface.

Though not intended as a model for any specific source mechanism, the exosphere that results from these initial conditions resembles the late (collisionless) stage of an impact-generated atmosphere, in which volatile transport is sustained by the sublimation and diffusive transport of water adsorbed to the night side at dawn. Since these Monte Carlo simulations are collisionless, they are much less computationally intensive than the DSMC simulations and can be run more easily for much longer periods of simulation time, until a quasi-steady state is reached. (Note that the exosphere never reaches a true equilibrium with the underlying surface, since all the simulated molecules are ultimately photodestroyed or cold-trapped.) Figure 5.3 is a representative snapshot of exospheric column density in the vicinity of the South Pole, showing the characteristic enhancement in exospheric density at the dawn terminator.

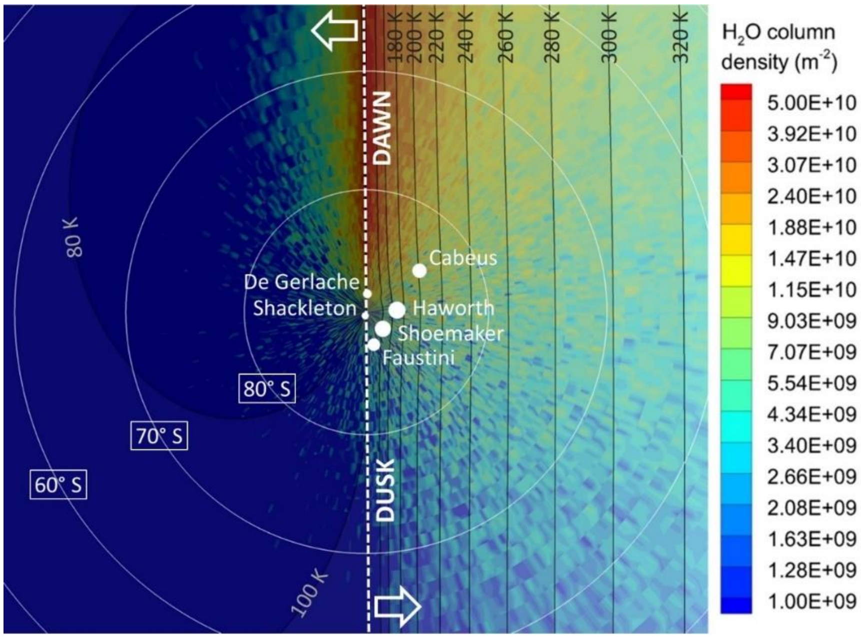

Figure 5.3: Representative snapshot of exospheric column density in the vicinity of the lunar South Pole, superimposed over a surface (bolometric) temperature map with line contours marked. At this stage, the exosphere is sustained by sublimation of night side adsorbate at sunrise, causing an enhancement in column density at the dawn terminator. The six nominal craters included in the Monte Carlo simulations are also marked; arrows indicate the direction of rotation of the dawn/dusk terminators.

Figure 5.4(a) shows the fate of the initialized exosphere over the course of seven lunar days for Case 1-S, Case 1-R and Case 2, while Figure 5.4(b) focuses on how the amounts of photodestruction and cold trap capture differ between these three cases. Seven lunar days after initialization, it can be seen that slightly less water has been photodestroyed in the two rough surface cases. This is related to the fact that molecules adsorbed to the lunar surface are protected from photodestruction – an effect that is significant only when surface residence times are comparable to or longer than the ballistic time-scale. In Case 1-S, only the night-side surface offers such temporary shelter, since residence times on the day side are very short compared to ballistic times.

The rough surface temperature model introduces sub-pixel surfaces that are both warmer and cooler than the corresponding smooth pixel temperature at any time of day, but the influence of longer residence times on the cooler surfaces (particularly shadowed surfaces) outweighs that of reduced residence times at the warmer surfaces. Thus, the day-side shadows present in Case 1-R and the additional “deep shadows” present in Case 2 increase the amount of temporary shelter available to migrating molecules, which acts to reduce the amount of photodestruction. (It should be noted that there may be mechanisms for the destruction of adsorbed water molecules, e.g. space weathering, which are not included in the model.)

Shadows and cool surfaces only provide temporary shelter, thereby slowing the rate of migration of molecules to regions of permanent shadow near the lunar poles. Molecules desorb from cool surfaces with a reduced mean velocity and ultimately spend more time aloft before cold trap capture if cool surfaces are encountered during migration to the poles. (Since the ballistic hop length $\propto T$ while the ballistic timescale $\propto \sqrt{T}$, it takes less time for a molecule to cover a given distance through a few long hops than through a greater number of short hops.) One might then expect that the presence of shadows renders migrating molecules *more* susceptible to photodissociation. Thus, our finding of *reduced* photodestruction in the two rough surface cases is somewhat counterintuitive. It is also observed that there is ~4-7% more water cold-trapped at both poles in the two rough surface cases. This preferential depletion of the exosphere by cold-trap capture vs. photodestruction suggests that the important factor is the *location* of surfaces that offer temporary shelter, rather than their mere presence. Specifically, the large proportion of shadows at high solar incidence angles increases the availability of temporary shelter around the poles, as seen in Figure 5.2. This has the effect of (temporarily) capturing and concentrating migrating molecules in the vicinity of the poles, from where they are more likely to reach a permanent cold trap within a few hops after desorption, rather than being photodestroyed.

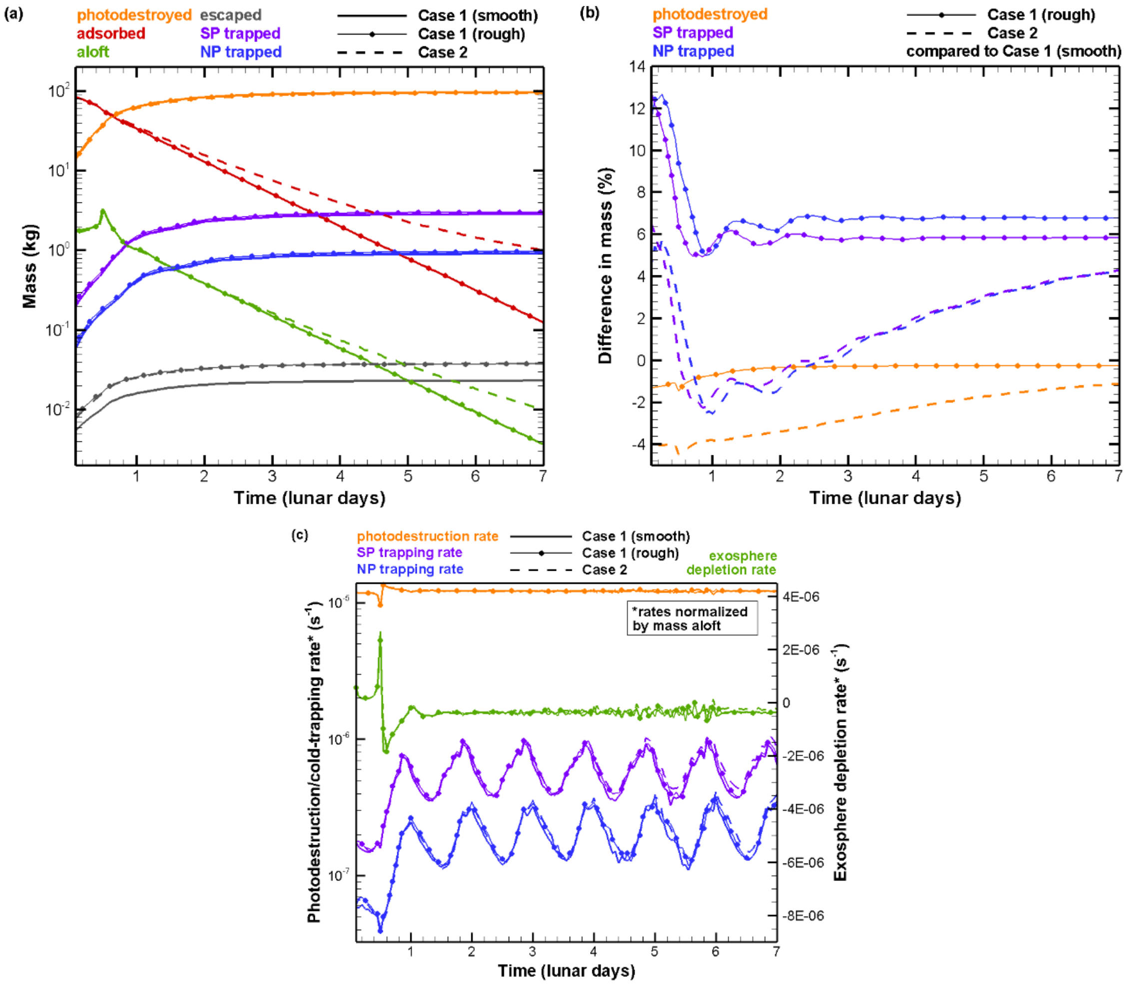

Figure 5.4: (a) Comparison of amounts of water adsorbed, aloft, photodestroyed, cold trapped and escaped over the course of seven lunar days for Cases 1 and 2; (b) percentage differences in mass photodestroyed and cold-trapped in Case 1-R and Case 2 relative to Case 1-S; and (c) rates of photodestruction and cold-trapping in the three cases, normalized by mass of water aloft.

In a different context, Schorghofer and Taylor (2007) point out that there is an optimum surface temperature range that maximizes subsurface water content – above this optimum temperature range, surface ice accumulation is low and below the optimum temperature range, adsorbed molecules do not diffuse efficiently into the subsurface and are thus more susceptible to space weathering. It is interesting to note that there appears to be a similar optimum temperature range for polar surfaces, which facilitates the accumulation of water (and perhaps other volatiles) at permanently shadowed regions. Surfaces above this optimum temperature range would not have the effect of concentrating migrating molecules in the polar region, while surfaces below the optimum temperature range may themselves act as small cold traps, preventing molecules from migrating to regions that are more favorable for long-term stability.

Reinforcing the idea that the mobility of volatiles near the poles plays a crucial role in cold trap capture, Figure 5.4(c) shows a diurnal fluctuation in the rate of cold trap capture, with the trapping rate higher by almost a factor of two when the dawn terminator is located over the cold traps, compared to when the dusk terminator is at the same location. As illustrated by Figure 5.3, the quasi-steady exosphere that develops after the initial transient flow is sustained by the sublimation of night side adsorbate at sunrise. Therefore, when the dawn terminator is over a cold trap, a relatively large amount of vapor is mobilized in the vicinity of that cold trap, leading to a greater amount of cold trapping at that time. Molecules adsorbed to shadowed or sloping surfaces in the vicinity of the poles act as an additional source of volatile material that can be mobilized during the course of the lunar day. During the lunar night, water molecules largely remain adsorbed to the surface and are relatively immobile; as a result, rates of migration and cold-trap capture during the night-time are low.

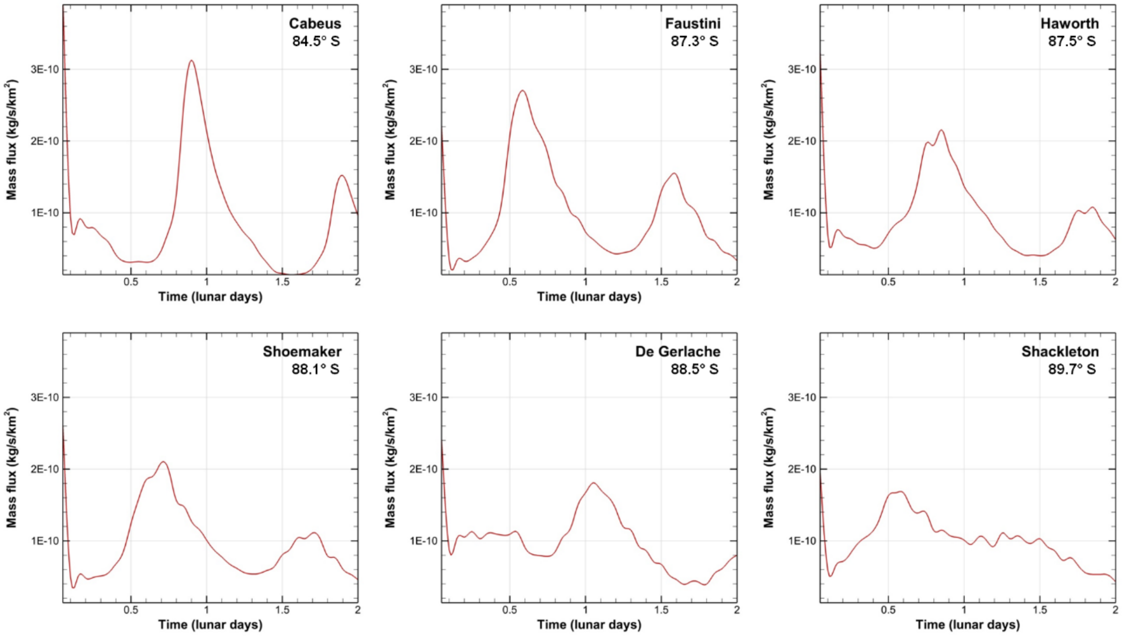

Figure 5.5: Depositional flux at each of the six modeled South Polar cold traps over the first two lunar days after initialization, for Case 2. The diurnal peaks in depositional flux at each cold trap coincide approximately with times when the dawn terminator is at the same longitude as that cold trap. The flux at cold traps closer to the pole appears less sensitive to the location of the terminator.

Figure 5.5 shows the depositional flux at each of the six modeled South Polar cold traps in Case 2. (Similar trends are seen in the other modeled cases.) The peak flux of water to each cold trap coincides with the passage of the dawn terminator. The average fluxes to each of the South Polar cold traps are found to be of comparable magnitude, without the preferential cold-trapping at low latitudes found by Moores (2016). This may be due to the different initial conditions adopted in this work; Moores considers a point source of water located at the equator, whereas I consider a global source.

Returning to Figure 5.4; an interesting feature in Figure 5.4(a) is the slightly higher rate of escape in the two rough surface cases compared to the smooth surface case. If we look at the latitudinal distribution of escaping molecules, shown in Figure 5.6(a), it can be seen that escape occurs preferentially at lower latitudes in both rough and smooth surface cases. Molecules escape when they acquire a velocity greater than lunar escape velocity after an encounter with the surface. We assume that all molecules leave the surface with a velocity drawn from a Maxwellian distribution at the local surface temperature $T_{surf,i}$, according to which the probability of a molecule of mass m having speed v is given by:

$$f\left(v, T_{surf,i}\right) = 4\pi \left(\frac{m}{2\pi k_B T_{surf,i}}\right)^{\frac{3}{2}} v^2 \exp\left(-\frac{mv^2}{2k_B T_{surfi}}\right) \qquad (5.4)$$

In the rough surface model, there is a distribution of temperatures within each pixel, which can be represented by a probability function $g(T_{surf,i})$. Therefore, the probability that a molecule encountering a pixel i will leave with a speed greater than the lunar escape speed $v_{esc} = 2.38$ km/s can be obtained:

$$p(v > v_{esc}) = \int_0^{T_{max}} g(T_i)\left(1 - \int_0^{v_{esc}} f(v, T_i)dv\right) dT_i \qquad (5.5)$$

The probability of escape, $p(v > v_{esc})$ varies with mean solar incidence angle. Figure 5.6(b) compares the variation of $p(v > v_{esc})$ for a rough surface (with $g(T_{surf,i})$ as shown in Figure 3.4(c)) and a smooth surface (with $g(T_{surf,i}) = \delta(T_{surf,i} - T_{surf})$) where T_{surf} is given by Eq. (3.6). It can be seen that the probability of escape over a rough surface is generally higher than over a smooth surface, due to the exponential dependence of escape velocity on temperature, consistent with what we find in the Monte Carlo simulations.

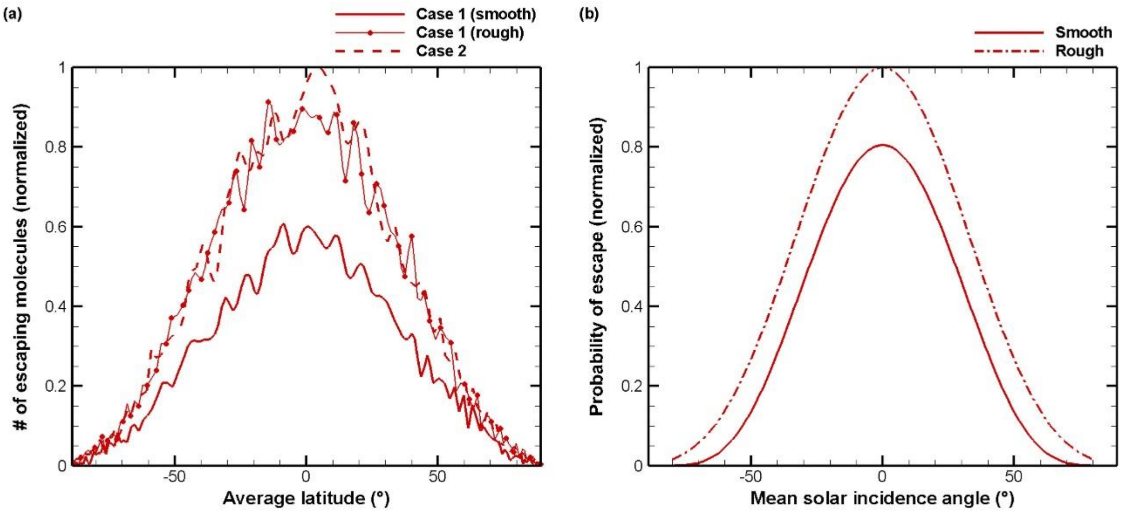

Figure 5.6: (a) Relative amount of escape occurring in various latitude bands (longitudinally averaged) in Case 1-S, Case 1-R and Case 2, during the first lunar day after initialization; and (b) analytically computed escape probability as a function of mean solar incidence angle for a smooth surface (with a uniform sub-pixel temperature) and a rough surface (with a distribution of sub-pixel temperatures).

Figure 5.4(b) shows that including a small proportion of "deep shadows" in Case 2 slows the rate of exospheric depletion due to photodestruction and cold trap capture (though the amount of escape is hardly affected). As shown in Figure 5.2(c), the inclusion of these colder shadows further increases the surface area over which molecules may reside for times comparable to or much longer than the corresponding ballistic times. This slows the rate of accumulation at the poles, causing the lag in cold trap deposition seen in Figure 5.4(b), and means that at any given time, a smaller proportion of molecules are aloft and susceptible to photodestruction, though those molecules that are aloft are just as likely to be photodestroyed as in the other two cases, as confirmed by Figure 5.4(c). Despite the initial lag, it can be seen from Figure 5.4(c) that the normalized cold-trapping rate in Case 2 becomes higher than in the other two cases at later times, i.e. a greater proportion of exospheric molecules are cold-trapped.

It can be seen from Figure 5.4(a) that the net effect of the various trends operating in Case 2 is that – at later times in particular – there is not only more water adsorbed to the lunar surface but also more water in the residual exosphere, sustained by the desorption of molecules adsorbed to temporarily shadowed surfaces. Seven days after initialization, it is seen that the residual exosphere decays exponentially in all three cases, but at a lower rate in Case 2 compared to Case 1-S and Case 1-R. The mass of the exosphere m at some subsequent time t can be expressed as:

$$m = m_0 \exp[-rt] \tag{5.6}$$

where r is a decay rate constant of magnitude ~3.6×10^{-7} s^{-1} for Case 1-S and Case 1-R and ~2.4×10^{-7} s^{-1} for Case 2; and m_0 is the exospheric mass at seven days after initialization (~0.0035 kg for Case 1-S and Case 1-R and ~0.01 kg for Case 2). After one more lunar day, the exosphere in Case 2 would contain ~4 times as much water, and it would take ~3 times longer for the exospheric mass to decrease to 0.001 kg.

Thus, although the “deep shadows” introduced in Case 2 are temporary in nature and constitute only a small fraction of all shadows, they have a significant effect on the longevity and density of the exosphere, as well as the amount of water photodestroyed and cold-trapped. The influence of these colder shadows is particularly noticeable over the first several lunar days after the volatile release. I ended the simulations at seven days after initialization, by which stage the normalized rates shown in Figure 5.4(c) appear to have approached constant values (or vary about some constant mean value in the case of cold-trapping rates). However, it should be noted that cold trap accumulation and photodestruction continue beyond this, so the percentage differences in cold-trapping and photodestruction may change beyond seven days, particularly for Case 2.

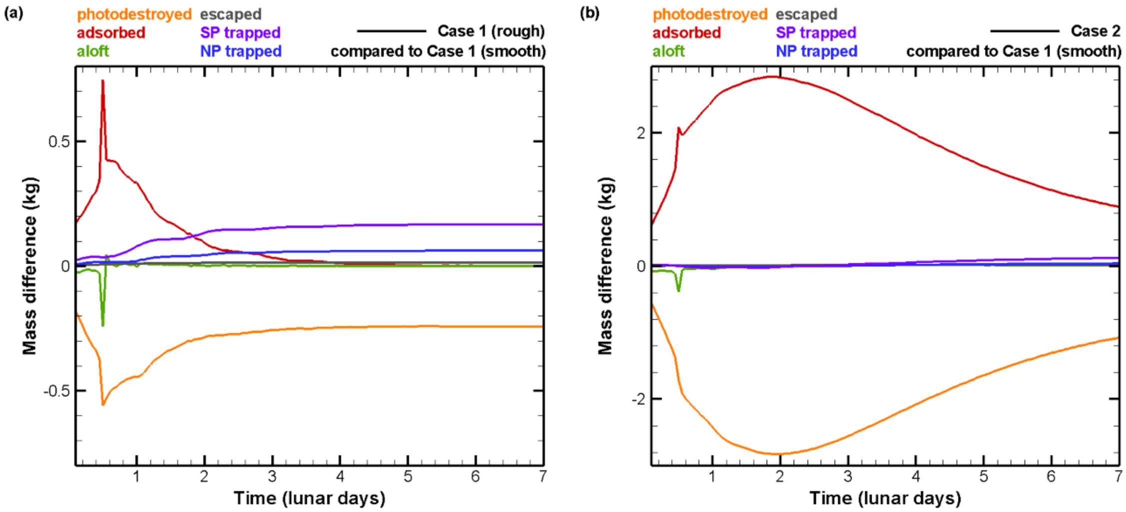

Figure 5.7: Difference in mass photodestroyed, adsorbed, aloft, escaped and cold-trapped between (a) Case 1-R and (b) Case 2, relative to Case 1-S. Differences in the mass escaped and aloft are several orders of magnitude less than the other quantities at later times. Note the different y-axis ranges in the two plots.

Figure 5.7 shows the differences in cumulative mass photodestroyed, adsorbed, aloft, escaped and cold-trapped vs. time for Case 1-R and Case 2, both relative to Case 1-S. The reduced amount of photodestruction in Case 1-R relative to Case 1-S is largely compensated for by increased cold trapping, and to a much smaller degree by increased escape. Meanwhile, most of the difference in photodestruction between Case 2 and Case

1-S is due to the increased surface area favorable for adsorption in Case 2, with increased cold-trapping accounting for the remainder of the difference.

Since the 1% of “deep shadows” in Case 2 are specified to be at a very low (perhaps unrealistically low) temperature, residence times in these regions are very long. At higher latitudes, some of these deep shadows are also persistent (i.e. surfaces remain shadowed for much of the lunar day) and may act as small, de facto cold traps. Seven days after initialization, ~0.4 kg of water is adsorbed in such regions. If the simulations were continued further, the total amount of water cold-trapped in Case 2 would likely asymptote to a value less than in Case 1-R, but greater than in Case 1-S. The objective of Case 2 was to test the sensitivity of simulation results to how we model the temperature of shadows cast by small-scale features. Comparing Case 1-S, Case 1-R and Case 2, we infer that while the presence of shadows in general leads to preferential depletion of the exosphere via cold-trap capture rather than photodestruction, the distribution of shadow temperatures affects the rate at which these processes occur.

Figure 5.8 examines differences in exospheric structure between Case 1-S, Case 1-R and Case 2, seven lunar days after initialization. Figures 5.8(a) and 5.8(c) primarily reflect differences in the total exospheric mass at this time. In all three cases, the overall exospheric column density is greater at 75° latitude, reflecting a redistribution of mass from warmer equatorial regions to colder high latitudes. This redistribution also appears slightly more pronounced in the two rough surface cases, with the peak column density (at the dawn terminator) greater at 75° vs. 0° by a factor of 2.5 in Case 2 and 2.1 in Case 1-R vs. 1.8 in Case 1-S. This is qualitatively consistent with the increased availability of colder surfaces at higher latitudes when surface roughness is incorporated. The normalized column density plots (Figures 5.8(b) and 5.8(d)) show that exospheric structure is very similar in all three of the modeled cases. The most significant difference, clearest at equatorial latitudes, is an appreciable reduction and slight broadening of the (normalized) dawn terminator column density peak in the two rough surface cases, i.e. a blurring of the terminator by surface roughness.

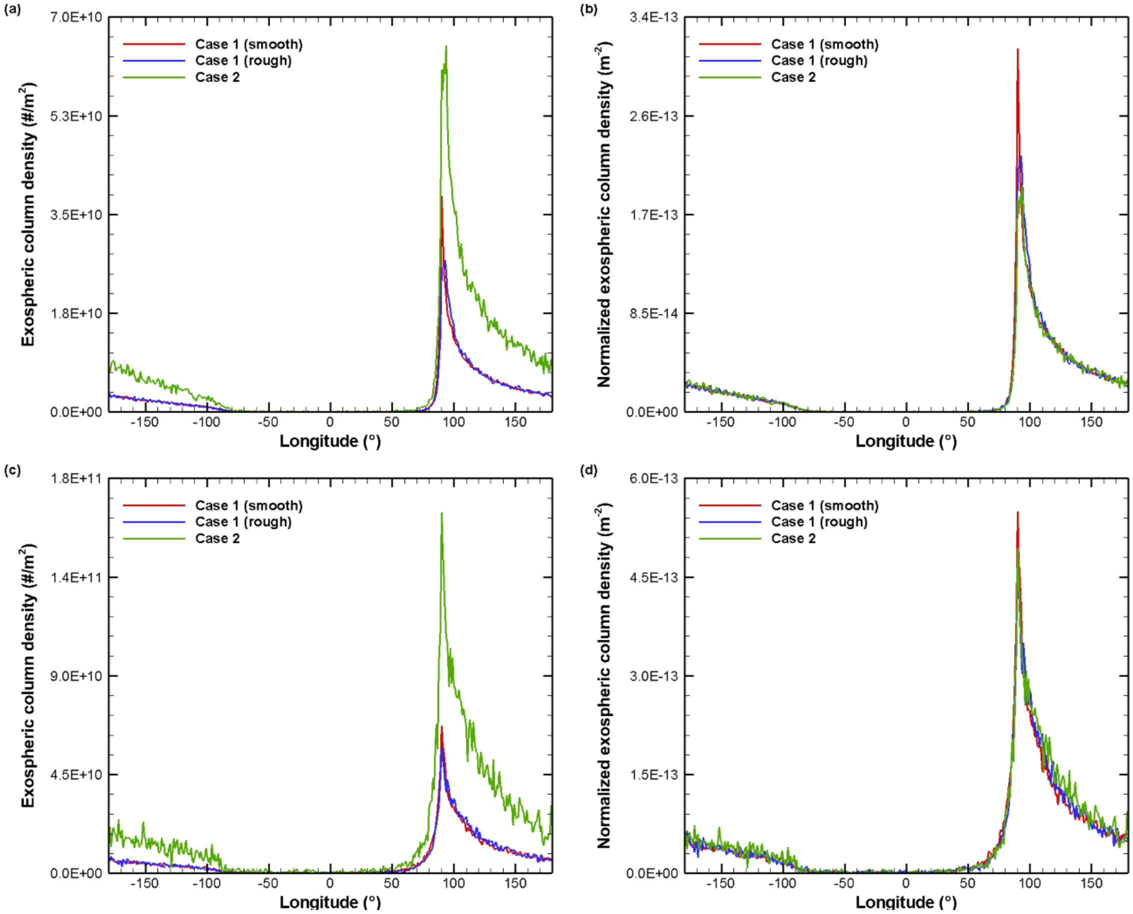

Figure 5.8: Exospheric column density vs. longitude for Cases 1 and 2, seven days after initialization, averaged over (a) a latitudinal band ~16° wide centered at the equator and (c) latitudinal bands ~3.8° wide centered at 75° N and S; (b) and (d) are normalized versions of (a) and (c) respectively, normalized by the total exospheric mass. 0° longitude corresponds to midnight. Note the different y-axis ranges in all four plots.

5.4. Role of Desorption Activation Energy

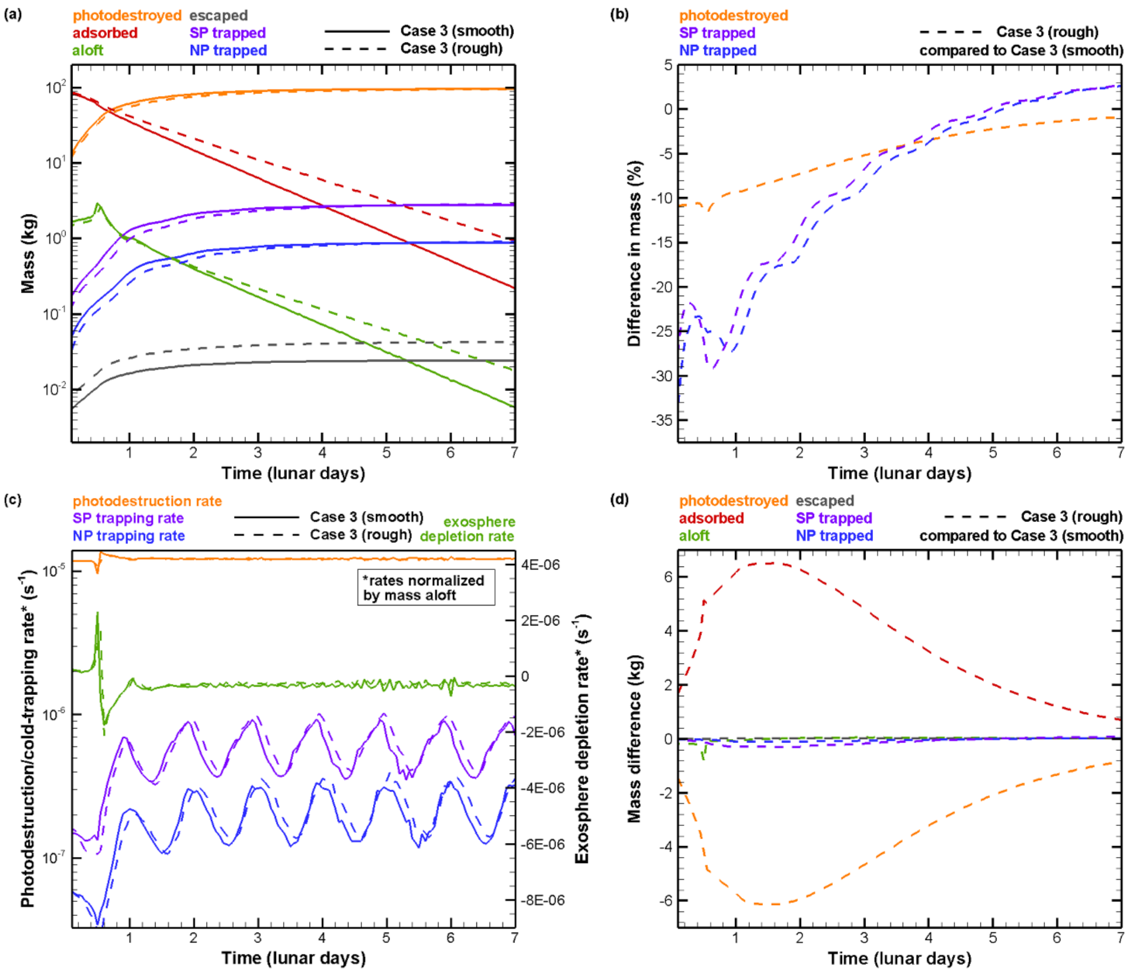

Figure 5.9: (a) Mass of water adsorbed and aloft, together with cumulative mass photodestroyed, cold trapped and escaped vs. time; (b) percentage difference in mass photodestroyed and cold-trapped; (c) rates of photodestruction and cold-trapping, normalized by mass of water aloft; and (d) difference in mass photodestroyed, adsorbed, aloft, escaped and cold-trapped between Case 3-S and Case 3-R.

The residence time of molecules on a surface is determined by both the surface temperature and the energetics of the gas-surface interaction. Section 5.3 dealt with the former factor, while this section examines the latter. Specifically, this section focuses on the results of the set of simulations labeled Case 3 in Table 3.1, which use the same surface distributions as in Case 1, but model residence times using a higher desorption activation energy E_a in Eq. (3.1).

Figure 5.9 shows the fate of the initialized exosphere over the course of seven lunar days for Case 3-S and Case 3-R. The change in desorption energy results in residence times that are O(10) times longer than in Case 1 e.g. at the coldest modeled day-time temperature of 130 K, the residence time in Case 3 is 70.95 h, compared to 1.76 h in Case 1. However, residence times in Case 3 are still short relative to the length of lunar day and therefore do not introduce de facto cold traps as in Case 2. The increase in desorption energy also means that residence times increase more steeply at low temperatures i.e. volatile transport is more sensitive to the distribution of surface temperatures introduced by sub-pixel roughness. This is illustrated by Figure 5.4 – in Case 1, the introduction of surface roughness affects surface sticking probabilities within 4° of the terminator/poles, whereas in Case 3, roughness affects sticking probabilities within 7° of the terminator/poles. Due to the increased residence times in Case 3, it can be seen from Figure 5.9(a) and 5.9(b) that it takes longer than in Case 1 for cold trap accumulation in the rough surface case to overtake that of the smooth surface case. However, surface roughness still has the effect of enhancing cold trap capture, as illustrated by the higher normalized cold-trapping rates in Figure 5.9(c), which indicate that a greater proportion of exospheric molecules are cold-trapped in the rough surface case. The enhancement in cold-trapping due to the introduction of surface roughness in Case 3 is also more pronounced than in Case 1, as anticipated from the increased sensitivity of volatile transport to the rough surface temperature distribution in Case 3. Figure 5.9(c) also reveals more clearly a pattern also seen in Figure 5.5(c), viz., the enhancement in cold-trapping occurs primarily during the half of the lunar day when the cold traps are on the day-side, surrounded by anisothermal pixels; at night, pixels in both rough and smooth cases are modeled as isothermal and there is very little difference in cold-trapping rates between the two cases.

Figure 5.9(d) shows the differences in cumulative mass photodestroyed, adsorbed, aloft, escaped and cold trapped vs. time for Case 3-R relative to Case 3-S. This plot is qualitatively very similar to Figure 5.7(b), which compares the same quantities in Case 2 to Case 1-S. In both Case 3-R and Case 2, the exospheric lifetime is longer compared to the respective smooth surface cases, and differences in the amount of photodestruction are largely due to the greater fraction of molecules adsorbed to and thus sheltered by cooler/shadowed surfaces. However, the reason for these trends is different in the two cases – in Case 2, it is the increased prevalence of cold surfaces (some of which act as de facto cold traps) that is responsible, while in Case 3-R, it is longer residence times on surfaces with the same temperatures as in Case 1-R. Ultimately, both of these factors increase sticking probabilities at low solar incidence angles, thereby affecting the rate and magnitude of cold-trap capture and photodestruction.

Since no sub-pixel shadows act as de facto cold traps in Case 3, it is anticipated that if these simulations were continued beyond seven lunar days, the difference in the amount of water photodestroyed between the rough and smooth surface cases would continue to decrease, while the differences in the amount of water cold-trapped at both poles would continue to increase – ultimately accounting for the entirety of the difference in photodestruction, as in Figure 5.7(a) for Case 1.

5.5. IMPLICATIONS FOR AN IMPACT-GENERATED ATMOSPHERE

Sections 5.3 and 5.4 discuss how volatile transport and loss in a collisionless exosphere are affected by the presence of surface roughness. The quasi-steady state attained in these simulations resembles the late-term collisionless limit of an impact-generated atmosphere (Stewart, 2010), in which the exosphere is sustained by the sublimation of night-side adsorbate at sunrise. Indeed, source mechanisms other than large impacts may also give rise to qualitatively similar exospheres (Schorghofer, 2014; Grava et al., 2015). However, as discussed in Chapter 4, *short-term* volatile transport after a comet impact is distinctly different, in that the impact-generated atmosphere is collisional at this stage, and has a characteristic structure different from that of the exospheres modeled in Cases 1 to 3. This section investigates how surface roughness affects transport and loss processes during this, more complex, phase.

In the simulations presented in this section, the surface temperature models used in Case 1-S and Case 1-R were coupled to the DSMC code. The 60°, 30 km/s simulation presented in Chapter 4 was paused at 1 hour after impact and then resumed using the new surface temperature model. This was done in order to avoid re-running the more computationally intensive, multi-domain calculations necessary to capture the initial rapid expansion of the impact-generated vapor. At the 1 hour mark, most of the material in the simulation has not yet interacted with the surface and so, introducing new temperature models at this stage should not significantly distort our results, particularly when the objective is to compare cases with and without surface roughness. Note that the Case 1-S temperature model is based on Eq. (3.6), from Hurley et al.'s (2015) recent fit to Diviner observations, which is different from the temperature model used in Chapter 4, from Stewart (2010). The updated model accounts for the effects of thermal inertia in the cooling of the surface during the lunar night, and day-side temperatures are also slightly different (more accurate).

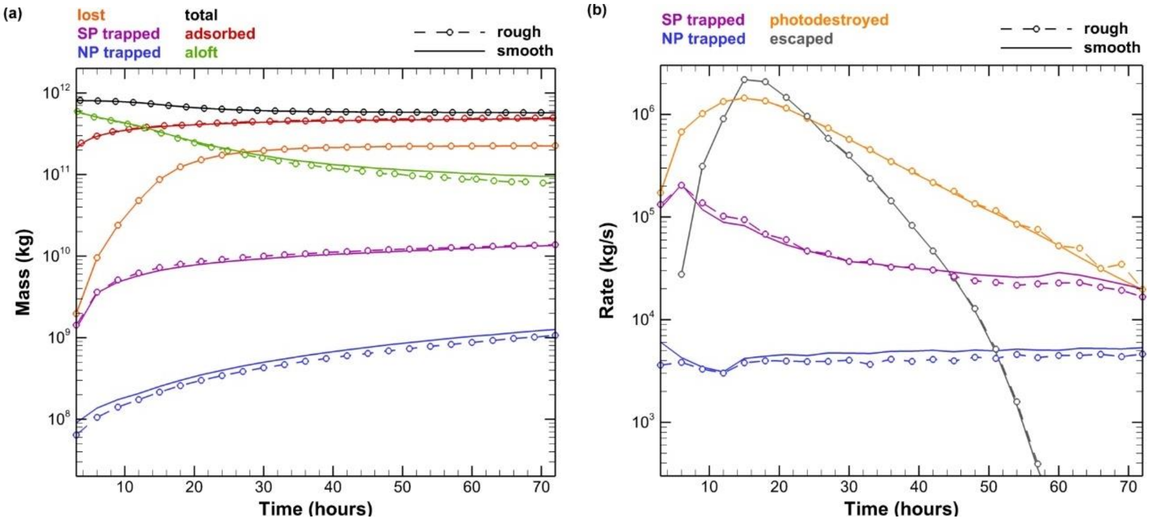

Figure 5.10: (a) *Cumulative* mass lost (photodestroyed + escaped) and cold-trapped, and *instantaneous* mass adsorbed and aloft for simulations of the impact-generated atmosphere with and without surface roughness, over the first 72 hours after impact. Also shown is the total mass left in the simulation (adsorbed + aloft). (b) Instantaneous rates of photodestruction, escape and cold-trapping in the two scenarios.

Figure 5.10(a) compares the mass lost (photodestroyed + escaped), cold-trapped, adsorbed and aloft over the first 72 hours after impact, for simulations of the impact-generated atmosphere with and without surface roughness. It can be seen that there is negligible difference in the amount of material lost since, at this stage, the rates of photodestruction and escape are predominantly governed by the far-field structure of the atmosphere rather than by gas-surface interactions. In both cases, vapor close to the surface is effectively shielded from photodestruction, and the thickness of the overlying atmospheric column makes it difficult for molecules to escape after a single surface interaction. As in the collisionless simulations, there is slightly more water adsorbed to the surface in the rough surface case ($\sim 2 \times 10^{10}$ kg more at 72 hours), but since this is only ~3 % of the total mass in the simulation, differences in atmospheric structure between the rough and smooth surface cases are virtually imperceptible. From Figure 5.10(b), it can be seen that the rate of cold-trapping at the North Pole is consistently lower for the rough surface case, while at the South Pole, the cold-trapping rate is initially higher for the rough surface case, but becomes lower at around 20-30 hours after impact. At 72 hours, ~15 % less water is cold-trapped at the North Pole, and ~2 % more water is cold-trapped at the South Pole in the rough surface case.

Figure 5.11 looks more closely at the differences in cold-trapping between simulations with/without surface roughness by comparing the cumulative amount of cold-trapping at each of the six modeled South Polar craters. It can be seen that although the overall amount of cold-trapping at the South Pole is higher for the rough surface case, two craters (Shackleton and de Gerlache) have consistently lower amounts of cold-trapped water. These happen to be the two highest-latitude cold-traps, but the inter-crater differences seen in Figure 5.11 are not simply a function of latitude. Instead, there appear to be a combination of factors at play.

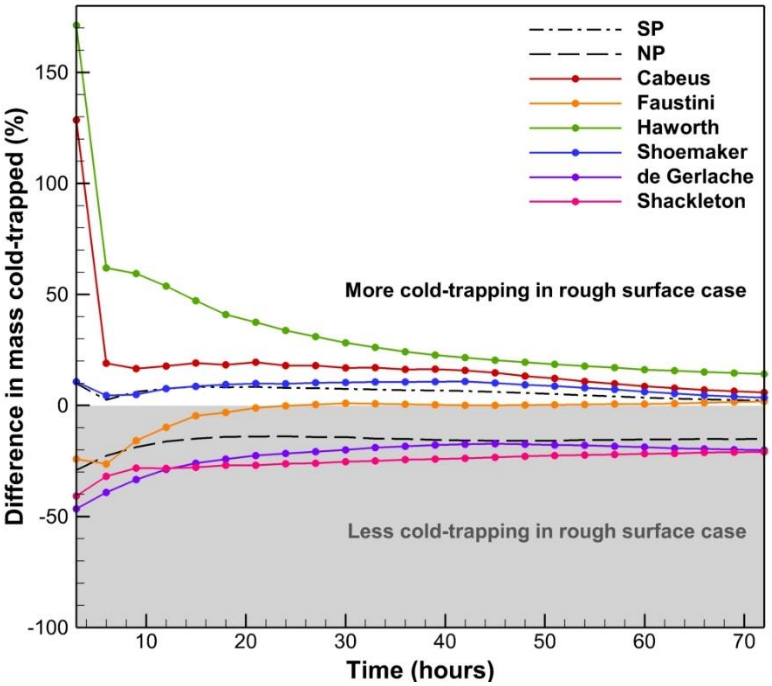

Figure 5.11: Percentage difference in cumulative mass cold-trapped at the North and South Pole for simulations of the impact-generated atmosphere with and without surface roughness, over the first 72 hours after impact. Differences in cold-trapping at the individual South Polar craters are also plotted.

To better understand the differences in cold-trap capture discussed above, it may be instructive to visualize how water migrates over the lunar day-side (recall that night-side migration is minimal due to exponentially longer surface residence times). Figure 5.12 shows the surface density of water transiently adsorbed to the lunar day-side at 24, 48 and 72 hours after impact, for the rough and smooth surface cases. Due to relatively short residence times over most of the day-side (except at very high solar incidence angles), surface density is a useful proxy for near-surface atmospheric density. From Figure 5.12, it can be seen that between 24-72 hours, there is a transition in the nature of the atmospheric flow. At 24 hours, the most prominent feature in the surface density maps is the high density around the South Pole; this seems to reflect the transport of water away from the antipode, which receives a relatively high influx of water due to the presence of the antipodal shock (as discussed in Chapter 4). Meanwhile, at 72 hours, atmospheric transport seems to be driven by the sublimation of night-side adsorbate, reflected in the predominantly longitudinal variation of surface density and the decrease from dawn to dusk. At 48 hours, both latitudinal and longitudinal variations in surface density (and correspondingly, in atmospheric density) are seen, indicative of flow away from both the antipode and the dawn terminator.

Comparing the smooth surface case in Figure 5.12 to the rough surface case, it can be seen that surface roughness appears to slow the rate of volatile transport over the day-side hemisphere – at all three times shown, the regional atmosphere (as reflected by surface density) has advanced slightly further from the antipode and the dawn terminator in the smooth surface case. These differences in flow patterns may partially explain the differences in cold-trapping between the rough and smooth surface cases, particularly at the North Pole. If the primary source of material cold-trapped at the North Pole is water transported from the antipode and the dawn terminator, then the slower rate of transport in the rough surface case could explain the reduced amount of cold-trapping in this case. However, the situation at the South Pole is more complicated; it is difficult to decouple the contributions of antipodal in-fall, day-side winds and sublimation at the dawn terminator to the cold-trap deposits, and thus difficult to predict and interpret the observed differences in cold-trapping – between different craters as well as between the rough and smooth surface cases.

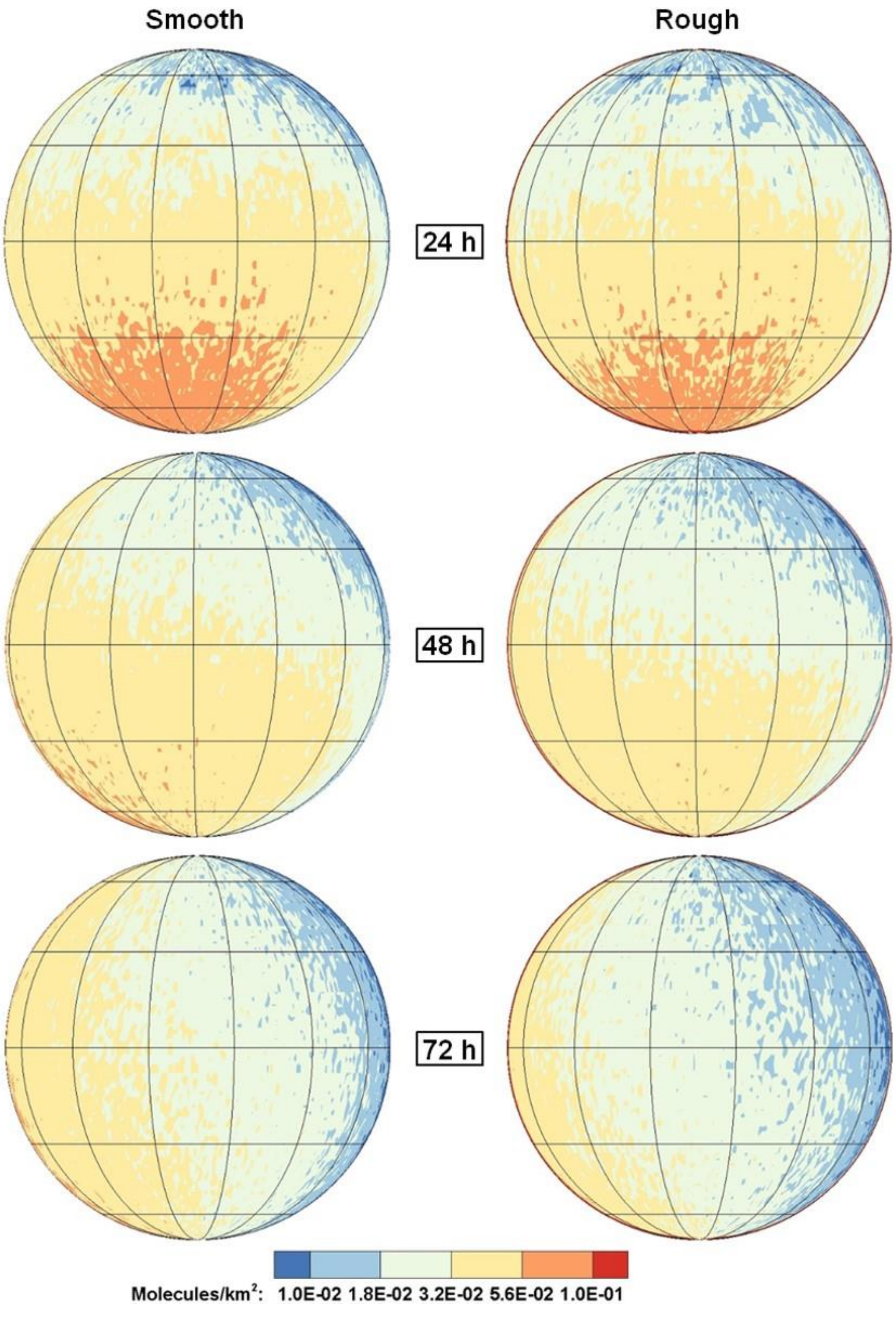

Figure 5.12: Surface density of adsorbed water molecules over the lunar day-side at 24, 48 and 72 hours after impact, from simulations of the impact-generated atmosphere with a smooth surface (left) and a rough surface (right).

Another consideration is a shift of ~4° (or ~120 km) in the effective location of the dawn terminator when surface roughness is introduced. From Figure 5.2(b), it can be seen that > 70 % of molecules that interact with this ~120 km-wide strip of the surface have residence times longer than the ballistic timescale, leading to significantly reduced mobility. This effect should reinforce the relatively low rate of cold-trapping at the high latitude North Polar cold trap in the rough surface case, and could explain why the three South Polar craters initially closest to the terminator (Shackleton, de Gerlache and Faustini) have initially lower cold-trapping rates in the rough surface case. However, despite reduced mobility near the terminator, the other three South Polar cold traps (Shoemaker, Haworth and Cabeus) have higher cold-trapping rates in the rough surface case. This is likely related to the fact that the increased 'stickiness' of the surface at high latitudes not only reduces volatile mobility at these latitudes, but also increases exospheric retention in the vicinity of the poles (this was inferred to be the reason for overall higher cold-trapping rates in the rough surface cases presented in Sections 5.3 and 5.4). In other words, the differences in cold-trapping at the six modeled South Polar craters appear to be related to two competing factors: reduced volatile mobility near the terminator in the rough surface case acts to reduce cold-trapping rates, while the corresponding increase in exospheric stability at high latitudes acts to increase cold-trapping rates. It should be noted that this section focuses on a relatively short period of time after the comet impact; the effects of the sharp gradient in volatile mobility near the terminator are likely to average out to some extent as the terminator sweeps around over the course of the several lunar day lifetime of the transient atmosphere.

5.6. SUMMARY AND CONCLUSIONS

The objective of this chapter was to investigate the influence of small-scale lunar surface roughness – represented by the stochastic rough surface temperature model developed in Section 3.4 – on volatile transport, loss and sequestration. This was achieved by first undertaking a series of collisionless Monte Carlo simulations (resembling the later stages in the lifetime of an impact-generated atmosphere), and then examining the consequences of surface roughness for volatile fallout during the collisional stages of the transient atmosphere discussed in Chapter 4.

Surface temperature affects several aspects of the gas-surface interaction, but in the context explored here, the quantity most sensitive to temperature is the surface residence time. Therefore, when implementing a rough surface temperature model, it is useful to compute a 'sticking probability', which we define as the fraction of molecules interacting with each pixel that are likely to reside on sub-pixel surfaces for timescales longer than the ballistic timescale. This sticking probability serves as a preliminary, qualitative measure of how volatile transport is affected by the introduction of surface roughness. Although roughness alters sub-pixel temperature distributions globally, sticking probabilities are significantly affected only in the vicinity of the terminator and towards the poles, where shadows become cooler and increasingly prevalent.

In general, the increasing prevalence of cool surfaces at high latitudes when a rough surface temperature model is implemented is found to lead to preferential depletion of the exosphere by cold trap capture rather than photodestruction. In particular, temporary shadows and cold slopes at the poles act as temporary reservoirs that capture and concentrate migrating molecules in the vicinity of the poles, providing more volatile material that can be mobilized and readily migrate to Permanently Shadowed Regions (PSR's) over the course of the lunar day. The distribution of temperatures introduced by a rough surface also increases the amount of thermal escape. On the Moon, the overall escape rate is still very low even when surface roughness is included, but the influence of roughness on thermal escape may be more important for surface boundary exospheres or rarefied atmospheres in environments with lower gravity or larger temperature variations.

Reinforcing the idea that volatile mobility near the poles plays an important role in cold-trapping, we observe a diurnal fluctuation in cold-trapping rates, related to the position of the dawn exospheric enhancement relative to the locations of the modeled PSR's. This trend is seen in both smooth and rough surface simulations. Though unrelated to roughness per se, it is found that the depositional fluxes at all the modeled PSR's in the collisionless Monte Carlo simulations are comparable in magnitude, without the preferential deposition at lower latitude cold traps seen by Moores (2016). This may be a result of the different initial conditions in our simulations. Ultimately, the findings of Moores also demonstrate the sensitivity of cold-trap capture to volatile mobility near the poles – which is in turn affected by roughness.

We also find that the rate and magnitude of cold-trapping and photodestruction are sensitive to the distribution of shadow temperatures, as well as to the energetics of desorption, with higher desorption energies and lower shadow temperatures slowing the rate of accumulation at the poles and prolonging the lifetime of the exosphere. This suggests that the small-scale cold traps inferred to be present on the Moon (Hayne et al.,

2013) may act to decrease the accumulation of volatiles at the larger, polar PSR's. The activation energy for desorption of water from lunar regolith is also quite likely higher than modeled here – from laboratory experiments using Apollo samples, Poston *et al.* (2015) find a distribution of activation energies about 0.5 eV (for mare soil) and 0.7 eV (for highlands soil). Here, we model only a single species (H_2O), but accounting for surface roughness in exospheric modeling becomes more important when considering species with higher activation energies for desorption from the surface of interest.

Insofar as exospheric structure is concerned, accounting for surface roughness results in a reduced and broadened peak in column density at the dawn terminator, most clearly apparent at equatorial latitudes. In the collisionless Monte Carlo simulations, exospheric density is found to be greater at higher latitudes, and this enhancement in column density is more pronounced when surface roughness is modeled.

In the short-term aftermath of a comet impact, the role that surface roughness plays in determining the fate of volatiles is more complex. At this stage, much of the impact-generated vapor has yet to interact with the surface and thus, the overall rates of escape and photodestruction are hardly affected by the inclusion of roughness in the surface thermal model. However, a comparison of cold-trapping rates at different PSR's in simulations with and without surface roughness yields some interesting insights. Surface roughness slows the rate of migration over the day-side hemisphere, and leads to both reduced volatile mobility and increased exospheric density at high solar incidence angles. These factors, combined with the non-uniform nature of the transient atmosphere at this stage, are reflected in differences in cold-trapping between the modeled PSR's.

Chapter 6: Radiative Heat Transfer in an Unsteady, Rarefied Atmosphere

6.1. CHAPTER OVERVIEW

This chapter focuses on radiative heat transfer in the impact-generated atmosphere. Section 6.2 discusses the validation of the method developed in Chapter 3 (Section 3.5) for radiative heat transfer in an unsteady, rarefied atmosphere, through a series of relatively simple test cases. Section 6.3 deals with the application of this method to the DSMC simulations of the impact-generated atmosphere and discusses the influence of radiative heat transfer on atmospheric structure and the resulting volatile fallout.

6.2. CODE VALIDATION TESTS

As outlined in Chapter 3 (Section 3.5), there are three aspects to the problem of radiative heat transfer in an impact-generated atmosphere: (i) the attenuation and reabsorption of spontaneously emitted molecular radiation; (ii) the attenuation and absorption of radiation from the lunar surface; and (iii) the attenuation and absorption of solar radiation. (As mentioned in Chapter 3, scattering is not modeled.) Each of these aspects is implemented as an independent sub-routine in the main DSMC code, and can therefore be validated independently. (It is also difficult to formulate a single test case that can simultaneously validate all three sub-routines.) Sections 6.2.1, 6.2.2 and 6.2.3 discuss the validation of the sub-routines that compute the net rate of atmospheric heating or cooling due to mechanisms (i), (ii) and (iii), respectively. Another aspect of the code that requires validation is the coupling of the computed heating/cooling rates to unsteady gas dynamics (described in Section 3.5.1), which is implemented through a series of other sub-routines. The validation of this approach is discussed in Section 6.2.4. It should be noted that unless otherwise specified, “gas” in this section refers to water vapor.

6.2.1. Attenuation & Reabsorption of Spontaneously Emitted Molecular Radiation

The sub-routine that deals with the attenuation and reabsorption of spontaneously emitted molecular radiation involves several steps, summarized below:

1. The total energy emitted within each computational cell is calculated.
2. This energy is divided among a specified number of energy packets.
3. Each energy packet is propagated through the computational domain.
4. Computational cells absorb energy (based on cell properties and propagation path length) and energy packets are attenuated accordingly.

The outputs of this sub-routine are the energy absorbed by each computational cell i originating from all other cells $j \neq i$, $\epsilon_{abs,j \rightarrow i}$ (in W), and an opacity factor, f_i, defined as the fraction of energy emitted within a computational cell that is reabsorbed in that cell. Ideally, f_i should be $\ll 1$ for a well-resolved calculation, although in practice this may not always be possible – particularly when the computational domain is very large or gas density is very high – since grid resolution is constrained by available memory.

Step 1 in the list above is based on published line strengths (from the HITRAN database) and well-established theoretical formulations. The rate of energy emission as a function of temperature computed using this approach is generally consistent with previous literature (as shown in Figure 3.7). This leaves the validation of the propagation and absorption steps. As a first, basic check, I verified that the conservation of energy was satisfied for the computational domain; i.e. all the energy emitted within the domain was either absorbed within the domain or crossed the domain boundaries. Additionally, in the optically transparent and opaque limits, all the energy emitted within the domain was verified to leave the domain or be absorbed, respectively.

For a more quantitative check, we can approximate the cell opacity factor analytically, as follows. Consider the propagation of a packet p with initial energy $\epsilon_{0,p}$ through a cell i with uniform number density n and absorption cross-section k. If the packet travels some distance L_p (based on its initial position and direction of propagation) before leaving the cell, the amount of energy absorbed from packet p by cell i is given by:

$$\epsilon_{abs,p\to i} = \epsilon_{0,p}[1 - \exp(-nL_pk)] \tag{6.1}$$

If the medium is optically thin ($nL_pk \ll 1$), $\epsilon_{abs,p\to i}$ can be approximated as:

$$\epsilon_{abs,p\to i} \approx \epsilon_{0,p}nL_pk \tag{6.2}$$

Considering some large number of N packets with the same initial energy ϵ_0, but different initial positions within the cell and different directions of propagation, we can obtain the total energy absorbed by cell i from all packets released within that cell:

$$\epsilon_{abs,i\to i} = \sum_{p=1}^{N} \epsilon_{abs,p\to i} \approx \epsilon_0 nk \sum_{p=1}^{N} L_p \tag{6.3}$$

Per definition, the opacity factor f_i can then be found as follows:

$$f_i \equiv \epsilon_{abs,i\to i}/N\epsilon_0 \approx nk\left(\sum_{p=1}^{N} L_p/N\right) = nkL_m \tag{6.4}$$

The "mean path length" L_m defined by Eq. (6.4) depends solely on the cell geometry, and can be obtained numerically by summation or sampling over all possible path lengths; i.e. by calculating and averaging distances to the cell boundaries from a sufficiently large number of points in the cell interior, and along a sufficiently large number of directions (assumed to be uniformly and isotropically distributed, respectively). For a cubical cell, it can be found that $L_m \approx 0.45L$ where L is the length of any edge of the cube.

Thus, the propagation and absorption steps in the calculation of radiative heating/cooling due to spontaneously emitted molecular radiation can be validated by comparing the values of f_i obtained from the relevant sub-routine to independently computed values of f_i from Eq. (6.4). In order to carry out this test, the Cartesian grid used for the radiative heat transfer calculation was filled with a uniform gas at temperature $T = 300$ K and number density $n = 10^8$ m^{-3}. The grid was divided into 200 cells in each dimension – each cell being a cube with 19.38 km edges. As mentioned in Chapter 3, each of the 212 modeled spectral lines is divided into three wave-number bins and three energy packets are emitted per bin (i.e. nine packets per line). The absorption cross-section k associated with each line is a function of temperature, and each energy packet is tracked until its energy drops below a threshold value of 10^{-7} W (the average initial energy of a packet is O(10^{-3}) W). From Figure 6.1, it can be seen that the computed average values of cell opacity (f_i) for each spectral line agree well with the corresponding values estimated from Eq. (6.4), using a mean path length $L_m = 0.45L$. Also shown are average values of cell opacity obtained at a lower temperature ($T = 200$ K, corresponding to a larger range of absorption cross-sections), a higher number density ($n = 10^{12}$ m^{-3}) and a smaller number of cells (both of which increase the optical depth of each cell), and a higher number of packets per bin and a higher value of threshold energy (which increase and decrease, respectively, the accuracy of the calculation). It should be noted that although the computed *average* cell opacities agree well with the theoretical value for all six of these cases, individual cell opacities show more variation. Both the accuracy and expense of the calculation increase with the number of simulated energy packets.

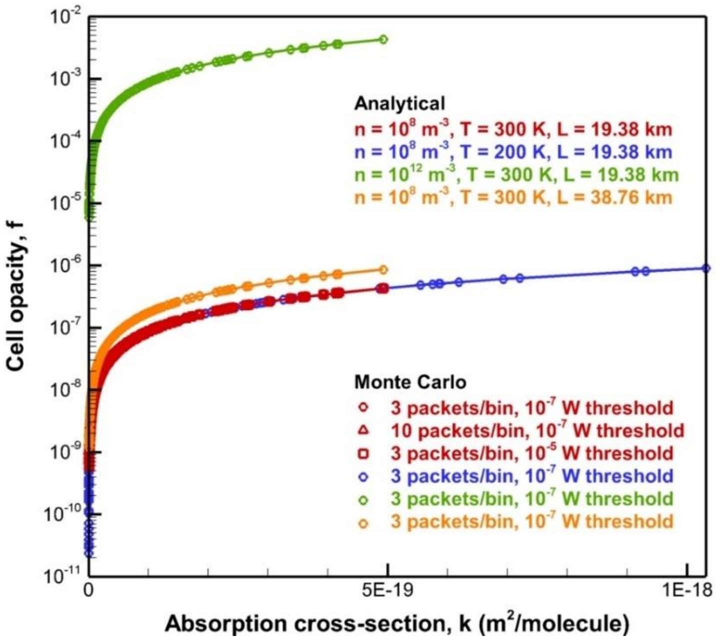

Figure 6.1: Average opacity of cubical cells filled with a uniform absorbing gas as a function of molecular absorption cross-section, obtained through Monte Carlo modeling (symbols), and compared against analytically estimated values (solid lines) from Eq. (6.4). The symbols correspond to the 212 spectral lines considered.

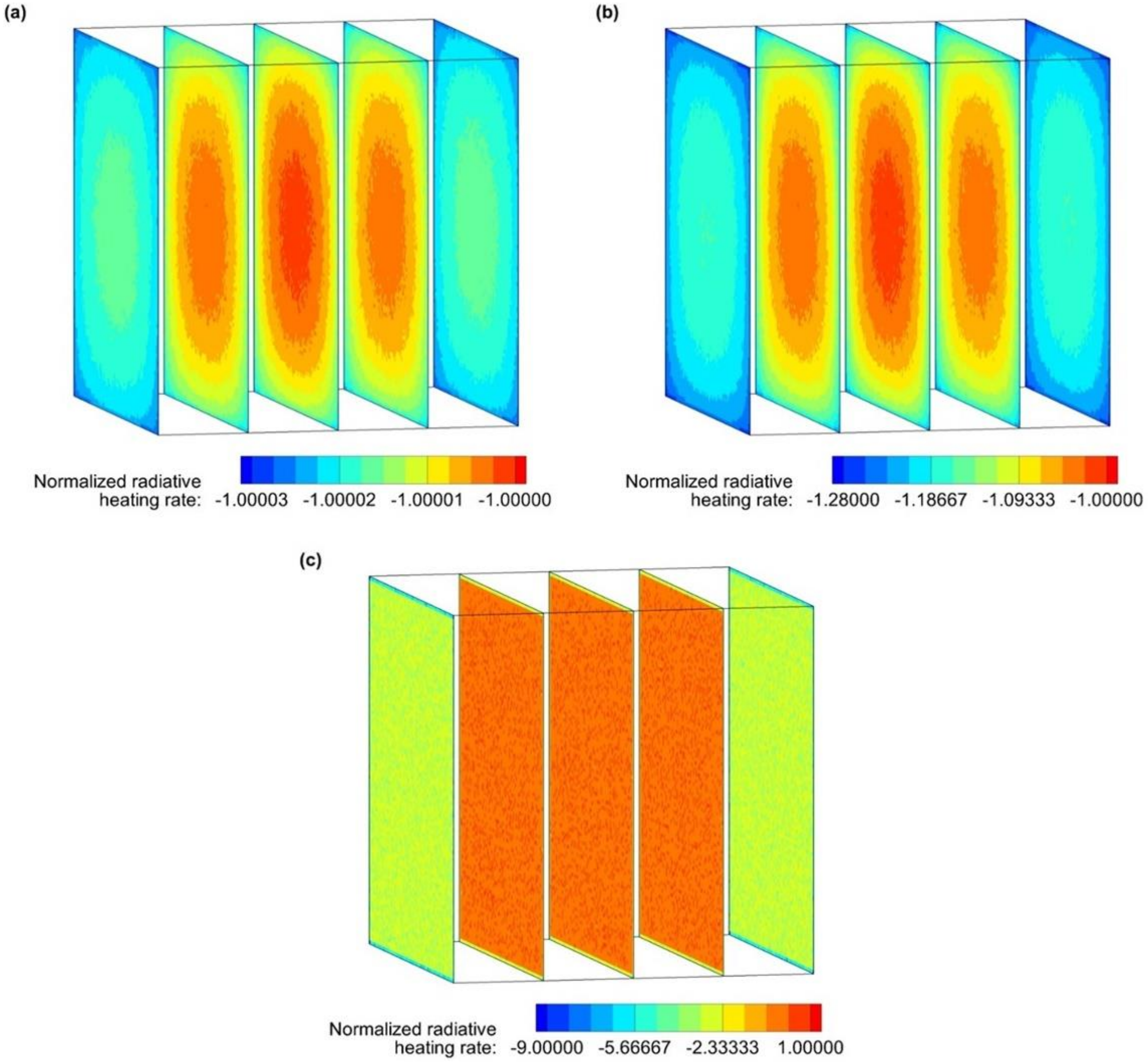

Figure 6.2: Radiative heat transfer rates (due to emission and reabsorption of molecular radiation) in a cube filled with a uniform gas at 300 K and number densities (a) 10^8 m^{-3}, (b) 10^{12} m^{-3}, and (c) 10^{16} m^{-3}. Rate magnitudes are normalized separately for each plot. Positive and negative values represent net heating and cooling of a cell, respectively. Note the different color scale for each plot.

Figure 6.2 provides a qualitative picture of how the attenuation and reabsorption of molecular radiation affect radiative heat transfer. Figures 6.2(a) to (c) show normalized radiative heating/cooling rates in a cubical region of space, surrounded by vacuum, filled with a uniform gas at 300 K and number densities of 10^8, 10^{12} and 10^{16} m^{-3}, respectively. In the n = 10^8 m^{-3} case, the gas is almost transparent – there is very little difference between the cooling rates at the center and periphery of the cube, although the rate of cooling is marginally faster at the periphery. Cooling rates in the n = 10^{12} m^{-3} case are qualitatively similar, with the periphery of the cube cooling faster than the center. However, in this case, the higher gas density allows for more effective trapping of radiation, such that the center of the cube cools appreciably more slowly. Lastly, in the n = 10^{16} m^{-3} case, the radiation field is qualitatively different since at this density, the gas is no longer optically thin. Spontaneously emitted radiation is readily reabsorbed and the cooling rate is significant only at the periphery of the cube; in the interior, the net rate of heating/cooling is quite low, with some Monte Carlo noise.

6.2.2. Radiation from the Lunar Surface

The main difference between the subroutines that handle gas-to-gas radiation and surface-to-gas radiation is the manner in which energy packets are initialized. In the former case, packets are initialized within Cartesian cells and propagate in all directions, while in the latter case, packets are initialized on a spherical surface and propagate away from the surface. Since the absorption of energy packets is implemented similarly in both cases, this section focuses on validating the initialization/propagation steps of the subroutine dealing with radiation from the lunar surface.

In the absence of an absorbing/emitting medium, the radiation field around a body with a known surface temperature distribution can be computed analytically or numerically. In the basic case of a spherical, isothermal black body of radius R and temperature T, the flux F (in W/m^2) at a radial distance d from the center of the sphere is simply given by:

$$F = \sigma T^4 R^2/d^2 \tag{6.5}$$

F can also be computed using the photon Monte Carlo method. The radiation field shown in Figure 6.3 was obtained using the lunar surface radiation subroutine with the lunar surface temperature set to T = 300 K. It can be seen that the analytical and Monte Carlo results are in close agreement for this simple test case.

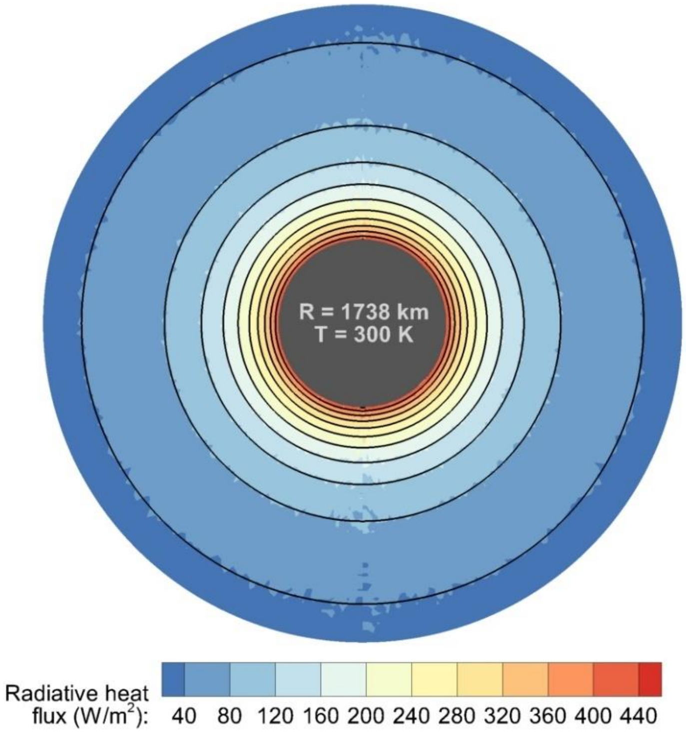

Figure 6.3: Radiative heat flux around an isothermal, spherical black body of radius R = 1738 km (= R_{Moon}) at temperature T = 300 K. Lines indicate analytical values computed at 40 W/m^2 intervals using Eq. (6.5) and colors indicate the Monte Carlo solution.

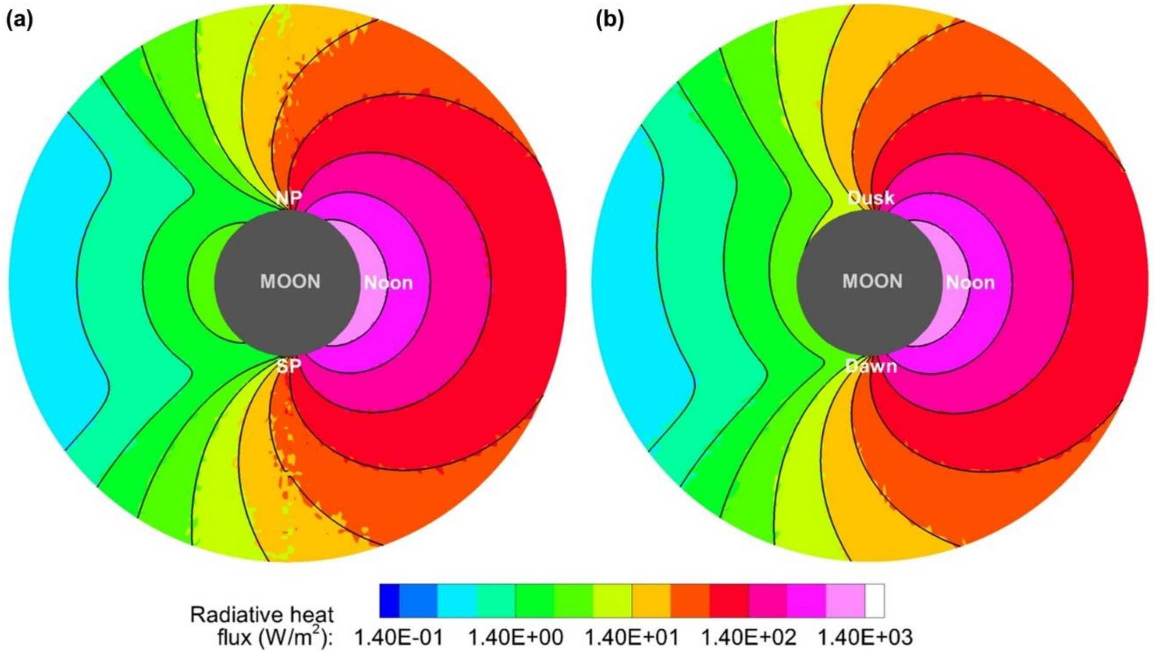

Figure 6.4: Radiative heat flux around the Moon in (a) a plane passing though the poles and the sub-solar point, and (b) the equatorial plane. Lines indicate the numerical solution computed using Eq. (6.6) and colors indicate the Monte Carlo solution. The lunar surface is assumed to be black with a temperature distribution given by Eq. (3.7).

A more interesting test is to check whether the lunar surface radiation subroutine can reproduce the radiation field around the Moon with a more realistic surface temperature distribution. For comparison, a numerical solution for the radiation field can be obtained as follows. Let us discretize the region of space around the Moon into spherical cells defined by coordinates (r, θ, φ) for $\theta = 0$ to π and $\varphi = 0$ to 2π. Assuming black body emission from the lunar surface, the rate of radiative energy transfer from a surface cell (R, θ_s, φ_s) with surface area dA_s at temperature T_s to a differential surface of area dA located at a distance d (where $d > R$) is given by:

$$dE = \left(\sigma {T_s}^4/\pi\right)(dA_s cos\alpha_s)(dA cos\alpha)/d^2 \tag{6.6}$$

where α and α_s are the angles between surface normals $\overrightarrow{dA}$ and $\overrightarrow{dA_s}$, respectively, and the line (of length d) connecting the two surface elements.

Figure 6.4 shows the radiative flux (dE/dA) around the Moon computed using Eq. (6.6) and the Monte Carlo method, with T_s specified according to Eq. (3.7). Once again, the Monte Carlo results agree very well with the numerical solution.

6.2.3. Attenuation & Absorption of Solar Radiation

The subroutine that handles the absorption and attenuation of solar radiation is perhaps the simplest part of the radiative heat transfer implementation. As mentioned in Section 3.5.4, solar radiation can be modeled as a parallel beam of energy packets of various frequencies; the attenuation of this beam can be computed numerically, without the need for a Monte Carlo method. For validation of this segment of the code, I considered the Cartesian computational grid (1938 km in size with 200 cells in each dimension) to be filled with a uniform gas at 300 K and number densities of $n = 10^8$ m^{-3} and 10^{12} m^{-3}. The energy absorbed by the N^{th} computational cell in a column (where $N = 1$ is the cell closest to the Sun) is given by:

$$\epsilon_{abs,N} = \sum_i \epsilon_{i,N} \left[1 - \exp\left(-nLk_{avg}(\omega_{0,i})\right)\right] \tag{6.7}$$

where $\epsilon_{i,N} = \epsilon_{i,N-1} \exp\left(-nLk_{avg}(\omega_{0,i})\right)$ for $N > 1$, and $\epsilon_{i,1} = \epsilon_{i,0}$

Here, $i = 1, 2, \ldots, 212$ denotes the line centered at $\omega_{0,i}$ and $k_{avg}(\omega_{0,i})$ is the profile-averaged absorption cross-section for that line, from Eq. (3.25). $\epsilon_{0,i}$ is the unattenuated energy in the range $\omega_{0,i} \pm 3\gamma_{D,ref}$, of which an amount $\epsilon_{N,i}$ enters the N^{th} cell.

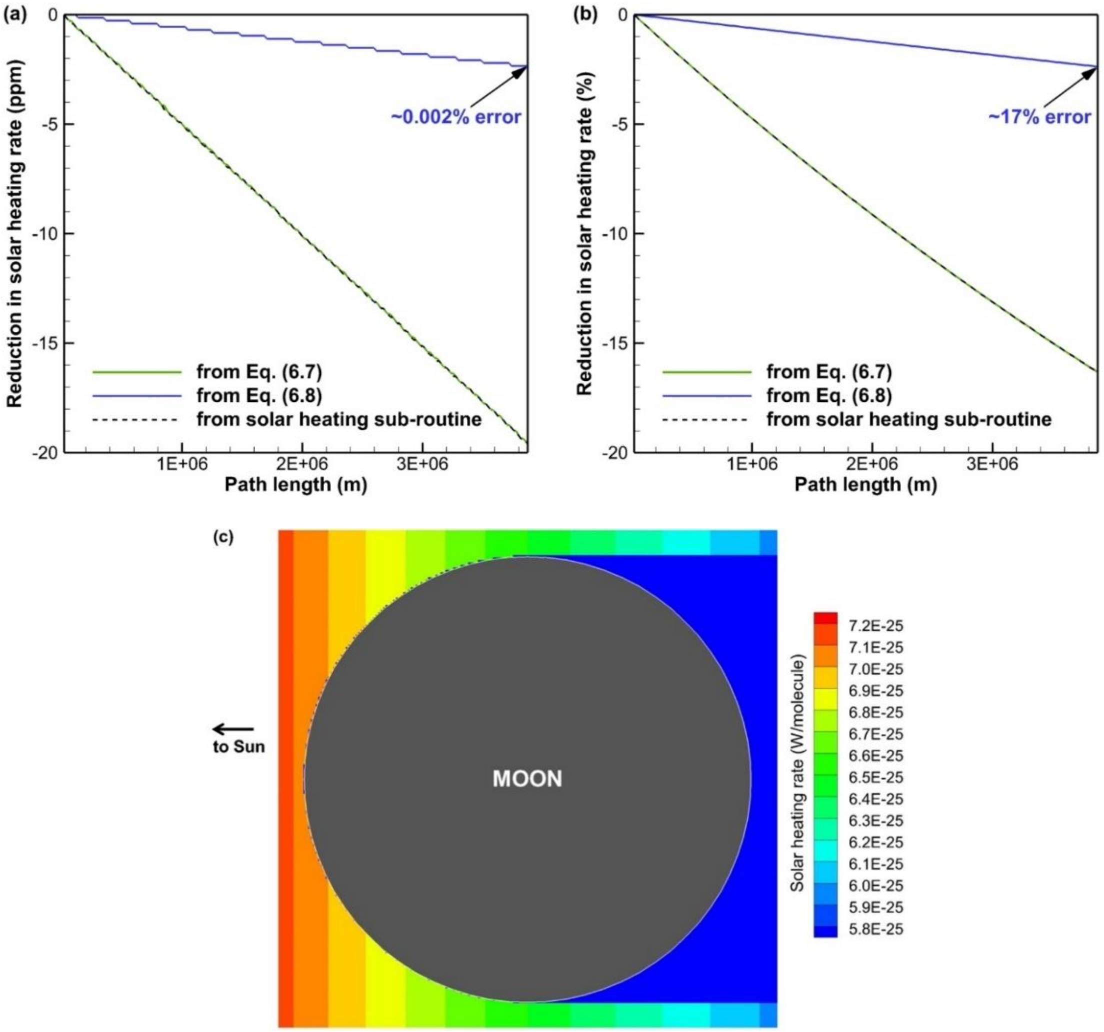

Figure 6.5: Reduction in solar heating rate due to the attenuation of sunlight passing through a uniform gas at 300 K for number densities of (a) 10^{8} m^{-3} and (b) 10^{12} m^{-3}, shown as a function of path length traveled through the gas. Note the different y-axis units in (a) vs. (b). The output of the solar heating sub-routine is compared to independent calculations using Eq. (6.7) and Eq. (6.8). Figure (c) is another view of the output of the solar heating sub-routine for the $n = 10^{12}$ m^{-3} case, illustrating the attenuation of sunlight by the medium, and the shadow cast by the Moon.

Figures 6.5(a) and (b) show the reduction in solar heating rate with path length traveled through the computational domain. Figure 6.5(c) is a two-dimensional view of solar heating rates in the $n = 10^{12}$ m^{-3} case, illustrating the attenuation of sunlight by the absorbing medium and the shadow cast by the Moon. Figures 6.5(a) and (b) show that the output of the solar heating subroutine closely matches values computed using Eq. (6.7). Also shown for reference is the heating rate computed using a weighted sum of line profile-averaged absorption cross-sections, k_{total} – this approximation simplifies the calculation by eliminating the summation over multiple lines in Eq. (6.7). In this case, the energy absorbed by the N^{th} computational cell in a column is given by:

$$\epsilon_{abs,N} = \epsilon_{total,N}[1 - \exp(-nLk_{total})] \tag{6.8}$$

where $\epsilon_{total,N} = \epsilon_{total,N-1}\exp(-nLk_{total})$ for $N > 1$, and $\epsilon_{total,1} = \sum_i \epsilon_{i,0}$

and $k_{total} = \sum_i \epsilon_{i,0} k_{avg}(\omega_{0,i}) \,/ \sum_i \epsilon_{i,0}$

It can be seen that Eq. (6.8) yields values of $\epsilon_{abs,N}$ that are close to those obtained through Eq. (6.7) in the low density case, but more significant errors are seen in the high density case. In both cases, the error increases as energy is propagated through the domain.

6.2.4. Coupling Radiative Heat Transfer and DSMC Gas Dynamics

The final aspect of the DSMC code that requires validation is the coupling of the radiative heat transfer subroutines to the rest of the code. The subroutines discussed in Sections 6.2.1 to 6.2.3 compute instantaneous rates of radiative heating/cooling. The resulting evolution of the flow field is modeled separately, as discussed in Section 3.5.1. The actual quantity that is modified is the rotational energy of molecules (characterized by a rotational temperature), which may be transferred to translational modes through collisions; at equilibrium, the translational and rotational temperatures are the same.

A series of test cases was conducted to verify that the computed rates of radiative heating/cooling are correctly reflected in the thermal evolution of the flow field. In these test cases, the DSMC domain was filled with a stationary, uniform gas at a specified number density and an initial temperature of 20 K. (The relatively low initial temperature was chosen to ensure that the initial rotational cooling rate could be resolved by the DSMC time-step.) For validation purposes, the radiative heating rate was fixed at a value of 2.522167×10^{-25} W/molecule, approximately equal to the unattenuated solar heating rate corresponding to the initial gas temperature. The rate of radiative cooling due to spontaneous emission was allowed to vary with gas temperature (as in Figure 3.7), assuming the gas to be transparent i.e. neglecting reabsorption of radiation. If the gas is sufficiently collisional, the net change in internal energy is redistributed equally among three rotational modes and three translational modes, according to the equipartition theorem, such that the energy possessed by each mode is equal to $\frac{1}{2} k_B T$. Thus, the change in temperature of the gas, ΔT, during a time-step of size Δt is given by:

$$3k_B \Delta T = (\partial \overline{e_{rot}}/\partial t)\Delta t \tag{6.9}$$

where $\partial \overline{e_{rot}}/\partial t$ is the net rate of change of average molecular rotational energy, i.e. the net rate of radiative heat transfer. If collisions are insufficient to transmit any changes in rotational energy to the translational modes, the translational temperature should not change. The rate of change of rotational temperature in this case, ΔT_{rot} is given by:

$$\frac{3}{2} k_B \Delta T_{rot} = (\partial \overline{e_{rot}}/\partial t)\Delta t \tag{6.10}$$

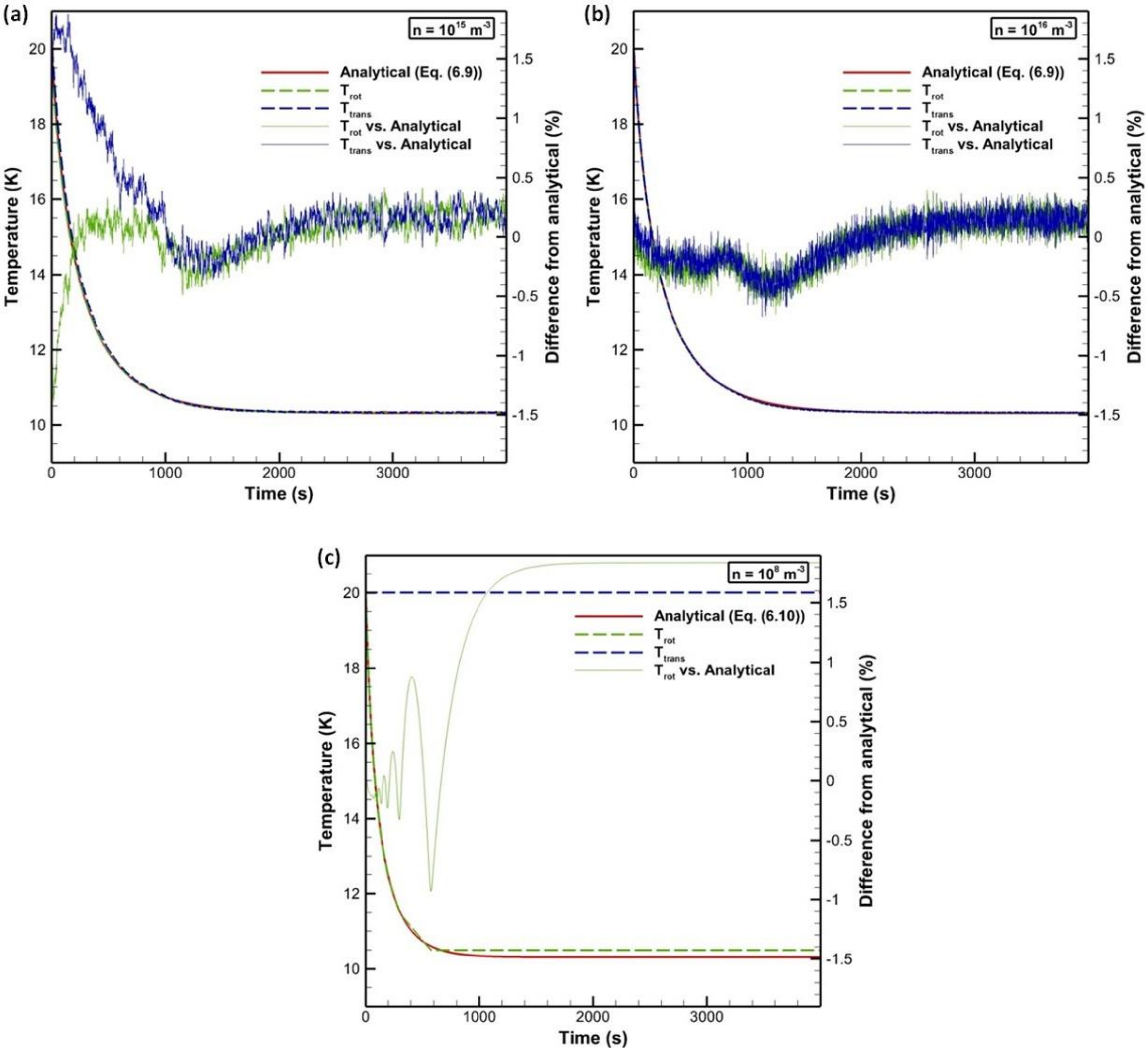

Figure 6.6: Evolution of the temperature(s) of a stationary gas from an initial temperature of 20 K, for number densities of (a) 10^{15} m^{-3}, (b) 10^{16} m^{-3} and (c) 10^{8} m^{-3}. Rotational and translational temperatures obtained from the DSMC simulation are compared to values obtained using Eq. (6.9) (for (a) and (b)) and Eq. (6.10) (for (c)).

The evolution of temperature computed using Eq. (6.9) or Eq. (6.10) can be compared to the evolution of translational and rotational temperatures in the DSMC simulation, as shown in Figure 6.6 for a few different number densities. To minimize noise, the DMSC temperatures are averaged over 1320 cells, each ~2° × 2° × 10 km in size and containing O(100) molecules. The time-step size is 1 s. In all modeled cases, the steady-state DSMC temperatures agree with the analytical value(s) to within a few percent. In the lowest density case (Figure 6.6(c)), the gas is virtually collisionless and only the rotational temperature evolves. The unrealistically sharp changes in rotational temperature at ~300 s and ~500 s in this case are due to the fact that the code rounds temperatures to the nearest integer values to reduce computational costs when computing rotational cooling rates. In the more collisional, higher density cases, these abrupt changes in rotational temperature are "softened" by collisions. As density increases and the gas becomes more collisional (Figure 6.6(a) and (b)), translational and rotational temperatures are in closer agreement with each other. This reflects the fact that the analytical solution assumes instantaneous redistribution of internal energy among rotational and translational modes, whereas in reality the speed of redistribution is limited by the collision frequency, which is directly proportional to number density for a given temperature and is O(0.1) collisions per unit time in the $n = 10^{15}$ m^{-3} case.

6.3. IMPLICATIONS FOR AN IMPACT-GENERATED ATMOSPHERE

This section discusses the application of the radiative heat transfer method developed in Chapter 3 and validated through the test cases presented in Section 6.2 in the context of the impact-generated atmosphere, focusing on the short-term, collisional stages of post-impact atmospheric evolution discussed in Chapter 4. Given the scope of this dissertation, the key question of interest is how the inclusion of radiative transfer affects the structure of the impact-generated atmosphere and the associated transport, loss and deposition of volatiles. The influence of radiative heat transfer on the temperature field is also of interest due to the implications this may have for phase changes (e.g. could impact-generated water vapor condense and precipitate?) and for post-impact chemistry (since reaction rates are sensitive to temperature).

This section compares two simulations – the first adopts a simplified treatment of radiative heat transfer in which radiation from the lunar surface, reabsorption of spontaneously emitted radiation and attenuation of solar radiation are not included, and the second uses the comprehensive model developed in Chapter 3 (with all the previously neglected factors included). The radiative heat transfer model used in the first simulation resembles that used for the simulations in Chapter 4, but with some updates, viz., radiative cooling is computed on a line-by-line basis rather than through an analytical expression, and solar heating is temperature-dependent (computed as in Section 3.5.4, but without attenuation) rather than being assumed constant.

For computational ease, both simulations begin at 1 hour after impact; i.e., the baseline simulation presented in Chapter 4 is paused at 1 hour after impact and then resumed using the radiative transfer models discussed above. The difficulty in applying the radiative heat transfer models at earlier times lies in the rapid expansion of the vapor cloud during the first hour after impact. To accurately compute radiative heating/cooling rates during the rapid expansion stage, the subroutines discussed in Section 6.2 must be called at more frequent intervals, adding to computational costs. After the first hour or so, atmospheric structure evolves more slowly and less frequent calls suffice. This approach may lead to a substantial overestimation of radiative cooling at early times, since we do not account for the trapping of radiation in the dense vapor cloud until 1 hour after impact. Thus, the results presented in this chapter probably underestimate the temperature of the flow field. Nonetheless, the two simulations discussed above should serve to provide a general assessment of the significance of radiative transfer.

It should also be noted that, as in Stewart (2010), the simulations do not model vapor that leaves the third domain (of four staged computational domains) at speeds above escape velocity. While escaping vapor cannot reach cold traps, neglecting this material also means neglecting its radiative influence. The escaping component accounts for a significant proportion of total mass of vapor generated, but it is also widely dispersed, and is likely to be cold and rarefied. As a result, the escaping vapor is unlikely to play a major role in attenuating or trapping solar or spontaneously emitted radiation. However, it may be worthwhile to consider this issue in more detail in future work.

As mentioned in Chapter 3, radiative heating and cooling rates are computed on a Cartesian grid. For the simulations in this chapter, the grid extended out to ± 37,000 km from the center of the Moon with 200 cells in each dimension. To resolve the shock structures in the vicinity of the Moon, the grid cells were non-uniform in size, with 100 cells (in each dimension) concentrated between ± 10,000 km and the remaining 100 distributed between ± 10,000 km and ± 37,000 km, corresponding to minimum and maximum cell dimensions of 200 km and 540 km, respectively. (Specifying smaller cells in the vicinity of the Moon would more accurately resolve flow features, but also leads to statistical issues, as discussed in Section 3.5.5.) For the Monte Carlo calculations, each of the 212 Doppler-broadened lines considered was divided into three wavenumber bins, and three energy packets were tracked in each bin. The threshold power (below which the propagation of energy packets is terminated) was set to 10^{-7} W. The DSMC simulations were run out to 6 hours after impact, with the ratio of real molecules to simulated molecules set to 1.25×10^{29} between 1-3 hours and 6.25×10^{28} between 3-6 hours.

Figures 6.7, 6.8 and 6.9 show the evolution of rotational and translational temperature and number density, respectively, between 1-3 hours after impact for the two sets of simulations. Note that there are some artefacts, particularly in the density contours, due to the interpolation of properties from the spherical DSMC grid to the Cartesian grid used for the radiative transfer calculations. The apparent absence of molecules along the North Polar axis is due to the fact that DSMC cells here are smaller and contain relatively few molecules. It can be seen from Figures 6.7 and 6.8 that the vapor cloud cools faster when the impact-generated atmosphere is treated as transparent, implying that the reduced rate of cooling due to trapping (i.e. reabsorption) of spontaneously emitted radiation in locally optically thick regions of the vapor cloud more than compensates for reduced solar heating due to self-shielding. The more comprehensive model also includes an additional heat source in the form of radiation from the lunar surface. Since the vapor is largely collisional at this stage, translational and rotational temperatures are in close agreement except at the fringes of the expanding cloud, where the gas approaches the collisionless limit. Below the shock, the gas is sufficiently dense that the vapor remains relatively warm (~300 K). In both sets of simulations, the far-field temperature is very cold, even lower than the equilibrium temperature of ~10 K achieved in test cases presented in Figure 6.6, which involved a nominally transparent gas. The likely reason for this is that in the impact-generated atmosphere simulations, the vapor cools through expansion as well as through radiation.

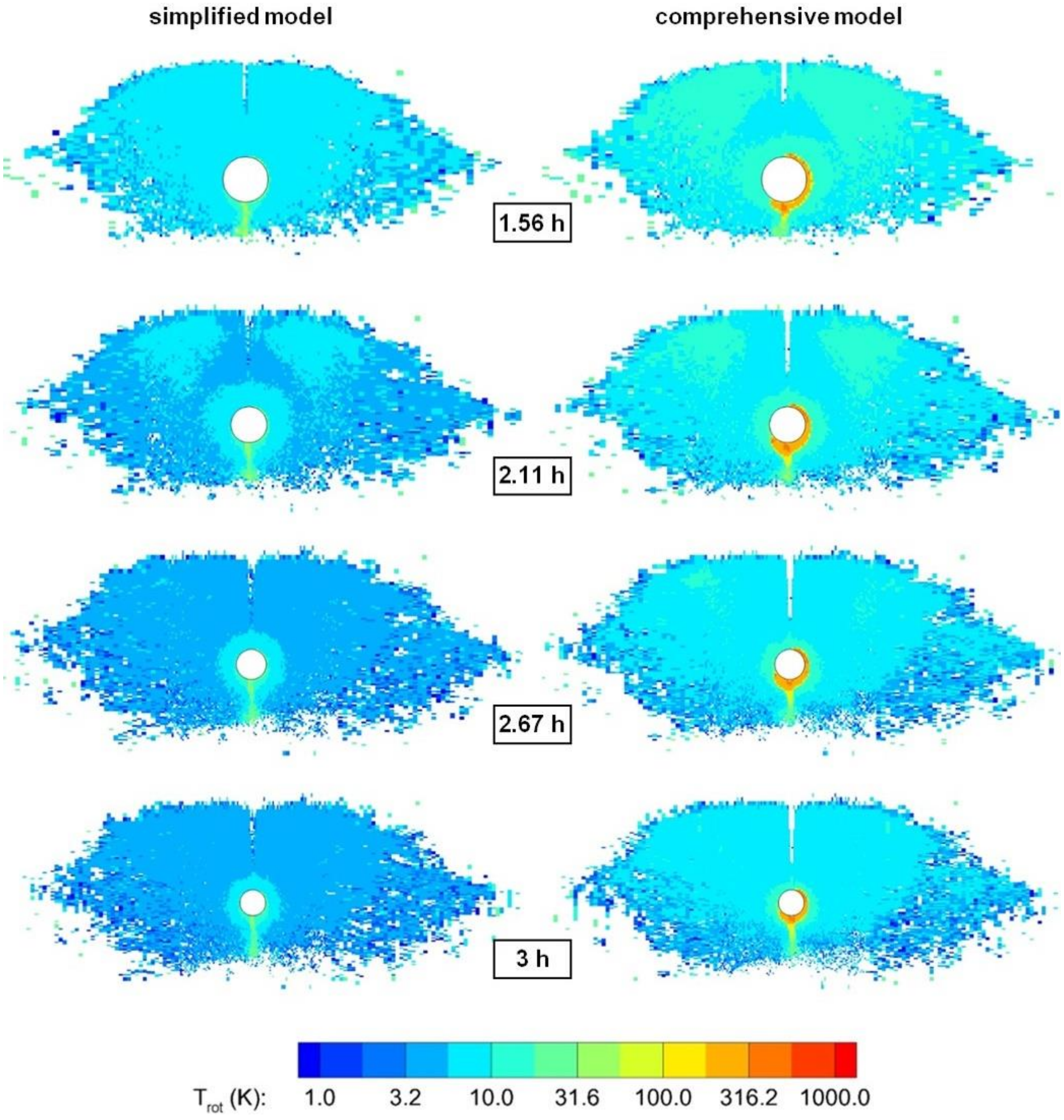

Figure 6.7: Comparison of the evolution of rotational temperature between 1-3 hours after impact in simulations adopting simplified and comprehensive models for radiative heat transfer. Temperature is sampled on the Cartesian grid used for the radiative transfer calculations and the views shown are in the plane of impact. The Sun is to the right.

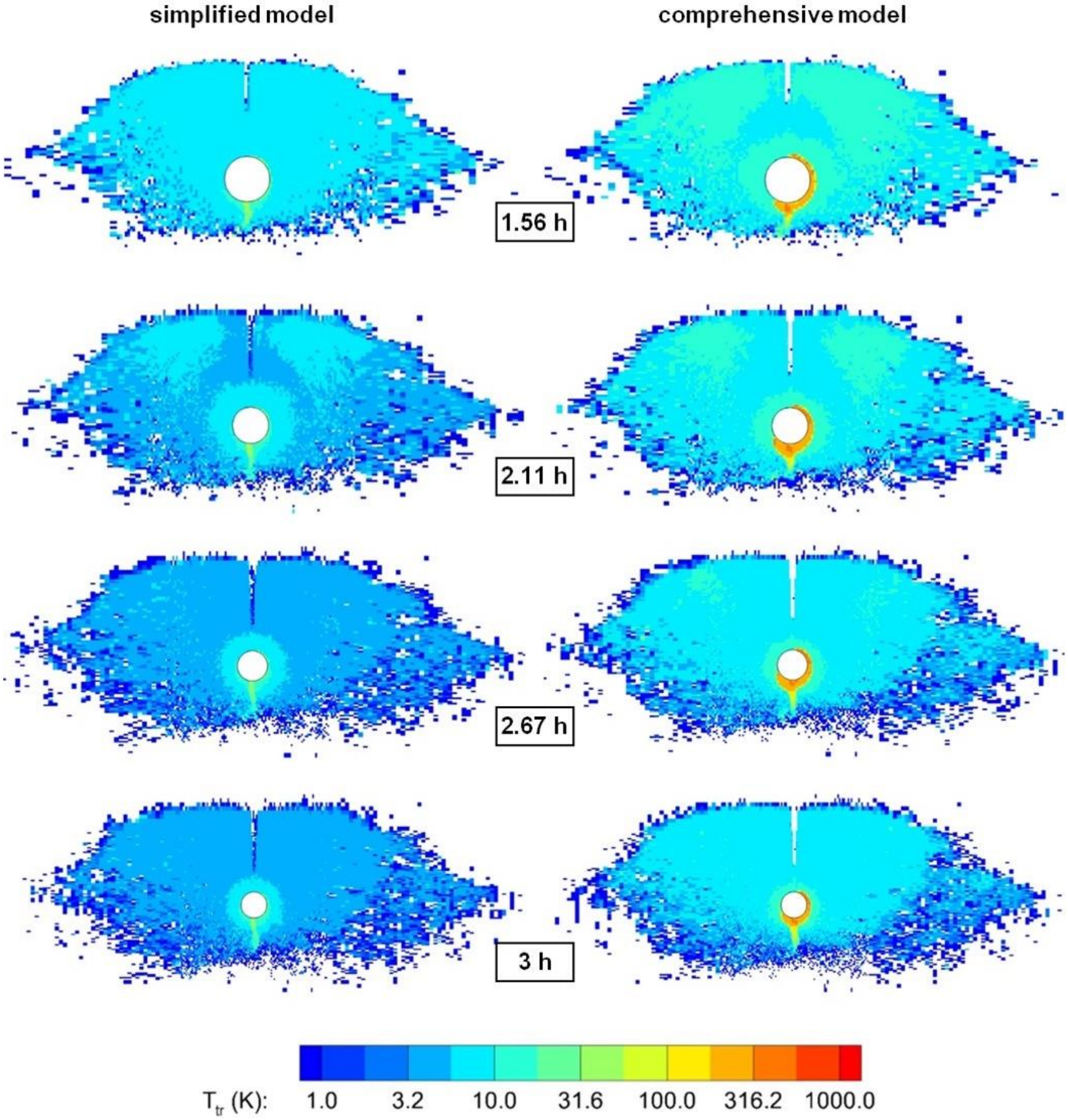

Figure 6.8: Comparison of the evolution of translational temperature between 1-3 hours after impact in simulations adopting simplified and comprehensive models for radiative heat transfer. Temperature is sampled on the Cartesian grid used for the radiative transfer calculations and the views shown are in the plane of impact. The Sun is to the right.

Accounting for the trapping of radiation also results in a qualitative change in atmospheric structure near the surface, reflected in both the temperature and density contours. Since the vapor retains more of its initial thermal energy, the antipodal and day-side shocks are more diffuse.

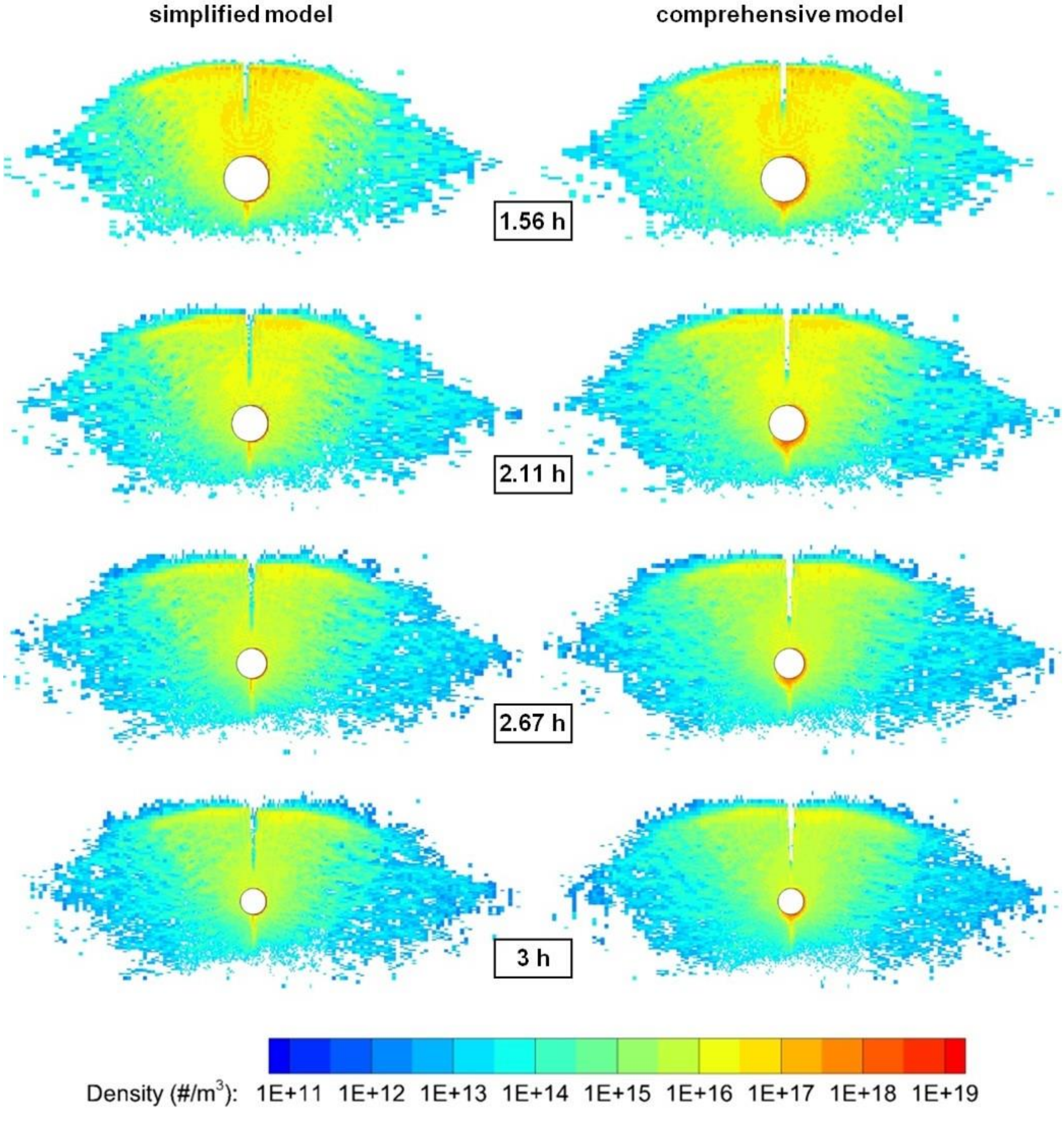

Figure 6.9: Comparison of the evolution of number density between 1-3 hours after impact in simulations adopting simplified and comprehensive models for radiative heat transfer. Density is sampled on the Cartesian grid used for the radiative transfer calculations and the views shown are in the plane of impact. The Sun is to the right.

Figure 6.10 compares near-field density and velocity vectors in the two modeled cases. It can be seen that with the more comprehensive radiative heat transfer model, the turning of the infalling gas to flow parallel to the surface occurs at a higher altitude, and the flow retains more of its pre-shock momentum (reflected in the more gradual turning of the streamlines). As a result, the day side winds travel further across to the night side.

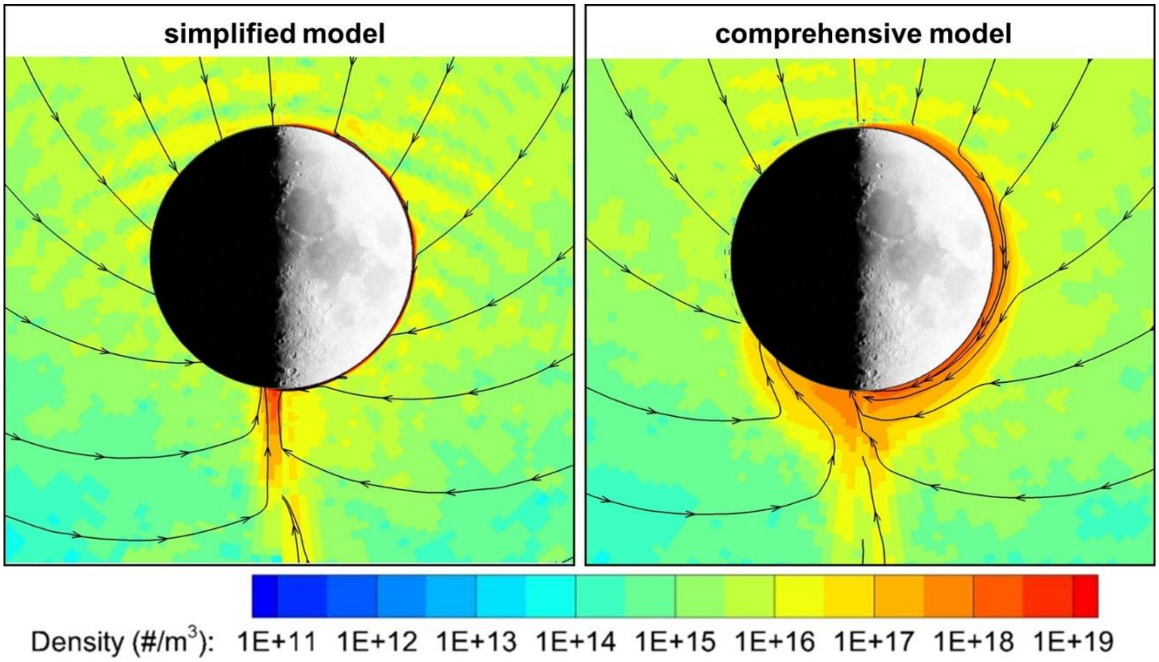

Figure 6.10: Near-field gas number density and streamlines at 3 hours after impact in simulations adopting simplified and comprehensive models for radiative heat transfer (see text for details). Density and velocity are sampled on the spherical grid used for the DSMC simulation. The image of the lunar surface is included only to illustrate the day and night sides, and does not depict actual topography included in the model. The views shown are in the plane of impact, and the Sun is to the right.

Figures 6.11 and 6.12 illustrate the relative importance of the various modeled mechanisms of radiative heating/cooling. As seen in Figure 6.11(a), solar radiation is attenuated as it passes through the absorbing water vapor atmosphere; regions close to the day-side surface and behind the antipodal shock are effectively shielded from solar heating by the strongly absorbing (i.e. relatively dense and warm) regions that lie sunward. Due to the dependence of absorption on both density and temperature, warm inner regions of the atmosphere are heated more strongly than cold outer regions, despite the reduced intensity of sunlight reaching the interior of the vapor cloud.

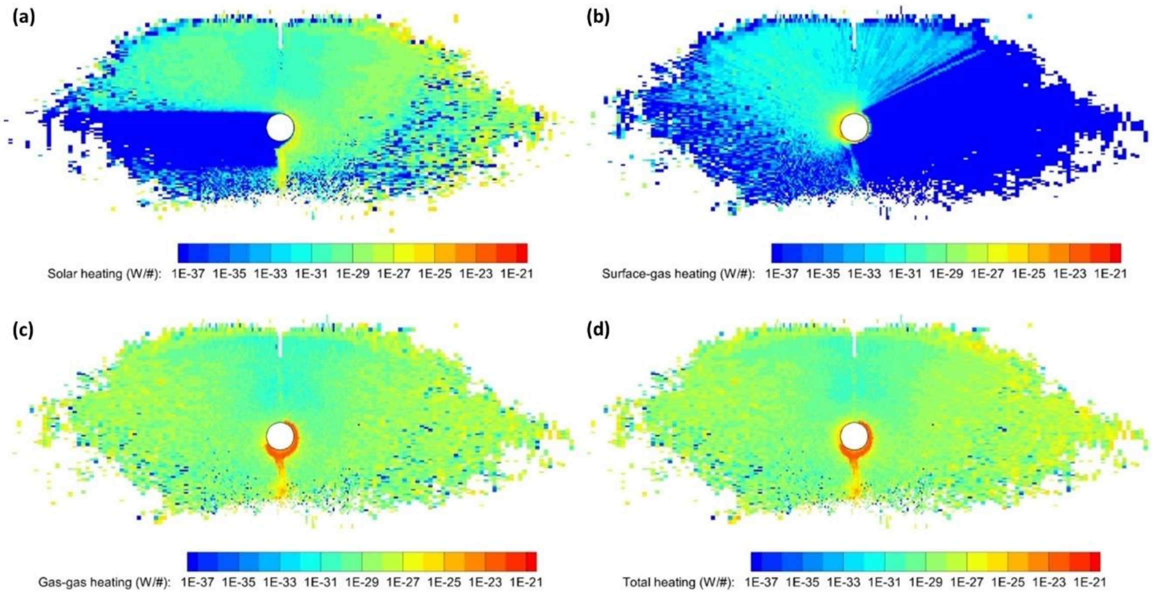

Figure 6.11: Radiative heating rates at 3 hours after impact due to (a) solar radiation, (b) radiation from the lunar surface, (c) reabsorption of spontaneously emitted radiation and (d) the combination of these sources. The rates are computed on a Cartesian grid, and the views shown are in the plane of impact, with sunlight passing through the vapor cloud from right to left. Note that the gas-gas heating rate shown in (c) represents the heating of the gas in a cell due to reabsorption of molecular radiation emitted from *other* cells only.

Radiation from the lunar surface contributes less than solar radiation to heating the vapor cloud, except near the night side surface. Somewhat counterintuitively, it appears from Figure 6.11(b) that the relatively cold lunar night-side surface plays more of a role in heating the gas than the warmer day-side surface. This is due to the structure of the impact-generated atmosphere at this stage; the dense day-side atmosphere traps radiation from the day-side surface at low altitudes, while radiation from the night-side surface propagates further through a more diffuse region of the vapor cloud.

Figure 6.11(c) shows the self-heating of the vapor cloud due to the reabsorption of molecular radiation. (Note that this plot only accounts for the heating of each cell by surrounding cells, i.e. heating due to the trapping of radiation within the cell in which it is emitted is not included.) The self-heating rate correlates strongly with the temperature fields shown in Figures 6.7 and 6.8, since warmer (and denser, in the simulated scenario) regions of the atmosphere emit and absorb more strongly. Comparing Figures 6.11(a), (b) and (c) to Figure 6.11(d), it can be seen that the dominant radiative heating mechanism almost everywhere in the atmosphere appears to be the reabsorption of spontaneously emitted radiation – only in the cold, low-altitude region over the night side does heating by the lunar surface dominate. However, Figure 6.11(d) shows only the total heating rate, and does not account for radiative cooling of the gas.

As described in Section 3.5.3, the rate of radiative cooling is computed at each time-step, using an opacity factor (f_i) to account for the trapping of radiation in the cell i from which it is emitted (such that if $f_i = 1$, the net radiative cooling rate of the cell is zero). Figure 6.12(a) shows the opacity of the vapor cloud at 3 hours after impact. It can be seen that at this stage, all occupied computational cells are close to opaque; > 94% of the radiation emitted within each cell is reabsorbed in the same cell. This is largely a consequence of the large cell sizes used in the radiative transfer calculation, as well as the density of the vapor at this stage. As expected, the low density fringes of the vapor cloud are more transparent (i.e. opacity is lower). Cell opacities are also relatively low near the boundary of the day-side surface shock. These are cells where the gas temperature is high (leading to strong emission), but the gas density is relatively low (leading to less trapping of emitted radiation).

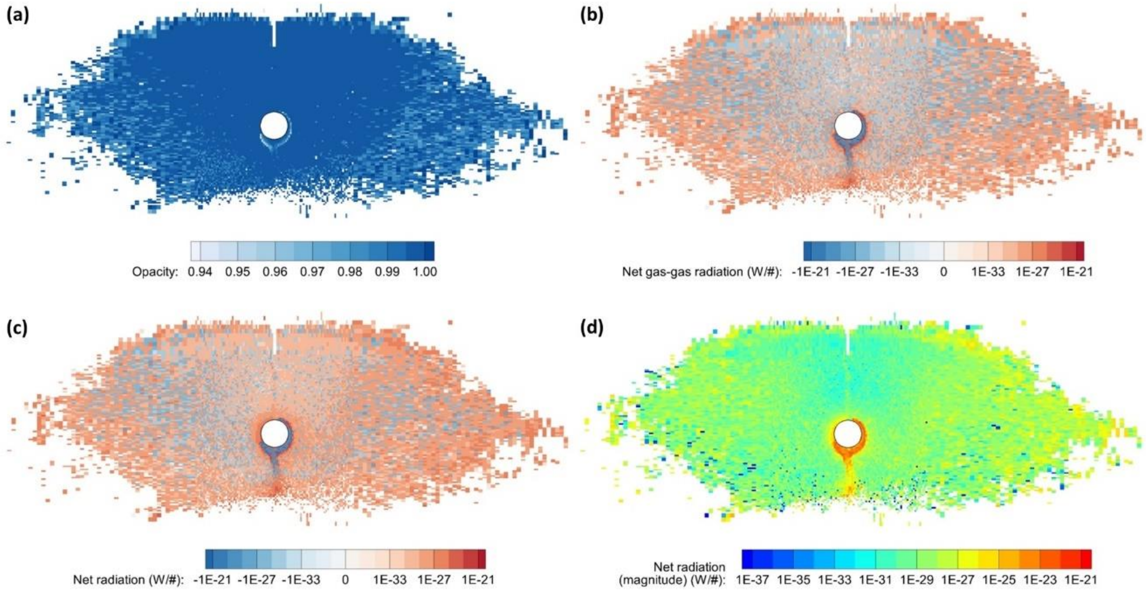

Figure 6.12: (a) Opacity of computational cells; (b) net gas-gas radiative transfer rate; (c) net radiative transfer rate due to all modeled mechanisms, and (d) the *magnitude* of net radiative transfer. Negative values in (b) and (c) indicate regions that experience net cooling due to gas-gas radiation or due to all modeled mechanisms, respectively. All the quantities shown are computed on a Cartesian grid, and the views shown are in the plane of impact, at 3 hours after impact. The Sun is to the right.

Figure 6.12(b) shows the net rate of gas-gas radiative transfer; i.e. the heating rates shown in Figure 6.11(c) minus radiative cooling rates based on gas temperature, modulated by cell opacities. Due to the high cell opacities, the net rates of radiative heating/cooling are quite low and somewhat noisy over much of the vapor cloud. The strongest net cooling is experienced by gas compressed and heated by the day-side and antipodal shocks, though despite the relatively strong rate of cooling, the shock-heated gas remains much warmer in this case than when the atmosphere is modeled as transparent. Figure 6.12(c) adds in the radiative contributions of the Sun and the lunar surface. Comparing Figures 6.12(b) and 6.12(c) it can again be seen that gas-gas radiative transfer is the dominant heating/cooling mechanism in the impact-generated atmosphere at this stage. Surface-gas radiative transfer leads to a net heating of cold, low-altitude gas above the lunar night-side while solar heating partially compensates for radiative cooling in the denser, more strongly absorbing regions of the vapor cloud, most noticeably at high altitudes above the point of impact. Figure 6.12(d) shows the magnitude of net radiative heating/cooling on the same color scale as Figure 6.11, for reference.

By influencing the structure of an impact-generated atmosphere, radiative heat transfer influences the transport of impact-generated vapor and its deposition at polar cold traps. Figure 6.13 shows several different views of the surface density of water molecules adsorbed to the lunar surface at 6 hours after impact in the two modeled cases. (Note that both cases used the surface roughness model corresponding to Case 1 in Chapter 5.) The most significant consequence of the more comprehensive radiative heat transfer model is increased deposition of water on the night-side in the vicinity of the terminator and poles – this follows from the finding that day-side winds travel further on to the night-side when the trapping of energy within the collapsing vapor cloud is accounted for. Table 6.1 quantifies differences in mass lost (primarily due to photodestruction, with a small amount of escape), cold-trapped, adsorbed and aloft at 6 hours after impact, in the two modeled cases.

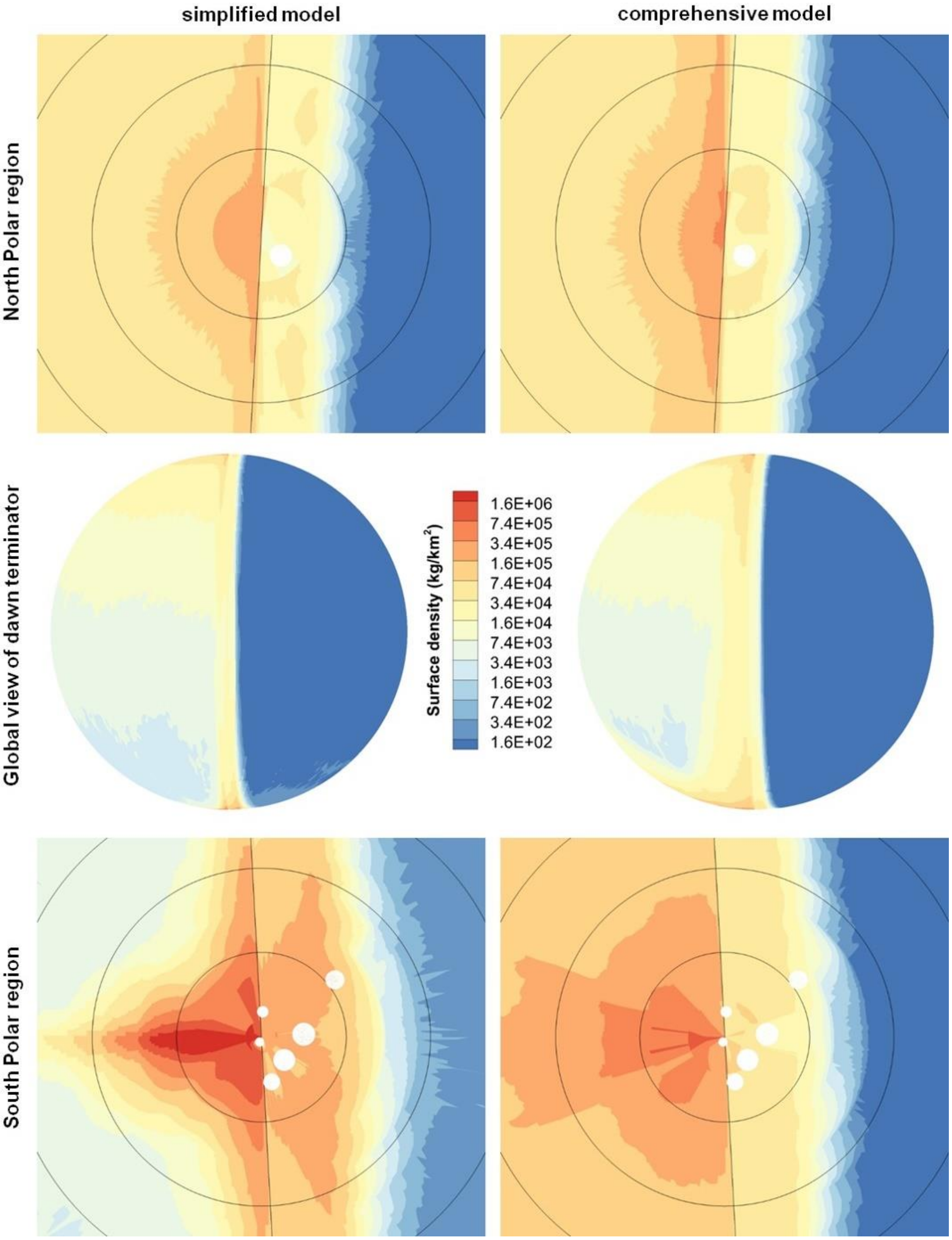

Figure 6.13: Surface density of water adsorbed to the lunar surface at 6 hours after impact in simulations adopting simplified and comprehensive models for radiative heat transfer (see text for details). The black lines in the North Polar and South Polar views mark the dawn terminator and circles of constant latitude at 5° intervals, and the white circles indicate the modeled cold traps. In all the views, the day-side is on the right.

	Mass of water [kg]				
	Lost	***Cold-trapped***		***Adsorbed***	***Aloft***
		North Pole	***South Pole***		
Simplified model	1.87×10^{10}	5.33×10^{7}	2.87×10^{9}	3.00×10^{11}	4.94×10^{11}
Comprehensive model	9.70×10^{9} **(0.52× ↓)**	1.50×10^{8} **(2.82× ↑)**	8.21×10^{8} **(0.29× ↓)**	4.01×10^{11} **(1.34× ↑)**	4.03×10^{11} **(0.82× ↓)**

Table 6.1: Comparison of *cumulative* mass lost (largely due to photodestruction, but also some escape) and cold-trapped, and *instantaneous* mass adsorbed and aloft in simulations adopting simplified and comprehensive models for radiative heat transfer (see text for details) at 6 hours after impact. The ratio of the quantities in the latter case to those in the former case, and whether this constitutes an increase or decrease, is also indicated. Note that the cumulative quantities do not include the small amount of material lost/cold-trapped within the initial 1 hour after impact.

It can be seen from Table 6.1 that adopting the more comprehensive model for radiative heat transfer leads to a decrease in the amount of water photodestroyed (gravitational escape accounts only for 2-3% of the total mass “lost”), an increase in the amount of material cold-trapped at the North Pole, and a decrease in the amount of material cold-trapped at the South Pole. All of these differences are related to the structure of the day-side winds, which carry water vapor further over to the night side when the trapping of radiation is included. This results in a greater proportion of water adsorbed to the night side; since these molecules are protected from photodestruction, the atmospheric loss rate is reduced. The increased strength of the day-side winds in the vicinity of the terminator appears to assist in the transport of water to the North Polar cold trap. However, at the South Pole, the day-side winds tend to “overshoot” the cold traps; this, together with a more diffuse antipodal shock (see Figure 6.10) results in less focusing of water vapor into the South Polar cold traps when the comprehensive radiative heat transfer model is applied. As also noted in Chapter 4, the trends in cold-trap capture are sensitive to the location (latitude and local time) of the impact. However, the increased efficacy of the day-side winds in transporting vapor to the night-side should not be very sensitive to impact parameters.

The simulations presented in this section were run primarily for comparative purposes and did not track the evolution of the atmosphere beyond 6 hours after impact. However, the results obtained illustrate that at this early stage in the evolution of the impact-generated atmosphere, a comprehensive treatment of radiative heat transfer, taking into account the attenuation and trapping of radiation, not only influences the thermal evolution of the atmosphere (in itself an important factor for processes such as phase change and chemistry) but also affects atmospheric structure – and thereby volatile transport, loss and deposition.

Chapter 7: Conclusions

7.1. CHAPTER OVERVIEW

This concluding chapter aims to synthesize and summarize results from previous chapters, before outlining questions for further investigation and suggesting developments to the computational method that may assist these future investigations.

7.2. SYNTHESIS AND SUMMARY OF RESULTS

As discussed in Chapter 1, the overarching objective of this work is to develop a broad understanding of the physical processes that govern the fate of impact-delivered volatiles (particularly water), focusing on three major themes, broadly corresponding to material discussed in Chapters 4-6, respectively:

- *Gas dynamic interactions.* What features characterize volatile transport after an impact? How do these features influence the volatile fallout from the impact?
- *Gas-surface interactions.* How does the distinctive lunar surface thermal environment (particularly the presence of large temperature gradients over very small scales) influence the fate of impact-delivered water?
- *Gas-radiation interactions.* How do shielding and radiative heat transfer affect the structure of the transient atmosphere and the redistribution of water?

Gas dynamic simulations, initialized using representative impact parameters, show that a lunar comet impact can give rise to a gravitationally bound, transient atmosphere that remains collisional for one or more lunar days. In this work, we find that the collisional nature of the atmosphere gives rise to certain characteristic features. Cold, supersonic vapor falling back to the lunar day-side is compressed and heated as it passes through a low-altitude shock; below this shock, the transport of water vapor occurs through winds driven by global pressure gradients and the momentum of the infalling gas, leading to an overall transport of vapor from the lunar day side to the night side. Another characteristic feature is a columnar shock that forms above the impact antipode due to the reconvergence of the collisional, expanding vapor cloud. The strength of these shock structures may vary with impact parameters and the inclusion of more detailed physics, but they are *characteristic* structures that should arise whenever a nominally airless body holds a sufficient quantity of volatiles gravitationally bound after impact. More specifically, antipodal and surface shocks (and the associated surface winds) should arise whenever the infalling vapor is collisional and supersonic; additionally, in order to sustain a surface shock, the surface should not behave as a temporary (or permanent) cold trap for the volatile(s) in question.

The question of how the characteristic structure of an impact-generated atmosphere affects the volatile fallout from an impact is more sensitive to impact parameters, including the location (latitude and time) of the impact. In this work, I found that an impact at the lunar North Pole could lead to non-uniform cold-trapping (at least in the short-term aftermath of the impact) and more concentrated deposits of water at the South Pole. These results demonstrate that a comet impact may leave distribute volatiles non-uniformly between cold traps, with the collisional nature of the transient atmosphere playing a role in generating non-uniformity. The finding that the antipodal reconvergence of the expanding vapor cloud can enhance deposition of volatiles in the vicinity of the antipode is also significant. From collisionless Monte Carlo simulations, Schorghofer (2014) finds that the pole closer to the point of impact accumulates more water, whereas the results presented here show that the opposite may occur.

In addition to gas dynamic interactions, gas-surface interactions also play an important role in the transport and sequestration of lunar volatiles. Although gas dynamic interactions dominate the short-term aftermath of an impact, gas-surface interactions influence both the short-term and late-term redistribution of impact-delivered water. In turn, gas-surface interactions are largely controlled by the surface thermal environment. In this work, I developed a rough surface temperature model that can be readily coupled to Monte Carlo or DSMC simulations of volatile transport (or other problems involving temperature-dependent interactions of particles with stochastically rough surfaces) on airless, slow-rotating bodies where an assumption that surface emission is balanced by insolation is valid. In the simulations presented here, surface temperature determines the average residence time of molecules on the lunar surface and the distribution of velocities with which molecules leave the surface. To quantify the extent to which sub-pixel surface roughness affects volatile transport, it is useful to define a ‘sticking probability’, defined as the fraction of molecules interacting with each pixel that are likely to reside on sub-pixel surfaces for timescales longer than the ballistic timescale.

Based on sticking probabilities, it is found that the influence of surface roughness is most important at high solar incidence angles (i.e. near the day-night terminator and the poles), where surfaces are cooler and more of the surface is in shadow. Near the poles, cool slopes and shadows are present throughout the lunar day and act as temporary reservoirs for water, capturing and concentrating migrating atmospheric (or exospheric) molecules at these high latitudes. On the one hand, this means that surface roughness reduces the mobility of water at high latitudes (and also slows the rate of transport over the day-side hemisphere), but on the other hand, the increased concentration of water molecules in the vicinity of the poles increases the likelihood that molecules will reach a permanently shadowed region. Ultimately, the interplay between these factors and atmospheric gas dynamics influences the fate of impact-delivered water.

Surface roughness also has other, more subtle, consequences. The modification of the distribution of velocities with which molecules scatter off the surface leads to a slight increase in thermal escape *in the late-term collisionless limit*; at earlier times, this aspect of the gas-surface interaction is subsumed by the gas dynamics of the transient atmosphere. Similarly in the late-term limit (when volatile transport is driven by the sublimation and diffusion of adsorbed water at the dawn terminator), the blurring of the terminator due to surface roughness may slightly alter exospheric structure.

The last theme explored in this dissertation was the role of radiative interactions in an impact-generated atmosphere. I focused on two aspects of the gas-radiation interaction thought to be the most significant: the self-shielding of water vapor from photodestruction (the major loss process for gravitationally bound material) due to the attenuation of solar ultraviolet radiation by an absorbing atmosphere, and radiative heat transfer at far-infrared to microwave wavelengths, from the Sun and the lunar surface to the rotational modes of water molecules. It is important to note that both of these phenomena are less important (likely negligible) for most other mechanisms of volatile delivery which, unlike comet impacts, do not involve the sudden release of a large amount of vapor, leading to a transformation of the lunar exosphere into a collisional and optically thick transient atmosphere. Self-shielding of the atmosphere from photodestruction significantly reduces the rate of loss of water. In the specific impact scenario modeled here, the inclusion of shielding was found to increase the amount of water cold-trapped during the initial 120 hours after impact by a factor of five. Interestingly, the local increases in gas density due to the surface and antipodal shocks play a prominent role in shielding the vapor that lies behind these structures.

The radiative heat transfer model developed in this work shows that, at least in the initial hours after impact, gas-gas radiative transfer (due to the reabsorption of spontaneously emitted molecular radiation) plays a more important role in the rotational energy balance of the impact-generated atmosphere than far-infrared to microwave radiation from the Sun and the lunar surface. The day-side and antipodal shocks are found to shield material not only from photodestruction (as mentioned above), but also from heating by solar radiation. Another notable consequence of the characteristic structure of the atmosphere is that the dense gas below the day-side shock traps most of the radiation emanating from the lunar day-side, such that the cold lunar night-side is able to heat the vapor cloud out to greater distances. The trapping of spontaneously emitted radiation in the optically thick vapor cloud slows the rate of cooling due to expansion of the vapor into vacuum. In the initial stages of atmospheric evolution, most of the vapor cloud is sufficiently collisional that changes in rotational and kinetic energy are coupled, and the rotational and translational temperatures are in close agreement.

Accounting for the trapping and attenuation of far-infrared to microwave radiation does not significantly alter the far-field structure of the impact-generated atmosphere (compared to baseline simulations in which the atmosphere was treated as transparent at these wavelengths), but the near-field structure changes significantly. Since the infalling vapor retains more of its initial thermal energy, the antipodal and surface shocks become more diffuse. Below the day-side shock, the gas remains warm; atmospheric condensation is unlikely at this stage in atmospheric evolution. Due to the increase in the day-side shock stand-off distance and the decrease in shock strength, day-side winds travel further over to the night-side, and deposit more water on the cold night-side surface, where it is shielded from photodestruction. For the specific impact modeled here, this leads to a significant decrease in the overall amount of photodestruction, and an increase in cold-trapping at the North Pole, which is offset by a decrease in cold-trapping at the South Pole. These results can be generalized to reason that accounting for the trapping of radiation in an impact-generated atmosphere should reduce the rate of photodestruction at early times (when the atmosphere is optically thick) due to the increased efficacy of day-side winds in transporting material to the night-side. Radiative heat transfer also influences cold trap deposition patterns, but the nature of this influence depends on the impact location and is less readily generalized.

The broad conclusion derived from the work presented in this dissertation is that the transport and deposition of volatiles in the aftermath of a volatile-rich impact on a nominally airless body is influenced qualitatively and quantitatively by the interplay between a number of physical processes – only some of which have been explored here, but which can be broadly grouped under the themes of gas dynamic interactions, gas-surface interactions and gas-radiation interactions. The simulations undertaken in this work focused on the question of the delivery of water to lunar polar cold traps, but the methods developed, and most of the key results, can be extended to other species and other 'airless' bodies. The next section discusses outstanding questions and possible directions for further investigations.

7.3. SUGGESTIONS FOR FURTHER INVESTIGATIONS

The objective of this work was to provide a broad overview of the physical processes governing the fate of impact-delivered volatiles, and in order to render this task tractable, I largely focused on a single impact scenario and looked in detail mainly at the short-term aftermath of the impact (i.e. the fallback stage). The most straightforward, yet also perhaps the most important, outstanding question to address is the extension of the results discussed here to the long-term aftermath of the impact. Can we identify characteristic stages/features of the transition of the impact-generated atmosphere from the fallback stage to the collisionless limit? (For instance, when does the gas become optically thin? How does this affect atmospheric structure?) Are non-uniform short-term cold-trap deposition patterns preserved in the late-term? How do the results presented here change when a different set of impact parameters or a different impact location is considered? The last two questions are particularly important when it comes to quantifying the contribution of comets to the lunar volatile inventory, or to determining the volatile fallout from some specific impact of interest (e.g. Ernst et al., 2016). The influence of impact speed on volatile retention has been well-studied for a range of impact speeds (e.g. by Ong et al., 2010 and Svetsov and Shuvalov, 2015), but the influence of impact angle – less so. Stewart et al. (2011) found that the total quantity of water cold-trapped was not very sensitive to impact location; however, it would be of interest to investigate how a change in impact location affects the structure of the transient atmosphere (and thereby the mechanisms of volatile transport) and the uniformity (or lack thereof) of cold-trap deposition patterns.

The most important loss process for gravitationally bound water molecules is photodestruction. To better estimate the amount of water lost in this way, this work modified the model used by Stewart (2010) to take into account the role of atmospheric self-shielding in mitigating photolytic losses. However, the model involves some simplifications and assumptions that are worth revisiting. One such assumption is the approximation of the solar spectrum to that of a black body at 5780 K when computing a band-averaged absorption cross-section over the 145-186 nm range (as described in Chapter 3, Section 3.3). This is a reasonably accurate approximation at longer wavelengths, but it may be more appropriate to use a lower black body temperature to approximate the solar spectrum at ultraviolet wavelengths (see Figure 7.1). Alternatively, the capacity of the DSMC code to handle the attenuation of solar radiation on a line-by-line basis could be extended to model the attenuation of solar ultraviolet radiation (currently, only far-infrared to microwave radiation is treated in this way). This approach can also readily accommodate any variations in UV absorption cross-sections with temperature, a factor that is not currently considered.

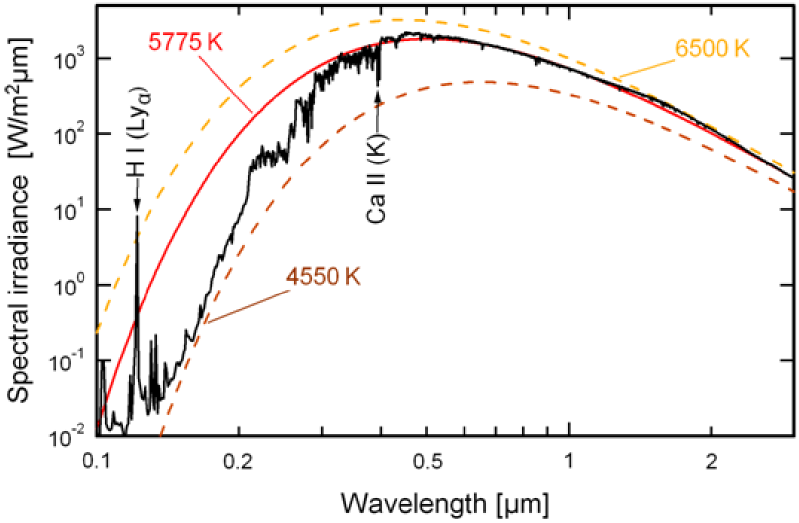

Figure 7.1: The unattenuated solar spectrum at 1 AU (Gueymard, 2004) compared against black body radiation at 4550 K, 5775 K and 6500 K. Also indicated are characteristic spectral lines of hydrogen and calcium. *Image Credit: Pietro P. Altermatt, on-line lectures, www.pvlighthouse.com.au.*

Another key simplification made in the simulations presented here is the deletion of photodissociation products (e.g. H, OH). One consequence of this is that we neglect any energy transfer from these species to the main species of interest (H_2O). However, the significance of this is uncertain, since photodestruction occurs preferentially in the rarefied outer regions of the expanding vapor cloud, where energetic dissociation products are more likely to escape and undergo fewer collisions. Berg et al. (2016) implemented a more accurate treatment of dissociation products, in which excess energy from photodissociation is appropriately partitioned into H and OH. It may be worth adopting this approach in future simulations.

The last assumption of note made in our treatment of photodestruction is that we do not consider water molecules adsorbed to the lunar surface to be susceptible to photodestruction (or other processes, such as photodesorption). This is a common assumption, made in most current models of lunar volatile transport, but one that may be worth revisiting in more detail in light of recent and ongoing work examining the behavior of adsorbed water molecules in the lunar environment (e.g. DeSimone and Orlando, 2014). However, it is also worth noting that adsorbed molecules may be effectively shielded from solar radiation by the presence of a dense day-side atmosphere after a comet impact; losses induced by the irradiation of adsorbed molecules are likely to become significant only in the late-term. Moreover, since molecular residence times on the sunlit surface are short compared to the time spent aloft, the probability of photodestruction when a molecule is adsorbed to the surface is likely to be low.

On a different note, the most important simplification made in this work is perhaps the treatment of the comet as composed solely of water, and the modeling of only a single species (H_2O). In reality, as discussed in Chapter 4 (Section 4.5), chemical reactions among impact-delivered species and dissociation products may give rise to a complex mixture of species. In the collisionless limit, multiple species may be considered to form multiple, non-interacting exospheres (Stern, 1999), but in a collisionally thick atmosphere, this is not the case. This raises a number of interesting and important questions. For instance, do chemical reactions deplete or enhance the atmospheric concentration of water? To what extent do non-condensable species impede the deposition of other species (such as water)? Is there preferential deposition of certain species, such that the composition of cold trap deposits does not mirror the composition of the impactor? These are all questions of considerable importance to interpreting remote sensing data, likely to become even more so as we gain further insight into the composition of cold-trapped volatiles on the Moon, Mercury and other airless bodies.

Modeling interactions between multiple species is a complex task. Although not used in this work, the DSMC code already has the ability to track multiple species and can also model chemical reactions – this is implemented by computing the probability that colliding molecules react, based on reaction cross-section data or Arrhenius rate coefficients (Moore, 2011). Extending code capabilities to the comet impact problem would involve the specification of surface residence times and reaction rates (subject to availability of this data) for the species and reactions of interest, and extension of the shielding and radiative heat transfer algorithms to account for multiple species. An initial step towards capturing the complexities introduced by the presence of multiple species may be to maintain the assumption that water is the only impact-delivered species, but include interactions between dissociation products.

Comets are composed not only of multiple volatile species, but also of substantial amounts of refractory dust. The fate of cometary dust during an impact is uncertain, but if refractory particles were dispersed throughout the impact-generated vapor cloud, this would affect the radiative energy balance of the transient atmosphere and perhaps also its chemistry. The behavior of a *dusty* impact-generated atmosphere may be another avenue for further investigation, well-suited for a DSMC approach. Another source of dust is the lunar regolith. One reason that lunar dust was neglected in this work is that hydrocode simulations on which the DSMC simulations were based indicated that vaporized lunar and cometary material were not well-mixed (for the specified initial conditions and material properties). Scouring and entrainment of the regolith by day-side winds at later times is also unlikely.

The suggestions discussed above have largely to do with gas dynamics. There are also several ways to advance the modeling of gas-surface interactions. The thermal model for small-scale roughness developed in Chapter 3 was constrained to match observed bolometric brightness temperatures at larger scales. Though physically consistent, this is an approximation that stops short of detailed thermal modeling of rough surface temperature distributions, which was beyond the scope of this work. However, as demonstrated in Chapter 5, volatile transport is sensitive to the distribution of shadow temperatures – a general challenge is how to model the rough surface temperature distribution accurately, without imposing a significant computational burden.

The present rough surface model can be adapted and extended in several ways. For instance, the only explicit assumption made regarding the spatial scale of the modeled roughness is that it is smaller than the O(10 km) pixel scale. Consequently, the methods discussed here could be applied to larger-scale roughness on the Moon or other solar system bodies. Different degrees of roughness for different geologic units (e.g. the lunar maria vs. highlands) could also be implemented; in general, surfaces with a greater degree of roughness are expected to have more, but warmer, shadows. It may also be possible to superimpose a thermal model for small-scale roughness over realistic large-scale topography for the Moon and other bodies for which digital elevation models exist.

It would be of interest to examine whether modeling volatile transport (post-impact or otherwise) in conjunction with a detailed surface model, could explain the distribution of hydrogen-bearing species derived from remote-sensing observations, which does not seem to be controlled solely by volatile *stability*.

As noted previously, we do not explicitly model any topography – only the corresponding temperature variations. This approach should be reconsidered if more detailed thermophysical modeling of the lunar surface is pursued. For instance, we currently do not account for the fact that ballistic trajectories of molecules released from sloping surfaces or at grazing angles may be cut short by encounters with surrounding terrain. Butler (1997) provides a brief discussion of this particular issue, which may become more important if rougher surfaces or large-scale roughness are considered.

Several improvements could also be made to the way in which radiative heat transfer was modeled in this work. For instance, the model presently considers only 212 spectral lines in the far-infrared to microwave range, associated with rotational transitions of water in the ground vibrational state. The reasons for this were discussed in Chapter 3, but it may be worthwhile to extend the applicability of the model by taking into account vibrational and electronic excitation. It may also be worth reassessing the role that escaping vapor plays in radiative heat transfer/shielding, and whether this could be approximated without a significant increase in computational cost; e.g. by representing escaping vapor using tracer particles rather than performing full DSMC.

The nuts and bolts of the Monte Carlo radiative heat transfer subroutines of the DSMC code could also be improved upon in several ways. One suggestion is to consider performing the radiative transfer calculation using the same spherical grid as the main DSMC code, rather than a Cartesian grid. The Cartesian grid is slightly more convenient to work with, but using the DSMC grid would reduce the computational overhead and inaccuracies associated with mapping between two grids. At a practical level, this would mainly involve modifying the sections of code that deal with the initialization and propagation of packets of energy (e.g. the random number formulations required to distribute packets uniformly within a cell are different for a spherical vs Cartesian grid). Although the radiative heat transfer subroutines are fairly well-parallelized at present, these are still computationally expensive sections of the code, and modifications that could reduce run-time would be useful.

Lastly, the capabilities developed in this work could be adapted to model a number of other problems. In planetary science alone, rarefied atmospheres and surface boundary exospheres have been observed to exist in a range of different environments throughout the solar system, from Mercury and the Moon to small bodies and outer solar system satellites. Some of these bodies may be visited in the near future – raising the question of how exogenous volatiles (such as spacecraft exhaust) interact with the local environment. Though the source mechanisms may be different in all these cases, the interaction of volatiles with solar radiation and the underlying surface are important. Modeling these interactions, and synthesizing computational results and observational data, is key to understanding the processes that have shaped the worlds around us.

To summarize, the main suggestions for further investigation discussed in this section are as listed below:

- ***Longer term simulations*** of the impact-generated atmosphere as it transitions to the collisionless limit, in order to extend the results discussed here to the long-term aftermath of an impact.
- ***Exploration of parameter space***, particularly impact location, which may *qualitatively* change the structure of the impact-generated atmosphere and the nature of volatile transport and deposition.
- ***Modeling multiple species*** (gas phase, perhaps also dust) and their chemical and gas dynamic interactions, with a view to answeing the question of whether the composition of cold trap deposits mirrors that of the impactor. This would require extensions/updates of code subroutines dealing with photodissociation, chemistry, radiative transfer and gas-surface interactions.
- ***Application of the capabilities developed here*** to study rarefied atmospheres and surface boundary exospheres in other contexts.

References

Aharonson, O. and Schorghofer, N. (2006). Subsurface ice on Mars with rough topography. *Journal of Geophysical Research: Planets*, 111, E11007.

Altermatt, P. P. (2017). Lecture 2: The Solar Spectrum. *www.pvlighthouse.com.au*.

Arnold, J. R. (1979). Ice in the lunar polar regions. *Journal of Geophysical Research*, 84, p. 5659-5668.

Artemieva, N. A. and V. V. Shuvalov (2008). Numerical simulation of high-velocity impact ejecta following falls of comets and asteroids onto the Moon. *Solar System Research,* 42(4), p. 329-334.

Bandfield, J. L., Hayne, P. O., Williams, J., Greenhagen, B. T. and Paige, D. A. (2015). Lunar surface roughness derived from LRO Diviner Radiometer observations. *Icarus*, 248, p. 357-372.

Basilevsky, A. T., Abdrakhimov, A. M. and Dorofeeva, V. A. (2012). Water and other volatiles on the Moon: a review. *Solar System Research*, 46(2), p. 89-107.

Berezhnoi, A. A. and Klumov, B. A. (1998). Lunar ice: can its origin be determined? *J. Experimental and Theoretical Physics Letters*, 68, p. 163-167.

Berezhnoi, A. A. and Klumov, B. A. (2000). Photochemical model of impact-produced lunar atmosphere. *Exploration and Utilisation of the Moon,* p. 175-178.

Berezhnoy, A. A., Hasebe, N., Hiramoto, T. and Klumov, B. A. (2003). Possibility of the presence of S, SO_2, and CO_2 at the poles of the Moon. *Publications of the Astronomical Society of Japan*, 55(4), p. 859-870.

Berg, J. J., Goldstein, D. B., Varghese, P. L. and Trafton, L. M. (2016). DSMC simulation of Europa water vapor plumes. *Icarus*, 277, p. 370-380.

Bernes, C. (1979). A Monte Carlo approach to non-LTE radiative transfer problems. *Astronomy and Astrophysics*, 73, p. 67-73.

Bird, G. A. (1994). *Molecular Gas Dynamics and the Direct Simulation of Gas Flow*. Oxford University Press, New York.

Brownlee, D. E., Hörz, F., Vedder, J. F., Gault, D. E. and Hartung, J. B. (1973). Some physical parameters of micrometeoroids. *Lunar and Planetary Science Conference*, 4, p. 3197.

Buhl, D., Welch, W. J. and Rea, D. G. (1968a). Reradiation and thermal emission from illuminated craters on the lunar surface. *Journal of Geophysical Research*, 73(16), p. 5281-5295.

Buhl, D., Welch, W. J. and Rea, D. G. (1968b). Anomalous cooling of a cratered lunar surface. *Journal of Geophysical Research*, 73(24), p. 7593-7608.

Bussey, D. B. J., Lucey, P. G., Steutel, D., Robinson, M. S., Spudis, P. D. and Edwards, K. D. (2003). Permanent shadow in simple craters near the lunar poles. *Geophysical Research Lett*ers, 30(6).

Butler, B. J. (1997). The migration of volatiles on the surfaces of Mercury and the Moon. *Journal of Geophysical Research: Planets*, 102(E8), p. 19283-19291.

Chabot, N. L., Ernst, C. M., Denevi, B. W., Nair, H., Deutsch, A. N., Blewett, D. T., Murchie, S. L., Neumann, G. A., Mazarico, E., Paige, D. A. and Harmon, J. K. (2014). Images of surface volatiles in Mercury's polar craters acquired by the MESSENGER spacecraft. *Geology*, 42(12).

Clark, R. N. (2009). Detection of adsorbed water and hydroxyl on the Moon. *Science* 326, p. 562-564.

Cochran, A. L. (1982). *The Chemical Evolution of the Coma of Comet P/Stephan-Oterma*. University of Texas, Austin.

Colaprete, A., Schultz, P., Heldmann, J., Wooden, D., Shirley, M., Ennico, K., Hermalyn, B., Marshall, W., Ricco, A., Elphic, R. C., Goldstein, D., Summy, D., Bart, G. D., Asphaug, E., Korycansky, D., Landis, D. and Sollitt, L. (2010). Detection of water in the LCROSS ejecta plume. *Science*, 330, p. 463-468.

Combi, M.R. (1996). Time-dependent gas kinetics in tenuous planetary atmospheres: the cometary coma. *Icarus,* 123, p. 207-226.

Cook, J. C., Stern, S. A., Feldman, P. D., Gladstone, G. R., Retherford, K. D. and Tsang, C. C. (2013). New upper limits on numerous atmospheric species in the native lunar atmosphere. *Icarus*, 225, p. 681-687.

Crider, D. H. and Vondrak, R. R. (2000). The solar wind as a possible source of lunar polar hydrogen deposits. *Journal of Geophysical Research: Planets,* 105, p. 26773-26782.

Crider, D. H. and Vondrak, R. R. (2002). Hydrogen migration to the lunar poles by solar wind bombardment of the Moon. *Advances in Space Research*, 30, p. 1869-1874.

Crider, D. H. and Vondrak, R. R. (2003). Space weathering of ice layers in lunar cold traps. *Advances in Space Research*, 31(11), p. 2293-2298.

Crovisier, J. T. (1984). The water molecule in comets- fluorescence mechanisms and thermodynamics of the inner coma. *Astronomy and Astrophysics*, 130, p. 361-372.

Crovisier, J. (1989). The photodissociation of water in cometary atmospheres. *Astronomy and Astrophysics*, 213, p. 459-464.

Davidsson, B. J., Rickman, H., Bandfield, J. L., Groussin, O., Gutiérrez, P. J., Wilska, M., Capria, M. T., Emery, J. P., Helbert, J., Jorda, L. and Maturilli, A. (2015). Interpretation of thermal emission. I. The effect of roughness for spatially resolved atmosphereless bodies. *Icarus*, 252, p. 1-21.

Debout, V., Bockelée-Morvan, D. and Zakharov, V. (2016). A radiative transfer model to treat infrared molecular excitation in cometary atmospheres. *Icarus*, 265, p. 110-124.

DeSimone, A. J. and Orlando, T. M. (2014). Mechanisms and cross sections for water desorption from a lunar impact melt breccia. *Journal of Geophysical Research: Planets*, 119(4), p. 884-893.

Elbeshausen, D., Wünnemann, K. and Collins, G. S. (2009). Scaling of oblique impacts in frictional targets: Implications for crater size and formation mechanisms. *Icarus*, 204(2), p. 716-731.

Ernst, C. M., Chabot, N. L. and Barnouin, O. S. (2016). Examining the Potential Contribution of the Hokusai Impact to Water Ice on Mercury. *Lunar and Planetary Science Conference*, 47, p. 1374.

Feldman, W. C., Lawrence, D. J., Elphic, R. C., Barraclough, B. L., Maurice, S., Genetay, I., and Binder, A. B. (2000). Polar hydrogen deposits on the Moon. *Journal of Geophysical Research*, 105, p. 4175-4195.

Fleagle, R. G. and Businger, J. A. (1980). *An Introduction to Atmospheric Phys*ics. International Geophysics Series, Academic Press, Vol. 25, New York, p. 69-72.

Frenkel, Z. (1924). Theorie der adsorption und verwandter erscheinungen. *Zeitschrift für Physik,* 26, p. 117-138.

Gersch, A. M. and A'Hearn, M. F. (2014). Coupled escape probability for an asymmetric spherical case: Modeling optically thick comets. *The Astrophysical Journal*, 787(1), p. 36.

Giguere, P. T. and Huebner, W. F. (1978). A model of comet comae. I-Gas-phase chemistry in one dimension. *The Astrophysical Journal*, 223, p. 638-654.

Gisler, G. R., Weaver, R. P. and Gittings, M. L. (2006). Energy partitions in three-dimensional simulations of the Chicxulub meteor impact. *Lunar and Planetary Science Conference*, 37, p. 2095.

Gladstone, G. R., Retherford, K. D., Egan, A. F., Kaufmann, D. E., Miles, P. F., Parker, J. W., Horvath, D., Rojas, P. M., Versteeg, M. H., Davis, M. W., Greathouse, T. K., Slater, D. C., Mukherjee, J., Steffl, A. J., Feldman, P. D., Hurley, D. M., Pryor, W. R., Hendrix, A. R., Mazarico, E. and Stern, S. A. (2012). Far-ultraviolet reflectance properties of the Moon's permanently shadowed regions. *Journal of Geophysical Research: Planets*, 117, E00H04.

Gombosi, T. I., Nagy, A. F. and Cravens, T. E. (1986). Dust and neutral gas modeling of the inner atmospheres of comets. *Reviews of Geophysics*, 24, p. 667-700.

Gratiy, S. L., Levin, D. A. and Walker, A. C. (2010). Rassvet: Backward Monte Carlo radiative transfer in spherical-shell planetary atmospheres. *Icarus*, 206(1), p. 366-379.

Grava, C., Chaufray, J. Y., Retherford, K. D., Gladstone, G. R., Greathouse, T. K., Hurley, D. M., Hodges, R. R., Bayless, A. J., Cook, J. C. and Stern, S. A. (2015). Lunar exospheric argon modeling. *Icarus*, 255, p. 135-147.

C. Gueymard (2004). The Sun's total and spectral irradiance for solar energy applications and solar radiation models. *Solar Energy*, p. 423-453.

Haruyama, J., Ohtake, M., Matsunaga, T., Morota, T., Honda, C., Yokota, Y., Pieters, C. M., Hara, S., Hioki, K., Saiki, K., Miyamoto, H., Iwasaki, A., Abe, M., Ogawa, Y., Takeda, H., Shirao, M., Yamaji, A. and Josset, J.-L. (2008). Lack of exposed ice inside lunar South Pole Shackleton crater. *Science*, 322, p. 938-939.

Hayne, P. O., Williams, J.-P., Siegler, M. and Paige, D. (2013). Little cold traps on the Moon. *Lunar Volatiles Workshop Without Walls* 2013.

Hayne, P. O. and Aharonson, O. (2015). Thermal stability of ice on Ceres with rough topography. *JGR: Planets*, 120(9), p. 1567-1584.

Hodges, R. R. (1972). Applicability of a diffusion model to lateral transport in the terrestrial and lunar exospheres. *Planetary and Space Science*, 20(1), p. 103-115.

Hodges, R. R. (2002). Ice in the lunar polar regions revisited. *Journal of Geophysical Research: Planets*, 107(E2).

Hogerheijde, M. R. and van der Tak, F. F. (2000). An accelerated Monte Carlo method to solve two-dimensional radiative transfer and molecular excitation. *Astronomy and Astrophysics,* 362, p. 697-710.

Hood, L. L. and Artemieva, N. A. (2008). Antipodal effects of lunar basin-forming impacts: Initial 3D simulations and comparisons with observations. *Icarus*, 193(2), p. 485-502.

Housen, K. R. and Holsapple, K. A. (2011). Ejecta from impact craters. *Icarus*, 211(1), p. 856-875.

Huebner, W. F. (1985). The photochemistry of comets. *The photochemistry of atmospheres: Earth, the other planets, and comets.* Orlando, FL, Academic Press, Inc., p. 437-481.

Huebner, W. F. and Keady, J. J. (1984). First-flight escape from spheres with R^{-2} density distribution. *Astronomy and Astrophysics*, 135, p. 177-180.

Huebner, W. F., Keady, J. J. and Lyon, S. P. (1992). Solar photo rates for planetary atmospheres and atmospheric pollutants. *Astrophysics and Space Science,* 195, p. 1-294.

Hurley, D. M., Sarantos, M., Grava, C., Williams, J., Retherford, K. D., Siegler, M., Greenhagen, B. T. and Paige, D. A. (2015). An analytic function of lunar surface temperature for exospheric modeling. *Icarus*, 255, p. 159-163.

Hurley, D. M., Cook, J. C., Benna, M., Halekas, J. S., Feldman, P. D., Retherford, K. D., Hodges, R. R., Grava, C., Mahaffy, P., Gladstone, G. R. and Greathouse, T. (2016). Understanding temporal and spatial variability of the lunar helium atmosphere using simultaneous observations from LRO, LADEE, and ARTEMIS. *Icarus*, 273, p. 45-52.

Ingersoll, A. P., Svitek, T. and Murray, B. C. (1992). Stability of polar frosts in spherical bowl-shaped craters on the Moon, Mercury, and Mars. *Icarus*, 100(1), p. 40-47.

Keihm, S., Tosi, F., Capria, M.T., De Sanctis, M. C., Longobardo, A., Palomba, E., Russell, C. T. and Raymond, C. A. (2015). Separation of thermal inertia and roughness effects from Dawn/VIR measurements of Vesta surface temperatures in the vicinity of Marcia Crater. *Icarus*, 262, p. 30-43.

Keller, J. W., Petro, N. E. and Vondrak, R. R. (2016). The Lunar Reconnaissance Orbiter Mission–Six years of science and exploration at the Moon. *Icarus*, 273, p. 2-24.

Langmuir, I. (1916). The evaporation, condensation and reflection of molecules and the mechanism of adsorption. *Physical Review*, 8, p. 149-176.

Le Feuvre, M. and Wieczorek, M. A. (2008). Non-uniform cratering of the terrestrial planets. *Icarus*, 197(1), p. 291-306.

Li, S. and Milliken, R. E. (2013). Quantitative Mapping of Lunar Surface Hydration with Moon Mineralogy Mapper (M^3) Data. *Lunar and Planetary Science Conference*, 44, p. 1337.

Livengood, T. A., Chin, G., Sagdeev, R. Z., Mitrofanov, I. G., Boynton, W. V., Evans, L. G., Litvak, M. L., McClanahan, T. P., Sanin, A. B., Starr, R. D. and Su, J. J. (2015). Moonshine: Diurnally varying hydration through natural distillation on the Moon, detected by the Lunar Exploration Neutron Detector (LEND). *Icarus*, 255, p.100-115.

Lee, S., von Allmen, P., Kamp, L., Gulkis, S. and Davidsson, B. (2011). Non-LTE radiative transfer for sub-millimeter water lines in Comet 67P/Churyumov-Gerasimenko. *Icarus*, 215(2), p. 721-731.

Marconi, M. L. and Mendis, D. A. (1986). Infrared heating of Comet Halley's atmosphere. *Earth, Moon, and Planets*, 36(3), p. 249-256.

McCord, T. B., Taylor, L. A., Combe, J. P., Kramer, G., Pieters, C. M., Sunshine, J. M. and Clark, R. N. (2011). Sources and physical processes responsible for OH/H_2O in the lunar soil as revealed by the Moon Mineralogy Mapper (M^3). *Journal of Geophysical Research: Planets*, 116, E00G05.

McDoniel, W. J. (2015). *Realistic simulation of Io's Pele plume and its effects on Io's atmosphere*. University of Texas, Austin.

McDoniel, W. J., Goldstein, D. B., Varghese, P. L. and Trafton, L. M. (2015). Three-dimensional simulation of gas and dust in Io's Pele plume. *Icarus*, 257, p. 251-274.

Miller, R. S., Lawrence, D. J. and Hurley, D. M. (2014). Identification of surface hydrogen enhancements within the Moon's Shackleton crater. *Icarus*, 233, p. 229-232.

Mitrofanov, I. G., Sanin, A. B., Boynton, W. V., Chin, G., Garvin, J. B., Golovin, D., Evans, L. G., Harshman, K., Kozyrev, A. S., Litvak, M. L. and Malakhov, A. (2010). Hydrogen mapping of the Lunar South Pole using the LRO Neutron Detector Experiment LEND. *Science*, 330(6003), p. 483-486.

Mitrofanov, I., Litvak, M., Sanin, A., Malakhov, A., Golovin, D., Boynton, W., Droege, G., Chin, G., Evans, L., Harshman, K. and Fedosov, F. (2012). Testing polar spots of water-rich permafrost on the Moon: LEND observations onboard LRO. *Journal of Geophysical Research: Planets*, 117(E12).

Modest, M. F. (2003). *Radiative Heat Transfer.* Academic Press, USA.

Moore, C. H., Goldstein, D. B., Varghese, P. L., Trafton, L. M. and Stewart, B. (2009). 1-D DSMC simulation of Io's atmospheric collapse and reformation during and after eclipse. *Icarus*, 201(2), p. 585-597.

Moore, C. H. (2011). *Monte Carlo simulation of the Jovian plasma torus interaction with Io's atmosphere and the resultant aurora during eclipse.* University of Texas, Austin.

Moores, J. E. (2016). Lunar water migration in the interval between large impacts: Heterogeneous delivery to Permanently Shadowed Regions, fractionation, and diffusive barriers. *Journal of Geophysical Research: Planets*, 121(1), p.46-60.

Morgan, T. H. and Shemansky, D. E. (1991). Limits to the lunar atmosphere. *Journal of Geophysical Research: Space Physics*, 96(A2), p.1351-1367.

Nanbu, K. (1986). Theoretical basis on the direct Monte Carlo method. *15th International Symposium on Rarefied Gas Dynamics*, p. 369-383.

National Research Council (2007). *The Scientific Context for Exploration of the Moon: Final Report*. Washington, DC: The National Academies Press.

Neish, C. D., Bussey, D. B. J., Spudis, P., Marshall, W., Thomson, B. J., Patterson, G. W. and Carter, L. M. (2011). The nature of lunar volatiles as revealed by Mini-RF observations of the LCROSS impact site. *Journal of Geophysical Research: Planets*, 116(E1).

NIST Chemistry WebBook, Thermodynamics Source Database, NIST Standard Reference Database Number 69, Eds. P.J. Linstrom and W.G. Mallard.

Nozette, S., Lichtenberg, C. L., Spudis, P., Bonner, R., Ort, W., Malaret, E., Robinson, M. and Shoemaker, E. M. (1996). The Clementine bistatic radar experiment. *Science*, Vol. 274, p. 1495-1498.

O'Hanlon, J. F. (2005). *A User's Guide to Vacuum Technology*. John Wiley & Sons.

Ong, L., Asphaug, E. I., Korycansky, D. and Coker, R. F. (2010). Volatile retention from cometary impacts on the Moon. *Icarus*, 207(2), p. 578-589.

Ozawa, T., Levin, D. A., Wang, A. and Modest, M. F. (2010). Development of Coupled Particle Hypersonic Flowfield-Photon Monte Carlo Radiation Methods. *Journal of Thermophysics and Heat Transfer*, 24(3), p. 612-622.

Paige, D. A., Siegler, M. A., Zhang, J. A., Hayne, P. O., Foote, E .J., Bennett, K. A., Vasavada, A. R., Greenhagen, B. T., Schofield, J. T., McCleese, D. J. and Foote, M. C. (2010). Diviner lunar radiometer observations of cold traps in the Moon’s South Polar region. *Science*, 330(6003), p. 479-482.

Penner, S. S. (1959). *Quantitative Molecular Spectroscopy and Gas Emissivities*. Addison-Wesley Pub. Co.

Pierazzo, E. and Melosh, H. J. (2000). Hydrocode modeling of oblique impacts: The fate of the projectile. *Meteoritics and Planetary Science*, 35(1), p. 117-130.

Pieters, C. M., Goswami, J. N., Clark, R. N., Annadurai, M., Boardman, J., Buratti, B., Combe, J. P., Dyar, M. D., Green, R., Head, J. W. and Hibbitts, C. (2009). Character and spatial distribution of OH/H_2O on the surface of the Moon seen by M^3 on Chandrayaan-1. *Science*, 326(5952), p. 568-572.

Poston, M. J., Grieves, G. A., Aleksandrov, A. B., Hibbitts, C. A., Dyar, M. D. and Orlando, T. M. (2015). Temperature programmed desorption studies of water interactions with Apollo lunar samples 12001 and 72501. *Icarus*, 255, p. 24-29.

Prem, P., Artemieva, N. A., Goldstein, D. B., Varghese, P. L. and Trafton, L. M. (2015). Transport of water in a transient impact-generated lunar atmosphere. *Icarus,* 255, p. 148–158.

Prem, P., Goldstein, D. B., Varghese, P. L. and Trafton, L. M. (2017). The influence of surface roughness on volatile transport on the Moon (under review).

Rosenburg, M. A., Aharonson, O., Head, J. W., Kreslavsky, M. A., Mazarico, E., Neumann, G. A., Smith, D. E., Torrence, M. H. and Zuber, M.T. (2011). Global surface slopes and roughness of the Moon from the Lunar Orbiter Laser Altimeter. *Journal of Geophysical Research: Planets*, 116(E2).

Roth, N. and Kasen, D. (2015). Monte Carlo Radiation-Hydrodynamics with Implicit Methods. *The Astrophysical Journal Supplement Series*, 217(1), 9.

Roveda, R., Goldstein, D. B. and Varghese, P. L. (2000). Hybrid Euler/direct simulation Monte Carlo calculation of unsteady slit flow. *Journal of Spacecraft and Rockets*, 37(6), p. 753-760.

Rubanenko, L., Aharonson, O. and Schorghofer, N. (2016). Temperature Distribution of Rough Airless Bodies and Volatile Stability. *Lunar and Planetary Science Conference*, 47, p. 1650.

Salo, H. (1988). Monte Carlo modeling of the net effects of coma scattering and thermal reradiation on the energy input to cometary nucleus. *Icarus*, 76(2), p. 253-269.

Sandford, S. A. and Allamandola, L. J. (1993). The condensation and vaporization behavior of ices containing SO_2, H_2S, and CO_2: Implications for Io. *Icarus*, 106(2), p. 478-488.

Schorghofer, N. and Taylor, G. J. (2007). Subsurface migration of H_2O at lunar cold traps. *Journal of Geophysical Research: Planets*, 112(E2).

Schorghofer, N. (2014). Migration calculations for water in the exosphere of the Moon: Dusk-dawn asymmetry, heterogeneous trapping, and D/H fractionation. *Geophysical Research Letters*, 41(14), p. 4888-4893.

Schultz, P. H. (1996). Effect of impact angle on vaporization. *Journal of Geophysical Research*, 101, p. 21-117.

Shepard, M. K., Brackett, R. A. and Arvidson, R. E. (1995). Self-affine (fractal) topography: Surface parameterization and radar scattering. *Journal of Geophysical Research: Planets*, 100(E6), p. 11709-11718.

Shimizu, M. (1976). The structure of cometary atmospheres. *Astrophysics and Space Science*, 40(1), p. 149-155.

Shuvalov, V. V. (1999). Multi-dimensional hydrodynamic code SOVA for interfacial flows: Application to the thermal layer effect. *Shock Waves*, 9(6), p. 381-390.

Siegler, M., Paige, D., Williams, J. P. and Bills, B. (2015). Evolution of lunar polar ice stability. *Icarus*, 255, p. 78-87.

Siegler, M. A., Miller, R. S., Keane, J. T., Laneuville, M., Paige, D. A., Matsuyama, I., Lawrence, D. J., Crotts, A. and Poston, M. J. (2016). Lunar true polar wander inferred from polar hydrogen. *Nature*, 531(7595), p. 480-484.

Simpson, R. A. and Tyler, G. L. (1999). Reanalysis of Clementine bistatic radar data from the lunar south pole. *Journal of Geophysical Research: Planets*, 104(E2), p. 3845-3862.

Smith, B. G. (1967). Lunar surface roughness: Shadowing and thermal emission. *Journal of Geophysical Research*, 72(16), p. 4059-4067.

Sohn, I., Li, Z., Levin, D. A. and Modest, M. F. (2012). Coupled DSMC-PMC radiation simulations of a hypersonic reentry. *Journal of Thermophysics and Heat Transfer*, 26(1), p. 22-35.

Spudis, P. D., Bussey, D. B. J., Baloga, S. M., Butler, B. J., Carl, D., Carter, L. M., Chakraborty, M., Elphic, R. C., Gillis-Davis, J. J., Goswami, J. N. and Heggy, E. (2010). Initial results for the North Pole of the Moon from Mini-SAR, Chandrayaan-1 mission. *Geophysical Research Letters*, 37(6).

Spudis, P. D., Bussey, D. B. J., Baloga, S. M., Cahill, J. T. S., Glaze, L. S., Patterson, G. W., Raney, R. K., Thompson, T. W., Thomson, B. J. and Ustinov, E. A. (2013). Evidence for water ice on the Moon: Results for anomalous polar craters from the LRO Mini-RF imaging radar. *Journal of Geophysical Research: Planets*, 118(10), p. 2016-2029.

Stacy, N. J. S., Campbell, D. B. and Ford, P. G. (1997). Arecibo radar mapping of the lunar poles: A search for ice deposits. *Science*, 276(5318), p. 1527-1530.

Stern, S. A. (1999). The lunar atmosphere: History, status, current problems, and context. *Reviews of Geophysics*, 37(4), p. 453-491.

Stewart, B., Pierazzo, E., Goldstein, D., Varghese, P., Trafton, L. and Moore, C. (2009). Parallel 3D hybrid continuum/DSMC method for unsteady expansions into a vacuum. *47th AIAA Aerospace Sciences Meeting*, p. 266.

Stewart, B. D. (2010). *Numerical simulations of the flow produced by a comet impact on the Moon and its effects on ice deposition in cold traps*. University of Texas, Austin.

Stewart, B. D., Pierazzo, E., Goldstein, D. B., Varghese, P. L. and Trafton, L. M. (2011). Simulations of a comet impact on the Moon and associated ice deposition in polar cold traps. *Icarus*, 215(1), p. 1-16.

Sunshine, J. M., Farnham, T. L., Feaga, L. M., Groussin, O., Merlin, F., Milliken, R. E. and A'Hearn, M. F. (2009). Temporal and spatial variability of lunar hydration as observed by the Deep Impact spacecraft. *Science*, 326(5952), p. 565-568.

Svetsov, V. V. and V. V. Shuvalov (2015). Water delivery to the Moon by asteroidal and cometary impacts. *Planetary and Space Science*, 117, p. 444-452.

Tenishev, V., Combi, M. and Davidsson, B. (2008). A global kinetic model for cometary comae: The evolution of the coma of the Rosetta target comet Churyumov-Gerasimenko throughout the mission. *The Astrophysical Journal*, 685(1), p. 659.

Tsang, W. and Hampson, R. F. (1986). Chemical kinetic data base for combustion chemistry. Part I. Methane and related compounds. *Journal of Physical and Chemical Reference Data*, 15(3), p. 1087-1279.

Vasavada, A. R., Paige, D. A. and Wood, S. E. (1999). Near-surface temperatures on Mercury and the Moon and the stability of polar ice deposits. *Icarus*, 141(2), p. 179-193.

Verdes, C. L., von Engeln, A., Buehler, S. A. and Perrin, A. (2005). Partition function data and impact on retrieval quality for an mm/sub-mm limb sounder. *Journal of Quantitative Spectroscopy and Radiative Transfer*, 90(2), p. 217-238.

Wagner, W. (1992). A convergence proof for Bird's direct simulation Monte Carlo method for the Boltzmann equation. *Journal of Statistical Physics*, 66(3), p. 1011-1044.

Walker, A. C., Gratiy, S. L., Goldstein, D. B., Moore, C. H., Varghese, P. L., Trafton, L. M., Levin, D. A. and Stewart, B. (2010). A comprehensive numerical simulation of Io's sublimation-driven atmosphere. *Icarus*, 207(1), p. 409-432.

Wang, A. and Modest, M. F. (2006). Photon Monte Carlo simulation for radiative transfer in gaseous media represented by discrete particle fields. *Journal of Heat Transfer*, 128(10), p. 1041-1049.

Watanabe, K. and Zelikoff, M. (1953). Absorption coefficients of water vapor in the vacuum ultraviolet. *JOSA*, 43(9), p. 753-755.

Watson, K., Murray, B. C. and Brown, H. (1961). The behavior of volatiles on the lunar surface. *Journal of Geophysical Research*, 66(9), p. 3033-3045.

Weissman, P. R. (2006). The cometary impactor flux at the Earth. *Proceedings of the International Astronomical Union*, 2(S236), p. 441-450.

Williams, J., Paige, D. A., Hayne, P. O., Vasavada, A. R. and Bandfield, J. L. (2013). Modeling Anisothermality in LRO Diviner Observations to Assess Surface Roughness and Rock Abundance. *AGU Fall Meeting Abstracts*.

Yeoh, S. K., Chapman, T. A., Goldstein, D. B., Varghese, P. L. and Trafton, L. M. (2015). On understanding the physics of the Enceladus south polar plume via numerical simulation. *Icarus*, 253, p. 205-222.

Zhang, J., Goldstein, D. B., Varghese, P. L., Gimelshein, N. E., Gimelshein, S. F. and Levin, D. A. (2003). Simulation of gas dynamics and radiation in volcanic plumes on Io. *Icarus*, 163(1), p. 182-197.

Zhang, J. (2004). *Simulation of Gas Dynamics, Radiation and Particulates in Volcanic Plumes on Io.* University of Texas, Austin.

Zuber, M. T., Head, J. W., Smith, D. E., Neumann, G. A., Mazarico, E., Torrence, M. H., Aharonson, O., Tye, A. R., Fassett, C. I., Rosenburg, M. A. and Melosh, H .J. (2012). Constraints on the volatile distribution within Shackleton crater at the lunar South Pole. *Nature*, 486(7403), p. 378-381.